PEOPLE'S DEMOCRATIC REPUBLIC OF ALGERIA
Ministry of Higher Education and Scientific Research
University of Amar Telidji - Laghouat

Faculty of Technology
Department of Electrical Engineering

LMD DOCTORAL THESIS

Presented with a view of obtaining the doctoral diploma LMD

Contribution à la simulation et la modélisation du contrôle d'un système de pile à combustible à membrane échangeuse de protons

Contribution to the simulation and control modeling of a proton exchange membrane fuel cell system

Presented by
Mohammed Yousri Silaa

Prof.	Salem Arif	*President*	University of Amar Telidji, Laghouat, Algeria
Prof.	Ali Cheknane	*Supervisor*	University of Amar Telidji, Laghouat, Algeria
Dr.	Khalil Benmouiza	*Co-supervisor*	University of Amar Telidji, Laghouat, Algeria
Prof.	Amine Boudghene Stamboli	*Examiner*	Oran Mohamed-Boudiaf University of Science and Technology
Prof.	Khaled Touafek	*Examiner*	Applied Research Unit in Renewable Energies of Ghardaia
Dr.	Bachir Mokhtari	*Examiner*	University of Amar Telidji, Laghouat, Algeria

2020-2021

الملخص

في هذه الأطروحة، تم اقتراح منهجيات تحكم متنوعة للتحكم في المحول رافع الجهد DC/DC من أجل تحسين جودة طاقة خرج خلايا الوقود ذات الغشاء التبادل البروتوني (PEMFC). الهدف الرئيسي هو الحفاظ على نظام طاقة خلايا الهيدروجين يعمل عند نقطة طاقة مناسبة في منطقة التشغيل. تم إنشاء هاته المنطقة من قبل الباحثين حيث يمكن استخراج ما يصل إلى أكثر 90٪ من الحد الأقصى للطاقة المولدة، بسبب عدم خطية خلايا الهيدروجين وتأثيرها على المعاملات مثل درجة حرارة الخلية، والضغط الجزئي للأكسجين، والضغط الجزئي للهيدروجين ومحتوى الماء. تم اقتراح منهجيات تحكم غير خطية. أولا، لم ينجح تطبيق وحدات التحكم الخطية التقليدية مثل المتحكم التناسبي (P) والتناسبي المتكامل (PI) والمشتق التناسبي المتكامل (PID) في دفع النظام للعمل بدقة في نقطة طاقة مناسبة. لذلك تقترح هذه الأطروحة تحكما قويا لا خطي يتمثل في التحكم بالنمط الانزلاقي النهائي السريع المتكامل (IFTSMC) بهدف تحسين جودة الطاقة الناتجة PEMFC، إلى جانب ذلك، تم تصميم وتنفيذ مرشح رقمي لتنعيم الإشارات من تأثير التذبذب السريع الناتجة عن المتحكم IFTSMC . يتم إثبات استقرار النظام عبر نظرية ليابونوف. تشير النتائج التجريبية المقارنة مع وحدة التحكم PI إلى أنه يمكن تحقيق تخفيض قدره 96% في وقت الاستجابة باستخدام الخوارزمية المقترحة حيث تم ازالة أكثر من 91 % من ظاهرة التذبذب السريع عن طريق تطبيق المرشح الرقمي.

ثانيا: يتم استخدام المتحكم في النمط الإنزلاقي من الدرجة الأولى (SMC) ومع ذلك، فإن ظاهرة التذبذب السريع الناتجة عن SMC تؤدي إلى انخفاض دقة التحكم وفقدان الحرارة في دوائر الطاقة. من أجل التغلب على هذه العيوب، تم اقتراح جهاز التحكم في النمط الإنزلاقي شبه المستمر عالي الترتيب (QC-HOSM) من أجل تحسين جودة الطاقة والأداء. تم إثبات استقرار جهاز التحكم من خلال نظرية ليابونوف. من أجل إثبات فعالية مخطط التحكم المقترح، تمت مقارنة النتائج التجريبية مع المتحكم SMC التقليدي. تظهر النتائج التجريبية التي تم الحصول عليها أنه تم تحقيق خفض في التذبذب السريع قدر 84 % باستخدام-QC HOSM. تم تصميم منهجيات وحدات التحكم المقترحة لنظام الحلقة المغلقة التجريبي الذي يتكون من PEM FC50 ، التحكم في النمط الإنزلاقي من الدرجة الاولى، التحكم بالنمط الانزلاقي النهائي السريع المتكامل، DSPACE DS1202 وDSPACE DS1104 , محول رافع للجهد متصل بخلية هيدروجين و مقاومة قابلة للبرمجة.

ثالثا: تم اقتراح تقنية الضبط والتحسين بناءا على خوارزمية تحسين سرب الجسيمات (PSO) من أجل ضبط معاملات وحدة التحكم PID في حالة جيدة. حيث يتم تطبيق هذا الأخير على محول رافع للجهد من اجل تحسين خرج جودة طاقة نظام خلية الوقود ذات الغشاء التبادل البروتوني. وبالتالي نظرا لمزاياها مقارنة بوحدة التحكم التقليدية Ziegler-Nichols PID. تم تنفيذ النموذج ووحدات التحكم في بيئة MATLAB

SIMULINK/ . تمت دراسة فعالية الخوارزمية المقترحة بنجاح باستخدام محول رافع للجهد متصل بـخلية وقود ذات التبادل البروتوني. تم عرض الدراسة والمقارنة مع Ziegler -Nichols حيث تم إثبات فعالية الخوارزمية المقترحة في الاستجابات العابرة، والحالة الثابتة، والديناميكية، وانخفاض التجاوز ووقت الاستجابة خاصة ضد تباين الحمل الشديد. أخيرا، تظهر مراجعة النتائج أن الخوارزمية المقترحة لها مزايا كبيرة مقارنة بوحدات التحكم التقليدية.

الكلمات الدالة:

خلية الهيدروجين ذات الغشاء التبادل البروتوني، التحكم في النمط الإنزلاقي من الدرجة الأولى، التحكم بالنمط الإنزلاقي النهائي السريع المتكامل، مرشح رقمي، التحكم في النمط الإنزلاقي الشبه المستمر، محول رافع للجهد، DSPACE DS1104 وDSPACE DS1202 ,خوارزمية تحسين سرب الجسيمات وتقنية Ziegler-Nichols.

Abstract

In this thesis, diverse control methodologies are proposed for the control of the boost converter in order to improve the proton exchange membrane fuel cell (PEMFC) output power quality. The main aim is to keep the PEMFC power system operating at an adequate power point of the operating zone. This zone was created by the researchers at which up to more than 90% of the maximum generated power could be extracted, due to the non-linearity of the proton exchange membrane fuel cells (PEMFCs) and their affectation by the parameters such as cell temperature, the partial pressure of oxygen, the partial pressure of hydrogen and water content of the membrane. A non-linear controllers methodologies, have been proposed.

First, the application of conventional linear controllers such as proportional (P), proportional-integral (PI) and proportional-integral-derivative (PID) did not succeed to drive the system to operate precisely in an adequate power point. Therefore, this thesis proposes a robust non-linear integral fast terminal sliding mode control (IFTSMC) aiming to improve the power quality generated by the PEMFC; besides, a digital filter is designed and implemented to smooth the signals from the chattering effect of the proposed controller. The stability proof of the IFTSMC is demonstrated via Lyapunov analysis. Comparative experimental results with the PI controller indicate that a reduction of 96% in the response time could be achieved using the suggested algorithm; where, up to more than 91% of the chattering phenomenon could be eliminated via the application of the digital filter.

Second, a conventional first-order sliding mode control (SMC) is used. However, the chattering phenomenon, which is caused by the SMC leads to low control accuracy and heat loss in the energy circuits. In order to overcome these drawbacks, the quasi-continuous high-order sliding-mode controller (QC-HOSM) is proposed so as to improve power quality and the performance. The QC-HOSM controller stability is proven via the Lyapunov theory. In order to demonstrate the effectiveness of the proposed control scheme, ex-

perimental results are compared with the conventional SMC. The obtained experimental results show that a chattering reduction of 84% is achieved using the QC-HOSM.
The proposed controllers methodologies are designed for an experimental closed-loop system which consisted of a Heliocentric hy-Expert™ FC-50W, MicroLabBox DSPACE DS1202, DSPACE DS1104, step-up DC-DC power converter and programmable load .
Third, a tuning and optimization technique has been proposed based on particle swarm optimization algorithm (PSO) in order to set the PID controller parameters in a good condition. Where, this latter is applied to a DC/DC boost converter in order to improve and optimize the PEMFC system power quality. Thus, due to its advantages compared with the conventional Ziegler-Nichols (ZN) tuning PID controller. The model and controllers have been implemented in MATLAB/SIMULINK environment. The proposed algorithm effectiveness has been studied successfully using a DC/DC step-up converter connected to a PEMFC. Study and comparison with the ZN are presented. The effectiveness of the proposed algorithm in transient, steady-state, dynamic responses, low overshoot and response time, especially against extremely load variation, have been demonstrated. Finally, a review of results shows that the suggested algorithm has significant advantages over conventional controllers.

Keywords:

proton exchange membrane, sliding mode control, integral fast terminal sliding mode control, digital filter, quasi-continuous high-order sliding-mode control, DC/DC step-up converter, particle swarm optimization algorithm, Ziegler-Nichols method.

Résumé

Dans cette thèse, diverses méthodologies de contrôle sont proposées pour le contrôle du convertisseur élévateur afin d'améliorer la qualité de la puissance de sortie des piles à combustible à membranes échangeuses de protons (PEMFC). L'objectif principal est de maintenir le système d'alimentation PEMFC en fonctionnement à un point d'alimentation adéquat de la zone de fonctionnement. Cette zone a été créée par les chercheurs, permettant d'extraire jusqu'à plus de 90% de la puissance maximale générée, en raison de la non-linéarité des PEMFCs et de leur affectation des paramètres tels que la température de la cellule, la pression partielle de l'oxygène, la pression partielle d'hydrogène et la teneur en eau de la membrane. Des méthodologies de contrôleurs non linéaires ont été utilisées.
Premièrement, l'application de contrôleurs linéaires conventionnels tels que proportionnel (P), proportionnel-intégral (PI) et proportionnel-intégral-dérivé (PID) n'a pas réussi à amener le système à fonctionner avec précision dans un point de puissance adéquat. Par conséquent, cette thèse propose une commande par mode de glissement terminal rapide intégrale non linéaire robuste (IFTSMC) visant à améliorer la qualité de l'énergie générée par le PEMFC; en outre, un filtre numérique est conçu et mis en œuvre pour lisser les signaux de l'effet de broutage de l'IFTSMC. La preuve de stabilité de l'IFTSMC est démontrée via le critére de Lyapunov. Des résultats expérimentaux comparatifs avec le contrôleur PI indiquent qu'une réduction de 96% du temps de réponse pourrait être obtenue en utilisant l'algorithme suggéré; où, jusqu'à plus de 91% du phénomène de broutage pourrait être éliminé via l'application du filtre numérique.
Deuxièmement, une commande par mode glissant (SMC) conventionnelle du premier ordre est utilisée. Cependant, le phénomène de broutage, qui est provoqué par le SMC, conduit à une faible précision de contrôle et à une perte de chaleur dans les circuits d'énergie. Afin de remédier à ces inconvénients, le contrôleur de mode glissant d'ordre élevé quasi-continu

(QC-HOSM) est proposé afin d'améliorer la qualité de la puissance et les performances. La stabilité du contrôleur QC-HOSM est prouvée via le critére de Lyapunov. Afin de démontrer l'efficacité du schéma de contrôle proposé, les résultats expérimentaux sont comparés avec le SMC conventionnel. Les résultats expérimentaux obtenus montrent qu'une réduction de broutage de 84% est obtenue en utilisant le QC-HOSM. Les méthodologies de contrôleurs proposées sont conçues pour un système expérimental en boucle fermée qui se composait d'un hy-Expert ™ FC-50W héliocentrique, d'une MicroLabBox DSPACE DS1202, DSPACE DS1104, d'un convertisseur de puissance DC-DC élévateur et une charge programmable.
Troisièmement, une technique de réglage et d'optimisation a été proposée basée sur l'algorithme d'optimisation de l'essaim de particules (PSO) afin de régler les paramètres du contrôleur PID dans un bon état. Où, ce dernier est appliqué à un convertisseur élévateur DC/DC afin d'améliorer et d'optimiser la qualité de puissance du système de pile à combustible à membrane échangeuse de protons (PEMFC). Ainsi, en raison de ses avantages par rapport au régulateur PID de réglage Ziegler-Nichols conventionnel. Le modèle et les contrôleurs ont été implémentés dans l'environnement MATLAB / SIMULINK. L'efficacité de l'algorithme proposé a été étudiée avec succès en utilisant un convertisseur élévateur DC/DC connecté à un PEMFC. Une étude et une comparaison avec les Ziegler-Nichols sont présentées. L'efficacité de l'algorithme proposé dans les réponses dynamiques transitoires, en régime permanent, les faibles dépassements et temps de réponse, en particulier contre des variations de charge extrêmes, a été démontrée. Enfin, un examen des résultats montre que l'algorithme suggéré présente des avantages significatifs par rapport aux contrôleurs conventionnels.

Mots-clés:

piles à combustible à membrane d'échange de protons, mode glissant du premier ordre, mode glissement terminal rapide intégrale , filtre numérique, mode glissant d'ordre élevé quasi-continu, convertisseur élévateur DC/DC, algorithme d'optimisation par essaims particulaires, méthode de Ziegler-Nichols.

Dedication

I would like to present this writing to my family
For giving me all the inspiration and support I need,
Thank you...

Acknowledgements

This work was supported by the laboratory of semiconductors and functional materials, Amar Telidji university of **Laghouat, BP 37G, 03000, Algeria.**

The experimental study presented in this thesis was carried out at the level of the laboratory of advanced control, university of **Vitoria-Gasteiz, Spain.**

First of all, I'd like to thank **"ALLAH"** almighty, the most merciful and compassionate, for his support, help and generosity.

I would like to thank my supervisor **Prof. Ali Cheknane**, Professor in Renewable energy, and Dean of the Faculty of Technology, **Laghouat University**, for his supervision, continuous caring and guidance discussion. I am very indebted to him for his continuous encouragement, unforgettable help and kind feeling throughout the course of this study. And also, I would like to thank my co-supervisor **Dr. Khalil Benmouiza**, **Laghouat University**, for his helpful cooperation and continuous encouragement.

I would also like to thank my committee members, **Prof. Salem Arif**, **Prof. Amine Boudghene Stambouli**, **Prof. Khaled Touafek** and **Dr. Bachir Mokhtari** for letting my defence be an enjoyable moment, and for their brilliant comments and suggestions, thanks to you all.

I would like to express my deepest gratitude to **Prof. Oscar Barambones**, **Universidad del país vasco upv/ehu**, for giving me the opportunity to accomplish this modest work, for his excellent guidance, caring, patience, sharing expertise and encouragement extended to me, in addition to making sure that this research work takes place in the best conditions.

Also, I would like to thank my friends **Dr. Derbeli Mohamed** and **Dr. Cristian Napole**, **Universidad del país vasco upv/ehu**, for their helpful cooperation and continuous encouragement.

Publications

1. Silaa, M. Y., Derbeli, M., Barambones, O., Napole, C., Cheknane, A., Gonzalez De Durana, J. M. (2021). An efficient and robust current control for polymer electrolyte membrane fuel cell power system. Sustainability, 13(4), 2360.

2. Silaa, M. Y., Derbeli, M., Barambones, O., Cheknane, A. (2020). Design and implementation of high order sliding mode control for PEMFC power system. Energies, 13(17), 4317.

3. Silaa, M. Y., Cheknane, A, Barambones, O., Derbeli, M., Napole, C., (2021). Implementation of PID controller tuning using particle swarm optimization algorithm for PEM fuel cell power system. National Conference on Renewable Energies and Energy Efficiency.

Contents

List of Figures

List of Tables

List of Symbols

- R^n: denotes the n-dimensional Euclidean space. We will drop the superscript for real numbers and write just R.
- R: is the set of real numbers.
- V_{FC}: denotes the PEM fuel cell voltage.
- E_{Ner}: denotes the nernst voltage.
- V_{act}: denotes the activation overvoltage.
- V_{ohm}: denotes the ohmic overvoltage.
- V_{conc}: denotes the overvoltage concentration.
- $\zeta_{1,2,3,4}$: denotes the parametric coefficients of the cell.
- ψ: denotes the constant parameter of the cell.
- J, J_{max} : denotes the current density and the maximum current density.
- N_{cell} : denotes the number of cells.
- $\triangle g_f$: denotes the Gibbs free energy.
- L, C: inductance, capacitor.
- T_d : denotes the period.
- I_s : denotes the diode saturation current.
- I_{max} : denotes the maximum current in the inductor.

- I_{min} : denotes the minimum current in the inductor.
- $\triangle i_L$: denotes the current ripple in the inductor.
- $\triangle V_s$: denotes the output voltage ripple.
- α: denotes the duty cycle.
- f_s: denotes the switching frequency.
- $\vec{x}_{ij}$: denotes the swarm position vector.
- $\vec{v}_{ij}$: denotes the swarm velocity vector.
- $\vec{w}$: denotes coefficient of inertia .
- $e(t)$: error signal.
- f: the criterion to be optimized.
- $V(x)$: the Lyapunov function.
- $s(x)$: sliding variable.
- s: the sliding surface.
- u: the command control.
- u_{eq}: the equivalent command control.
- u_{sw}: the total command control.

List of Abbreviations

PEMFC	proton exchange membrane fuel cell
P	proportional
PI	proportional-integral
PID	proportional-integral-derivative
IFTSMC	integral fast terminal sliding mode control
SMC	conventional first-order sliding mode control
HO-SMC	high order sliding mode
QC-HOSM	quasi-continuous high-order sliding-mode controller
PSO	particle swarm optimization algorithm
ZN	Ziegler-Nichols
IAE	integral of absolute error
ISE	integral of squared error
ITAE	integral of time weighted absolute value of error
ITSE	integral of time weighted squared error
VSC	variable structure control
TWG	twisting algorithm
STWG	super-twisting algorithm
PCL	prescribed convergence law algorithm

GENERAL INTRODUCTION

Throughout history, earth temperature has been affected by small variations of the orbit, which results in slight changes in the climate [Saltzman, 1984]. However, in the recent few decades, global warming has been characterized by an abrupt increase due to the carbon dioxide emissions caused by human activities [Saltzman, 1984]. As a solution for this matter and in order to reduce its development, coal plants over the world are being replaced by clean and renewable energies such as wind turbines, solar panels, bio-oils, water and hydrogen power sources [Kåberger, 2018].

Hydrogen is the most abundant element in the universe; it represents up to more than 75% of all normal matter mass, and it accounts for over 90% of all atoms number on earth [Magoon, 2018]; it is found in molecular forms such as water or organic compounds (methane, coal, petroleum..). Hydrogen could be produced by either simple methods such as the electrolysis of water or industrial methods using steam reforming. The production cost of hydrogen is expected to fall by 50% by the middle of this century, and that could pave the way for more sustainable sources of energy [Choudhury and Kraft, 2004]. The latter has encouraged thousands of scientists and researchers to look forward in hydrogen cells.

PEMFCs are among the most efficient electrical generators due to several properties like high energy density, performance and high robustness [Reddy and Samuel, 2020], which leads to multiple applications

such as portable power generation, cars, aircraft and space shuttles [Delgado et al., 2020, Mardle et al., 2020, García-Olivares et al., 2020, Lee and Lin, 2020, Rastayesh et al., 2020].

In such application, DC-DC high step-up power converters are usually desired not only for boosting the PEMFC low voltage, but also to provide regulated output voltage for end use. The DC-DC power converter could be an inductive switching converter or a switched capacitor converter [Kester et al.,], is an adaptation stage circuit that is inserted between the load and the PEMFC stack. One of the most common adaptation stage circuits is the DC-DC boost converter, which is classified as one of the most and simplest used converters. This latter has the ability to step up a lower input voltage into a higher output voltage via controlled the pulse-width-modulation (PWM) switching technique.

Problem statement and motivations

The output characteristics of the PEMFCs are nonlinear and influenced by parameters such as cell temperature, oxygen partial pressure, hydrogen partial pressure and membrane water content. Where these parameters lead to difficulty to predict the PEMFCs behaviour. In order to solve this problem, we have created an efficient power point to hold and drive the PEMFC working on it.

State of the Art

In order to have an efficient power conversion from the PEMFCs to the DC link (or load), many control techniques and algorithms have been adopted during the recent years. For example, in [Choe et al., 2007], an appropriate power point was obtained using a PID controller for a PEMFC

power system. This PEMFC was designed for the boost converter to control the PWM, so as to drive the fuel cell operating at an adequate power point. Results showed that by selecting the accurate parameters, the proposed approach could provide satisfactory results in terms of high tracking efficiency. Authors of [Qi et al., 2020] applied a fractional-order proportional-integral-derivative (FOPID) controller to a four-switch buck-step-up DC/DC converter in order to stabilize the PEMFC output power. The obtained results have shown that the proposed method achieved better performance in comparison with the integer-order, Two-Zero/Three-Pole (TZTP) controller. Hence, an overall efficiency of 92% more than the one obtained with TZTP, can be remained using the FOPID. An optimized PID using slap swarm algorithm (PID-SSA) was designed to track the maximum operating power point of the PEMFC. Comparative results with incremental resistance algorithm (IRA), grey antlion optimizer (GAO), grey wolf optimizer (GWO), mine-blast algorithm (MBA) and fuzzy logic controller (FLC), have indicated better performance of the proposed PID-SSA in terms of efficiency and reliability. The application FLC on PEMFC power systems was introduced by [Derbeli et al., 2017b]. In comparison with perturb and observe system (PO), satisfactory results such as a reduction of 90% in the signal ripples were obtained using the proposed control scheme. In [Luta and Raji, 2019], a FCL based on PSO was designed to hold the PEMFC running at maximum power point. Comparative results with the conventional FLC have demonstrated the effectiveness of the FLC-PSO to reduce the overshoot from 65.833% to 63.115% while ensuring high tracking efficiency (99.39%). However, despite the reduction of 2%, an overshoot up to more than 63% is still undesirable. To optimize the conventional FLC, Reddy and Sudhakar [Reddy and Sudhakar, 2019] also used an adaptive neuro-fuzzy inference system (ANFIS) based on MPPT applied for an electric vehicle PEMFC. Results have indicated that an increase of 1.95% in the average DC link and a reduction of 17.74% in the average time taken to reach the MPP, can be achieved using the proposed ANFIS algorithm. Authors

of [Derbeli et al., 2019a] used SMC aiming to overcome the drawbacks of the classical linear PI controller; their proposed method showed acceptable results in terms of robustness against sharp load variation, but since the SMC was used, the chattering phenomenon was present during the tests.

Recently, high order sliding mode (HO-SMC) have attracted the attention of many researchers due to their capabilities to overcome the drawbacks of the conventional SMC while offering several superior properties such as speeding up the convergence rate and providing high precision control [Che et al., 2020, Cao et al., 2018, Azar and Serrano, 2020, Wang et al., 2019, Ali et al., 2020, Doan et al., 2020, Zafran et al., 2020, Wang et al., 2020]. However, as a solution for the chattering phenomenon, Derbeli et al. [Derbeli et al., 2020] implemented a robust high order sliding mode based on based on twisting algorithm (HOSM-TA) to keep the PEMFC system works at an adequate and efficient power point. Experiment results have shown that the HOSM-TA control gives satisfactory results in terms of reducing the chattering effect; but even though it was reduced up to more than 82%, the occurred considerable overshoot when facing load variations is still one of the main drawbacks of the proposed HOSM-TA control. In Shotorbani et al. [Shotorbani et al., 2017], compared the performance of the distributed terminal sliding mode controller (DTSMC) with divers control schemes such as PI, SMC, proportional finite-time control (PFTC), proportional asymptotic convergent control (PACC) and proportional-integral finite-time control (PIFTC). Results have confirmed the effectiveness of the proposed DTSMC over the other controllers; in terms of accuracy, smooth tracking and robustness when facing external disturbances. A FTSMC was designed by Gudey and Gupta [Gudey and Gupta, 2016], for a low-voltage PEMFC based micro-grid system. Experimental results have demonstrated the effectiveness of the proposed FTSMC (faster convergence and slighter steady-state error) to overcome the inability of the classical SMC to regulate the micro-grid bus voltage. An ITSMC was designed

by [Armghan et al., 2020] for a hybrid AC/DC micro-grids based on a wind turbine and PEMFC generator source. Improved performance in terms of robustness was obtained using the proposed ITSMC scheme with respect to control Lyapunov function (CLF) and SMC. A combination of cascaded adaptive ITSMC with time delay estimation (TDE) algorithm has been implemented by Abbaker et al. [Abbaker AM et al., 2020] for PEMFC air supply system, whereas the proposed adaptive ITSMC-TDE is compared with adaptive ITSMC, cascaded-ITSMC and cascaded integral SMC combined with TDE. Fast convergence rate with less fluctuations in the tracking trajectory, are obtained using the proposed adaptive ITSMC-TDE algorithm.

Objectives of this thesis

The goal of the research is to develop methodologies that ensure solving the PEMFC control problems, which achieves the following objectives:

1. Design of a non-linear control with computational efficiency, stability and convergence even with the existence of disturbances.

2. Force and keep the PEMFC work at an efficient power point.

3. Reduction of the chattering effect as well as to extend the life of the PEM fuel cell.

4. Improvement of the PEMFC output power quality in order to store it in the battery.

5. Validation of the proposed controllers capabilities with experimental tests.

Contribution

This thesis's motivation is to construct controls methodologies based on IFTSMC, QC-HOSM and PID in order to improve the PEMFC output power quality. The main contributions of proposed control schemes are summarised as

1. Successfully applied a robust no-linear IFTSMC combined with a digital filter which improves the PEMFC output power quality.
2. Design and implementation of a robust no-linear QC-HOSM as well as to reduce the conventional SMC chattering effects.
3. The stability proof of the proposed control methodologies is demonstrated via Lyapunov analysis, which guarantee system convergence.
4. Implementation of an optimization technique based on PSO in order to set the PID controller parameters in good condition.
5. The proposed controllers scheme are designed for an experimental closed-loop system which consisted of a Heliocentric hy-Expert^{TM} FC-50W, MicroLabBox dSPACE DS1104 and DSPACE DS1202, step-up DC-DC power converter and programmable DC power supplies.

Thesis organization

The remainder of the thesis is organised as follows:

In chapter two, we will discuss the fuel-cell type proton exchange membrane, as well as the mathematical equations related to its work that show the performance of the cell. Finally, modeling the hydrogen cell by MATLAB/SIMULINK environment.

Chapter three is devoted to the electronics interfaces for optimization of

the PEMFC power system. Where, those interfaces are deal with the problem of energy optimization of a PEMFC system. It begins with the direct connection of a PEMFC with the load. This configuration does not guarantee optimal energy transfer. To overcome this drawback, an adaptation stage is necessary. Subsequently, an operational analysis of several non-isolated DC/DC converters (buck, boost, buck-boost, sepic and cuk) acting as adapters is done.

In the fourth chapter, we will expose the different structures of the PID regulator, the different performance criteria, as well as the classic method of tuning control loops based on ZN and the PSO method.

Definition of variable structure systems, generalities on nonlinear control based on conventional sliding mode, High order sliding mode (second order and arbitrary order) analysis of the operating principle are described in chapter five.

Chapter six focuses on the application of the proposed control strategies on a PEMFC power system based on a DC/DC converter type boost. The system will be implemented in Matlab / Simulink and loaded practically on a DSPACE card.

In the general conclusion, we present a summary of the work carried out as well as the main results obtained, then the perspectives of this work.

Chapter 1

AN OVERVIEW OF PEMFC TECHNOLOGY

> I believe that water will one day be employed as fuel, that hydrogen and oxygen which constitute it, used singly or together, will furnish an inexhaustible source of heat and light, of an intensity of which coal is not capable.
>
> *Jules Verne*

1.1 Introduction

Fuel cells provide clean and efficient energy production and are currently being developed around the world. They are the means par excellence of using the hydrogen energy vector to produce electricity. In fact, they are electrochemical devices that directly convert chemical energy from a fuel into electrical energy to generate water and heat. There are six types of fuel cells [Larminie et al., 2003], three of which operate with a liquid electrolyte

and three with a solid electrolyte. Note that these fuel cells are classified according to the nature of their electrolyte and their operating temperature. The current market trend is towards small production units. This is why our study focuses on the PEMFC generator. Furthermore, generating electricity from hydrogen does not require large power stations. In fact, a single cylinder of hydrogen, when attached to several hydrogen cells, could do the trick and provide the electricity needed for the daily needs.

In this chapter, we will describe the energy and environmental issue. An introduction of the basic concepts of a PEMFC, its operating principle, the characteristic curve, as well as its operating variables. Mathematical modelling will be described in order to plot the current-voltage (I-V) and power-voltage (P-V) characteristics of the PEM fuel cell by showing the influence of meteorological conditions (gases pressures and temperatures).

1.2 Energy and hydrogen issue

Hydrogen is the first element of the periodic table consisting of a proton. It is the simplest and most abundant element in the universe. Where it is always found in combination with other elements, water, for example, is a combination of hydrogen and oxygen. Hydrogen is also found in many organic compounds notably, the hydrocarbons that make up fuels such as gasoline natural, gas, methanol and propane. Hydrogen is primarily produced using two methods, system reforming and electrolysis, also known as water splitting. Today the major of all hydrogen is produced from steam reforming of natural gas electrolysis, which is a process that splits water into its basic elements using electric current. The electricity used in the process may come from hydrocarbons or renewable. Hydrogen is an efficient way to store and transport energy, which leads to many important applications. Hydrogen can also used for the electricity production that on a fuel cell.

1.2.1 Energy issue

With the development of the industry for several decades, we are consuming more and more energy resources to be able to meet the growing energy needs of the population. Almost 80% of the world's energy production comes from coal, oil, natural gas and the rest from nuclear, etc. [Hoogers, 2002]. The depletion of these resources is becoming a problem of concern to all of us; energy issues currently cover two areas. One is linked to the risk of depletion of fossil and fissile resources, in particular that of oil which at the current rate of consumption, is expected in a century or less. The other is the problem of environmental pollution, in particular, the emission of CO_2 (greenhouse gases) and polluting gases (SO_2, NOx, CO, CH_4, $photofluorography$, $solidparticles$, *etc.*), from vehicles of transport or industrial enterprise Figure 1.1.

Figure 1.1: Environmental pollution.

Since the $19th$ century, more and more CO_2 has been released Figure 1.2, now it is important to stop this progression and reduce its risks as much as possible.

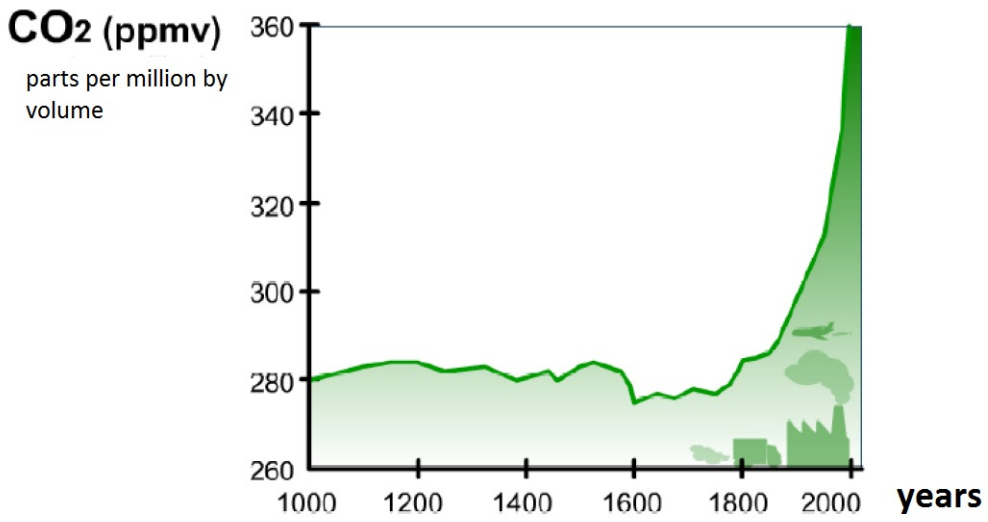

Figure 1.2: Increasing carbon dioxide since the 19*th* century [Zhang, 2010]

1.2.2 Hydrogen technology

Faced with the incessant increase in energy consumption and the environmental problems it raises, it is urgent to make societal choices. Two solutions are proposed. The first one is to reduce overall energy consumption. Several governments, aware of this situation, reached an agreement in Japan in 1997 and signed the Kyoto protocol, which aims to reduce and stabilize CO_2 emissions for the period $2008 - 2012$. Unfortunately, these agreements have a limit. The second solution is to develop new technologies that are more favourable to the environment. Hydrogen energy appears to be one of the most promising solutions because it presents several interesting characteristics [Hoogers, 2002]:

- Efficient energy: compared to petroleum or coal, hydrogen of equivalent weight releases about three times more energy than oil, about six times more energy than coal.
- Clean Energy: production of water without pollution.

– Reliable source: hydrogen is very abundant and very accessible.

Thanks to the many advantages, hydrogen is very environmentally and friendly energy. Research into new user technologies has been encouraged and undertaken to develop systems for converting or producing electrical energy. PEMFCs appear to be one of the best solutions for converting hydrogen into electrical energy.

1.3 General description of a fuel cell

A fuel cell is a generator of electrical energy. It directly converts the chemical energy of the fuel into electrical energy. It is a system that produces virtually no noise pollution since it does not have any moving mechanical components, such as turbines and motors. Besides, an electric current is produced as long as the cell is jointly supplied with fuel (hydrocarbons, alcohols, biomass, natural gas, hydrogen) and oxidizer (oxygen in the air). That is what differentiates it from batteries, accumulators and other cells, where a limited amount of electrical energy is stored in chemical form and must either be recharged when possible (vehicle battery) or replaced (radio batteries).

1.3.1 Brief history of a fuel cell

In 1806, Mr Humphry Davy carried out the electrolysis of distilled water and obtained hydrogen and oxygen by consuming electricity. Christian Friedrich Schoenbein was the first to observe the principle of fuel cells in 1838. In his experiment, he uses a U-tube with two platinum electrodes. It uses an electric current to obtain hydrogen and oxygen. When he cuts off the power, he finds that the gases produce an electric current in the opposite direction to the first. William Robert Grove met Schoenbein at a conference in Birmingham in 1839. The two men's sympathized and learned of their research. In 1839 Grove demonstrated the principle of the fuel cell [Grooves, 1839].

In his famous experiment, he used U-tubes Figure 1.3, it was a hydrogen-oxygen with porous platinum electrodes and sulfuric acid as the electrolyte.

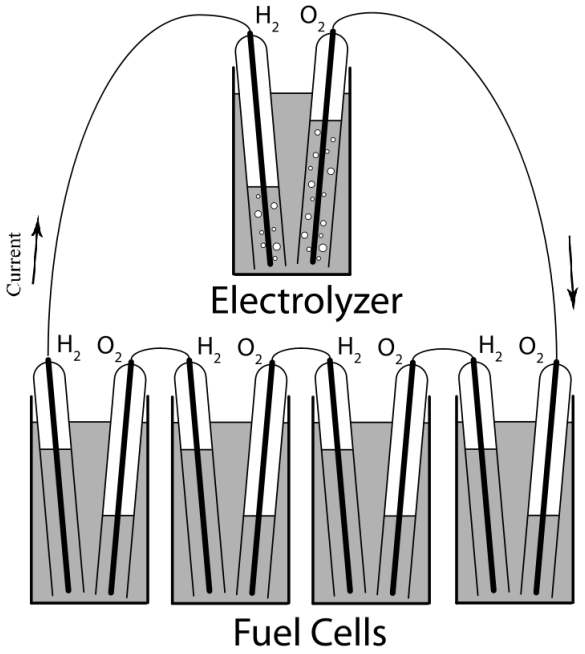

Figure 1.3: Fuel cell invented by Grove [Mosdale, 2003].

A constant current flows between the platinum electrodes, one end of which is submerged in a container of sulfuric acid and the other in sealed containers to collect oxygen and hydrogen. The sealed containers held water like gas, and he noted that the water level had risen in both tubes as long as the current was circulating. By combining several sets of these electrodes in a series circuit, he created what he called a "gas stack", a name given in 1889 by Ludwig Mond and Carl Langer [Mosdale, 2003] who introduced the catalysts (platinum) and have perfected the electrolyte.

At the end of the $19th$ century, Friedrich Wilhelm Ostwald, the physical chemist who provided much of the theoretical understanding of how batteries work, by studying the relationship between physical property and chemical reactions, improved Grove's battery. In 1893, he experimentally determined

the interactive roles between different components of the battery: electrodes, electrolytes, oxidants and ions, etc. His work in chemistry gave the foundations of the fuel cell to researchers. He later also demonstrated that the batteries were more efficient than the internal combustion engine [Srinivasan, 2006].

In the 1930s, another famous scientist, Francis Thomas Bacon Figure 1.4 set out to develop an operational device based on Grove's experience. He improved the expensive platinum catalyst of a hydrogen-oxygen heat pump using an electrolyte less corrosive alkaline and a less expensive nickel electrode called an Alkaline Fuel Cell (AFC). In 1959, Bacon and his colleagues produced a hydrogen-oxygen fuel cell with a power of 5 kW capable of powering a machine. The operating temperature ranged from 40° C to 200° C. Later, Bacon's stack was modified for the Gemini Space Project of 1960 to obtain electricity and water for space travel [Stevens et al., 2000].

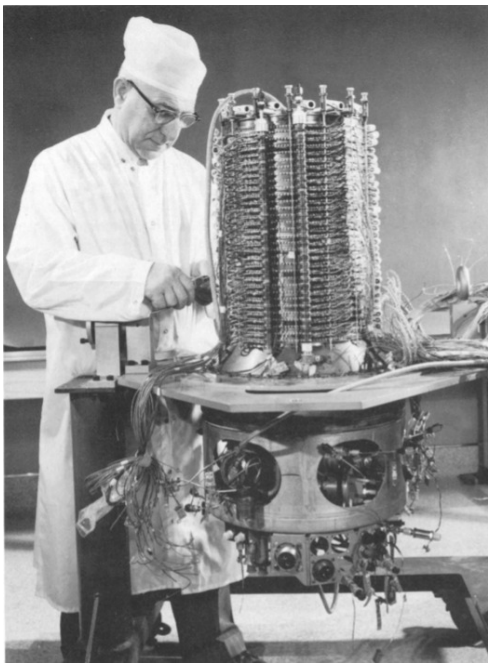

Figure 1.4: Francis Thomas Bacon and the fuel cell [Williams, 1994]

For the fuel cell to be as efficient as the Bacon cell, the electrolyte must be such that the ions pass through it as easily as a flow of electrons. It is later discovered that several cells stacked together provide high power.

The modern fuel cell with a membrane has allowed application in a stationary or mobile environment.

The PEMFC is also called a solid polymer fuel cell because of the use of solid electrolyte. The first fuel cell type PEM shown in Figure 1.5, was designed by the company General Electric at the beginning of the 1960 thanks to the work of Thomas Grubb and Leonard Niedrach [Grubb and Niedrach, 1960].

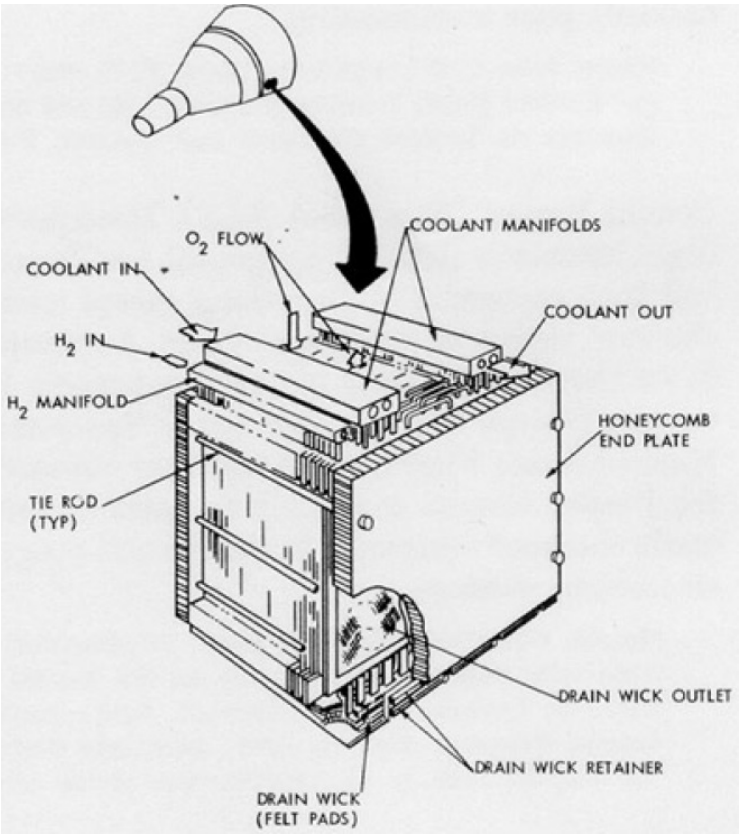

Figure 1.5: PEMFC used in the Gemini program [Behling, 2012]

PEMFCs technology was used in the Gemini Project at the start of 1960. In 1970, the Dupont company developed the Nafion membrane for another use, which made it possible to relaunch fuel cells from PEM. A large number of products derived from Modifications of Nafion and other polymers (e.g. sulfonated polyether ketones or SPEKs) are appearing in a wide variety of battery prototypes. The development of fuel cells largely followed the history of membranes.

The very strong development of PEMFC research in the 1970s resulted from the first oil crisis. In 1972, more than 30 research projects were carried out in the United States on the storage of on-board hydrogen or on its manufacture embedded.

In the 1980s, battery technology began to be tested by utilities and automakers. Technical advances were made with the development of the first vehicle equipped with a PEMFC in 1993 by the company Canadian Ballard. [Hua et al., 2014].

Since then, the focus of fuel cell research has been on the practical application level: improving performance and service life.

1.3.2 Fuel cell types

The classification of fuel cells is generally done according to the nature of the electrolyte because it determines, on the one hand, the temperature at which the cell operates and, on the other hand, the type of ion ensuring ionic conduction. The classification is mainly based on:

- The nature of the membrane: liquid or solid
- Fuel cell operating temperature: low (60° C-250° C) or high (600° C-1000° C)

Table 1.1: Types of fuel cells

Fuel cell	**Electrolyte**	**Temperature** $°C$	**Combustible**	**Oxidizer**	**Field of use/Power range**
AFC	Alcaline KOH, N_aOH	$60-120$	Pure H_2	Air or pure O_2	Space transport and vehicle $1-100kW$
PEMFC	Proton Exchange Membrane (Nafion)	$60-120$	Pure H_2	Air or pure O_2	Portable, transport $10-250kW$
DMFC	Proton Exchange Membrane (H_2SO_4)	$60-120$	CH_3OH	Air or pure O_2	Portable, transport $5kW$
PAFC	Phosphoric acid H_3PO_4	$150-220$	H_2, CH_4, CH_3OH	Air	Stationary $250W-11MW$
MCFC	Mixture of K_2CO_3 and Li_2CO_3	$600-800$	H_2, CH_4	Air	Stationary $1kW-25MW$
SOFC	Zirconium oxide ZrO_2 and Y_2O_3	$750-1050$	H_2, CH_4, CH_3OH, CO	Air	Stationary $500W-10MW$

There are six types of fuel cells that differ from each other by their operating temperature and by the electrolyte, which giving the cell its name.
Low temperature fuel cells operate between $60°C$ - $250°C$:

- The alcaline fuel cell or alkaline fuel cell (AFC)
- The proton exchange membrane fuel cell or (polymer electrolyte membrane fuel cell: PMEFC)
- The direct methanol fuel cell (DMFC)
- The phosphoric acid fuel cell (PAFC)

High temperature fuel cells operate between $600°C$ - $1000°C$:

- The solid oxide fuel cell (SOFC)

– Molten carbonate fuel cell (MCFC)

Table. 1.1 shows the main characteristics of these different families of fuel cells as well as their fields of application.

1.4 PEMFC modeling

Among all the existing families, the fuel cell type PEM has given rise to numerous research and development work around the world. Technology evolves quickly, especially as it is driven by the desire of the fuel cell manufacturers to provide economically viable and reliable products as quickly as possible.

We will only be interested in the fuel cell type PEM because this technology does indeed seem to be the closest to commercialization in the field of transport. In comparison with other types of fuel cells, the PEMFC has several attractive characteristics [O'hayre et al., 2016] such as:

– Higher power density;

– High efficiency of transformation of the chemical energy into electrical energy;

– Low temperatures, quick and easy to start;

– A solid polymer that reduces the construction, transportation and reliability concerns;

– More compact and lighter: better power density;

– Modular therefore easy to install.

1.4.1 PEMFC principle of operation

A PEMFC works on the reverse principle of water electrolysis. Chemical reagents allow the production of electrical energy. Generally speaking, the fuel is hydrogen, and it combines with oxygen to form water according to a universally known global chemical reaction Equation (1.1):

$$2H_2 \quad + \quad O_2 \quad \longrightarrow \quad 2H_2O \tag{1.1}$$

The electrochemical reaction uses a solid electrolyte membrane that conducts protons and is theoretically impermeable to reactive gases. The electrolyte is sandwiched between two electrodes (the anode and the cathode). The membrane electrode assembly (MEA), is shown schematically in Figure 1.6.

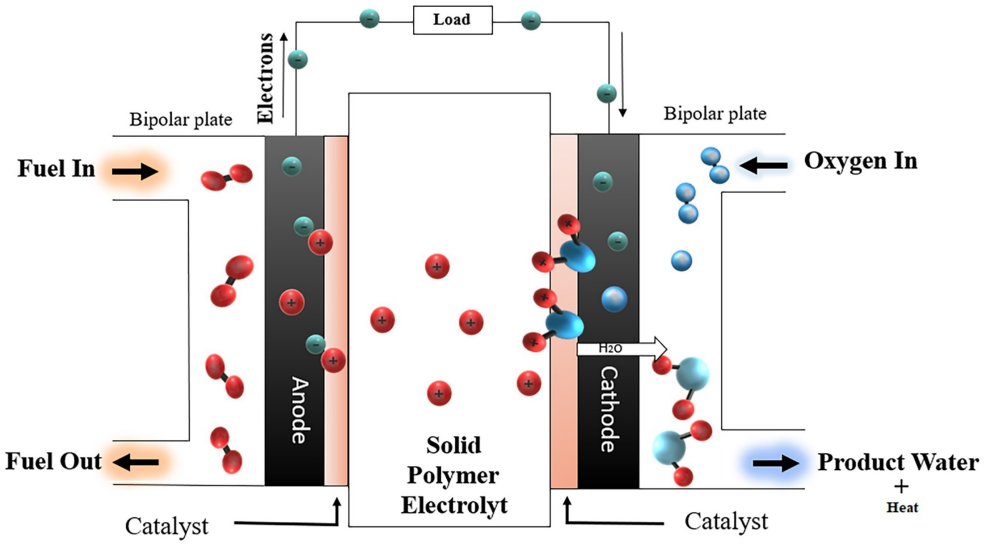

Figure 1.6: Cross section of a single PEMFC.

The electrodes use catalysts to activate the reaction on one side. At the anode, ions and electrons are produced by the oxidation of the fuel (hydrogen), according to equation Equation (1.2). Electrons are always transferred from the anode to the cathode. And then, at the cathode, the electrons allow the reduction of the oxidant (oxygen in the air) and the

production of oxygen ions like equation Equation (1.3). Electrochemical reactions can be represented schematically by:

$$\text{At the anode:} \quad 2H_2 \longrightarrow 4H^+ + 4e^- \tag{1.2}$$

$$\text{At the cathode:} \quad O_2 + 4e^- \longrightarrow 2O^{2-} \tag{1.3}$$

Since the electrolyte is a proton conductor, the material only allows the passage of ions. Ions produced on the anode are always transferred from the anode to the cathode. Finally, at the cathode, the ions combine with the oxygen ions to form water molecules. Electrochemical reactions can be represented schematically by Equation (1.4).

$$\text{At the cathode:} \quad O_2 + 4H^+ + 4e^- \longrightarrow 2H_2O \tag{1.4}$$

This relationship corresponds to that of the combustion of hydrogen and oxygen. The energy of the reaction is released in the form of heat and in the form of electricity. Combustion occurs using a platinum (Pt) catalyst.

The overall chemical reaction of the PEMFC represent in Equation (1.5):

$$4H^+ + O_2 + 4e^- \longrightarrow 2H_2O + electricity + heat \tag{1.5}$$

1.4.2 PEMFC total voltage model

The PEMFC polarization curve is described as a static model; proposed by numerous works [Corrêa et al., 2004, Lee et al., 1998] and [Iqbal, 2003]. In operation, when the fuel cell is producing current, the voltage is always less than the no-load voltage. In fact, voltage losses exist in the fuel cell due to different polarizations. These voltage drops are sometimes called polarizations or over voltages (over potential). They are related to:

– Rate of charge transfers (we speak of activation polarizations),

- Rate of transfer speed (feed) of reagents (we speak of concentration polarizations),
- Resistors (we speak of ohmic polarizations)

A single PEMFC voltage V_{FC} is the sum of four terms: the no-load voltage E_{Ner}, the activation overvoltage V_{act} (or activation drop), the ohmic overvoltage V_{ohm} (or ohmic drop) and the overvoltage concentration V_{conc} (or drop in concentration), which are defined by the following expression [Larminie et al., 2003]:

$$V_{FC} = E_{Ner} + V_{act} + V_{ohm} + V_{conc} \tag{1.6}$$

- Nernst potential

The PMEFC directly converts chemical energy into electrical energy. The chemical energy released can be calculated by the change in Gibbs free energy ($\triangle g_f$), which is the difference between the energy of the products and the energy of the reactants. Gibbs free energy is used to calculate the energy available to do external work. The Gibbs free energy variation for the fuel cell is given by Equation (1.7) [Larminie et al., 2003]:

$$\triangle g_f = (g_f)_{products} - (g_f)_{reactants} = (g_f)_{2H_2O} - (g_f)_{2H_2} - (g_f)_{O_2} \tag{1.7}$$

The variation of Gibbs free energy depends on temperature and pressure as given in Equation (1.8):

$$\triangle g_f = \triangle g_f^0 - RTln\left[\frac{P_{H_2}P^{\frac{1}{2}}O_2}{P_{H_2O}}\right] \tag{1.8}$$

Where $\triangle g_f$ is the variation of Gibbs free energy at standard pressure ($1bar$), which depends on the temperature T expressed in Kelvin. PH_2, PO_2 and

PH_2O are the pressures of hydrogen, oxygen and water vapor, respectively. R is the universal gas constant (8.31451 J.kg^{-1}.K^{-1}). Note that the value of $\triangle g_f^0$ is negative (-237.2 kJ.mol^{-1}) because the energy is released by the reaction. If there were no losses in the fuel cell, all of Gibb's free energy would be converted into electrical energy. For every hydrogen mole, two electrons pass by the external electrical circuit, and the electrical work is equal to the change in Gibbs free energy if the system has no lossless, the electrical work performed is given in Equation (1.9):

$$\triangle g_f = nFE \tag{1.9}$$

Where, F is Faraday's constant ($96,485 Coulombs/mole$), which represents the electric charge of an electron mole. n corresponds to the number of moles of electrons in the reaction. E is the open circuit voltage of the PEMFC. The PEMFC open circuit voltage can therefore be expressed as Equation (1.10):

$$E_{Ner} = \frac{-\triangle g_f}{2F} = \frac{-\triangle g_f^0}{2F} + \frac{RT}{2F} ln \left[\frac{P_{H_2} P^{\frac{1}{2}} O_2}{P_{H_2O}} \right] \tag{1.10}$$

In practice, the operation of PEMFC is accompanied by losses, part of the chemical energy is converted into heat. The term $\frac{-\triangle g_f}{2F}$ varies depending on the operating point. It is equal to 1.229 volts at the standard state ($25°C$) and 1 bar. We can express the tension E in the form [Baschuk and Li, 2005]:

$$E_{Ner} = 1.299 - 0.85.10^{-3}.(T - 298.15) + 4.3085.10^{-5} T \left[ln(PH_2) + \frac{1}{2}.ln(PO_2) \right] \tag{1.11}$$

The voltage depends on the temperature, the pressure of hydrogen and oxygen as represent in the Equation (1.11).

- The activation polarization

The activation losses are occurred due to the kinetics of the reactions taking place at the electrode. They can be calculated using Equation (1.12) [Candusso, 2013].

$$V_{act} = \zeta_1 + \zeta_2 \cdot T + \zeta_3 \cdot T \cdot ln(C_{O2}) + \zeta_4 \cdot T \cdot ln(i) \tag{1.12}$$

Where the parameters ζ_1, ζ_2, ζ_3 and ζ_4 are parametric coefficients determined by the constructor, I is the current of the PEMFC, and C_{O2} is the oxygen concentration in the catalysts ($mol \cdot cm^{-3}$) and it could be calculated using Equation (1.13).

$$C_{O2} = \frac{P_{O2}}{5.08 \cdot 10^6 \cdot e^{(\frac{-498}{T})}} \tag{1.13}$$

- The ohmic losses

The ohmic losses are occurred due to the electrical resistance of the different elements of the PEMFC. They have two origins: the internal resistance of the electrolyte membrane R_{mem} and the resistance that occurred occurred due to the contact between the bipolar plates and the carbon electrodes R_{con}. These losses can be calculated using Equation (1.14) [Ceraolo et al., 2003]:

$$V_{ohm} = I \cdot (R_{mem} + R_{con}) \tag{1.14}$$

Where

$$R_{mem} = \frac{\rho_{mem}.l}{A} \tag{1.15}$$

ρ_{mem} is the specific resistance of the membrane ($\Omega.cm$), A is the active membrane surface in cm_2, l is the membrane thickness in (cm). The following expression for the specific resistance is used [Derbeli et al., 2017a]:

$$\rho_{mem} = \frac{181.6[1 + 0.03(\frac{I}{A}) + 0.062(\frac{T}{303})^2 \cdot (\frac{I}{A})^{2.5}}{[\beta - 0.634 - 3(\frac{I}{A})] \cdot \exp[4.18(T - 303)/T]} \tag{1.16}$$

The parameter β is an adjustable parameter with a maximum possible value of 23. This parameter depends on the membrane fabrication process and is a function of the relative humidity and the stoichiometric rate of the gas in the anode. Under ideal humidity conditions (100%), this parameter may have a value ranging from 14 to 20.

- The concentration polarization

The concentration losses are caused by the variation in the concentration of reactants. These losses can be calculated using Equation (1.17) [Reddy and Sudhakar, 2018]; where, ψ, J and J_{max} are, respectively, a constant parameter, the current density and the maximum current density.

$$V_{con} = \psi \cdot ln\left(1 - \frac{J}{J_{max}}\right) \tag{1.17}$$

1.4.3 PEM fuel cell stack output power

The output voltage under the load is approximately 0.6 V - 0.7 V. Therefore, it is necessary to have cells in series Figure 1.7, which finally forming a "stack" to achieve the sufficient voltage and the amount of power needed. The power generated by the PEMFC stack can be calculated using Equation (1.11); where N_{cell} represents the number of cells used in the stack [Reddy and Sudhakar, 2018].

$$P_{stack} = V_{FC} \cdot I \cdot N_{cell} \tag{1.18}$$

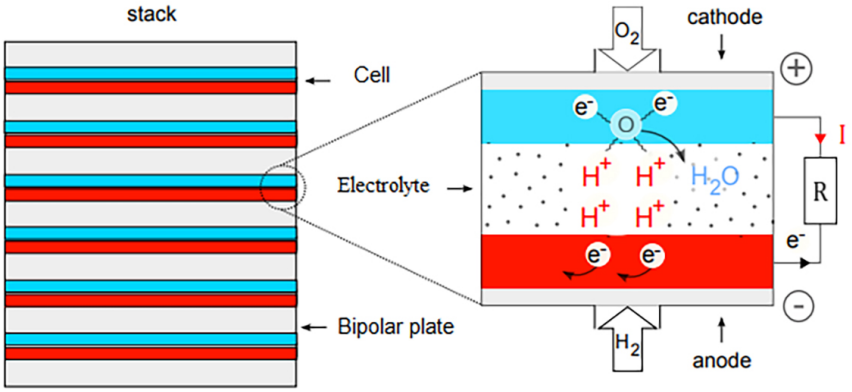

Figure 1.7: PEMFC stack.

1.5 Simulation model of PEMFC

The simulation modelling of a PEMFC plays a very important part in their development, because it facilitates the understanding of the phenomena involved in them. There are thus a large number of PEMFCs models, which generally each have their own specificities and uses, depending on the phenomena studied. The object of our study operates at variable temperatures. By using the mathematical Equation (1.10), Equation (1.12), Equation (1.14), Equation (1.17) and Equation (1.18), the PEMFC final diagram is represented by the Simulink block as shown in Figure 1.8.

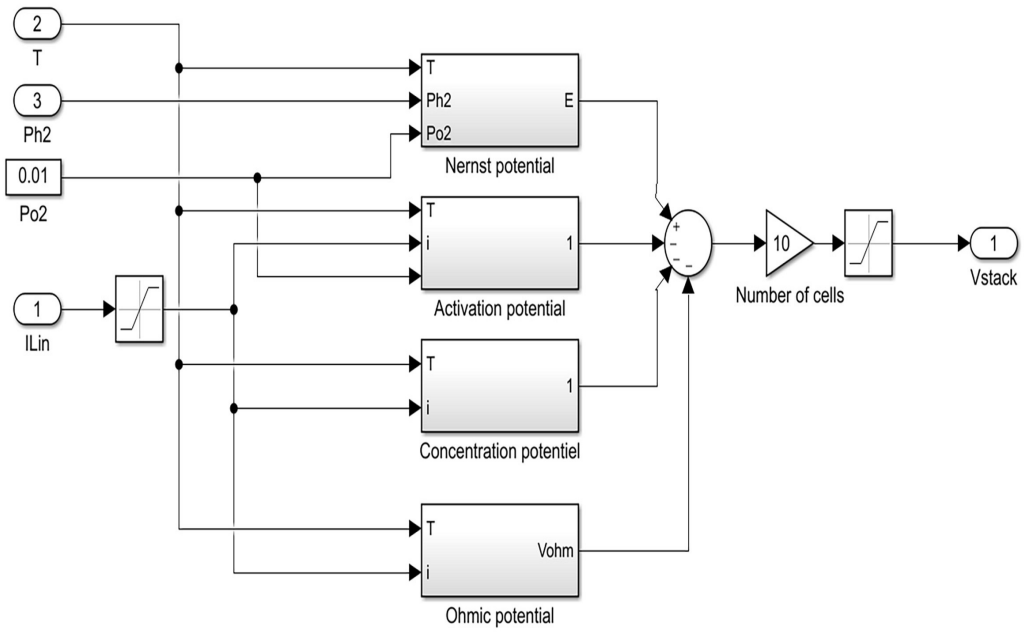

Figure 1.8: Dynamic model of a PEMFC.

1.5.1 The simulation results of a PEMFC

The data and characteristics of the PEMFC considered in our simulation are shown in Table. 1.2:

Parameter	**Value**
P_{max}	$55watt$
A	162 cm^2
β	23
l	$175.10^{-6}cm$
ψ	0.1 V
R_c	0.0003
J_{max}	0.062 $A.cm-1$
N_{cell}	10
ζ_1	0.9514 V
ζ_2	-0.00312 V/K
ζ_3	-7.4 $\cdot 10^{-5}$V/K
ζ_4	1.87 $\cdot 10^{-4}$V/K

Table 1.2: PEMFC model parameters.

- PEMFC polarization curve

The real potential of a PEMFC decreases to the Nernst potential because of the potential losses due to polarization or overvoltage phenomena which are of three types: activation polarization, ohmic polarization and concentration polarization which are indicated above. The polarization curves are a versatile diagnostic technique for the evaluation of the PEMFC performance and the effect of changes in particular operating parameters. From the polarization curve it is possible to distinguish between kinetic, ohmic and mass transport losses. The activation polarization region is this first part of a polarization curve, where current densities are low.

Using the previous Equation (1.11), Equation (1.12), Equation (1.14) and Equation (1.17), we can easily plot Figure 1.9, which represents the variation of the output voltage as a function of the current density I-V (polarization curve).

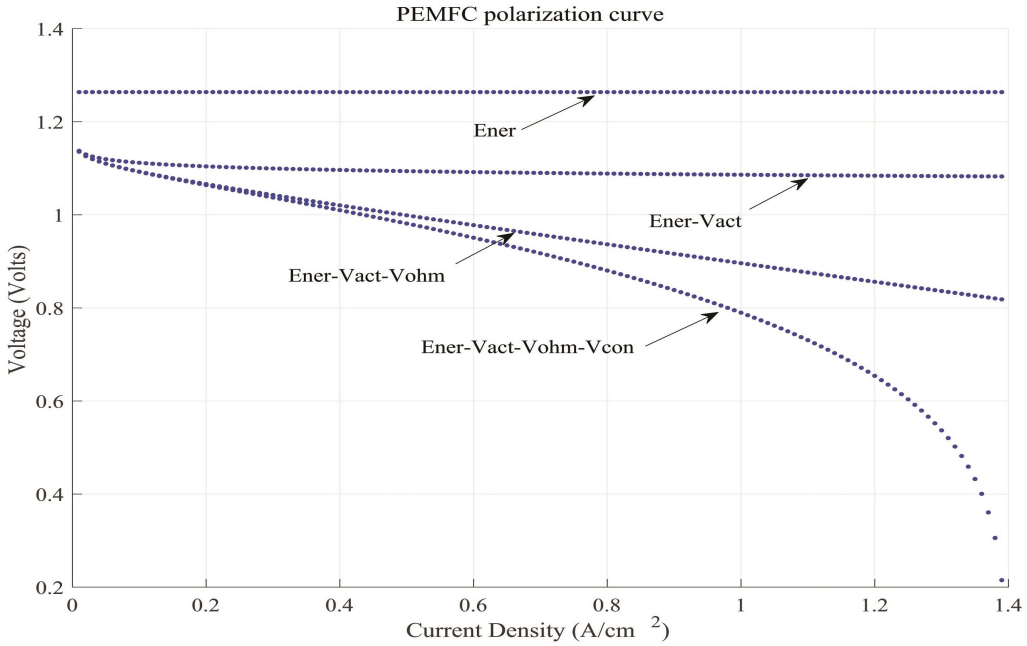

Figure 1.9: V-I Polarization curve of PEMFC.

- PEMFC output power curve

A PEMFC power density curve, which gives the power density delivered by a PEMFC as a function of the current density, can be constructed from the information in a PEMFC I-V curve. The power density curve is produced by multiplying the voltage at each point on the I-V curve by the corresponding current density. The current supplied by a PEMFC is directly proportional to the amount of fuel consumed (each mole of fuel provides n moles of electrons). Therefore, as PEMFC voltage decreases, the electric power produced per unit of fuel also decreases.

Using the previous Equation (1.6) and Equation (1.19) we can easily plot the Figure 1.10. According to this figure its noticed that the power of a single PEMFC gradually increases with increasing current density to reach a maximum at a certain time and then falls at still higher current densities. PEMFCs are designed to operate at or below the power density maximum.

At current densities below the power density maximum, voltage efficiency improves but power density falls. At current densities above the power density maximum, both voltage efficiency and power density fall.

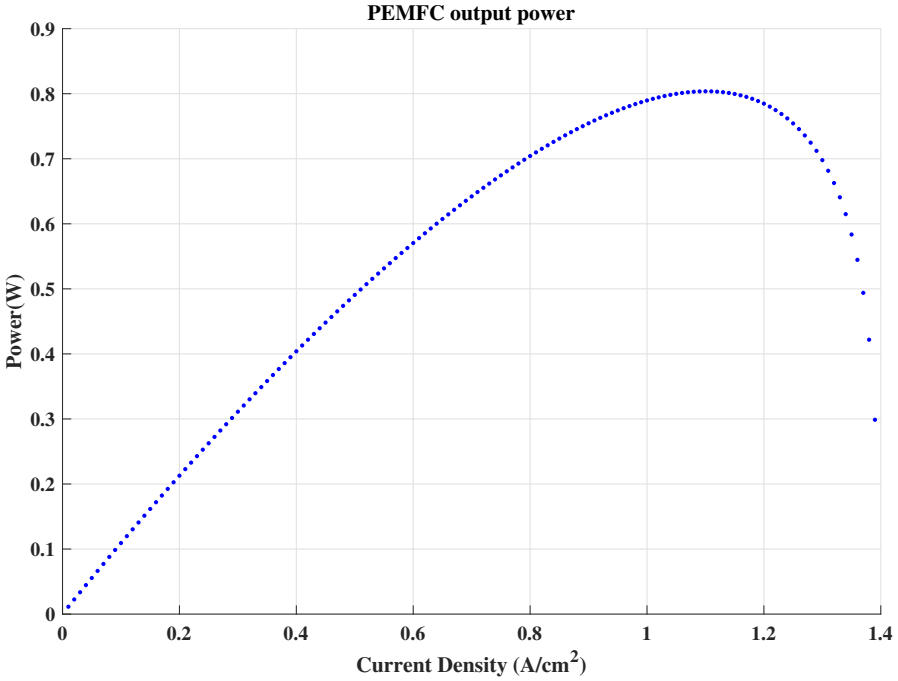

Figure 1.10: Power curve of single PEMFC.

It is essential to plot the curve of the power density as a function of current density in order to know the fuel cell capacities and its optimal operating conditions.

The obtained curve is parabolic, it grows linearly, then reaches a maximum and decreases rapidly, we can explain this behavior by the relations:

$$P_{cell} = V_{FC} \cdot I \tag{1.19}$$

In the longest trunk where ohmic polarizations predominate; We have :

$$V_{FC} = R \cdot I \quad ; \quad P_{cell} = R \cdot I^2 \tag{1.20}$$

This is the equation of a parabola

- The activation loss curve as a function of current density

The respective calculations of the activation loss as a function of current density are shown in Figure 1.11. It should be noted that the activation losses occur because the cell needs the energy to initiate reactions at both electrodes anode and cathode. As a result, a voltage drop is initialized inside the cell. With the increase of current density, the slope of the V/J curve changes. The activation polarization becomes less significant, while the ohmic effect becomes dominating. Note that the losses vary proportionally with the current density.

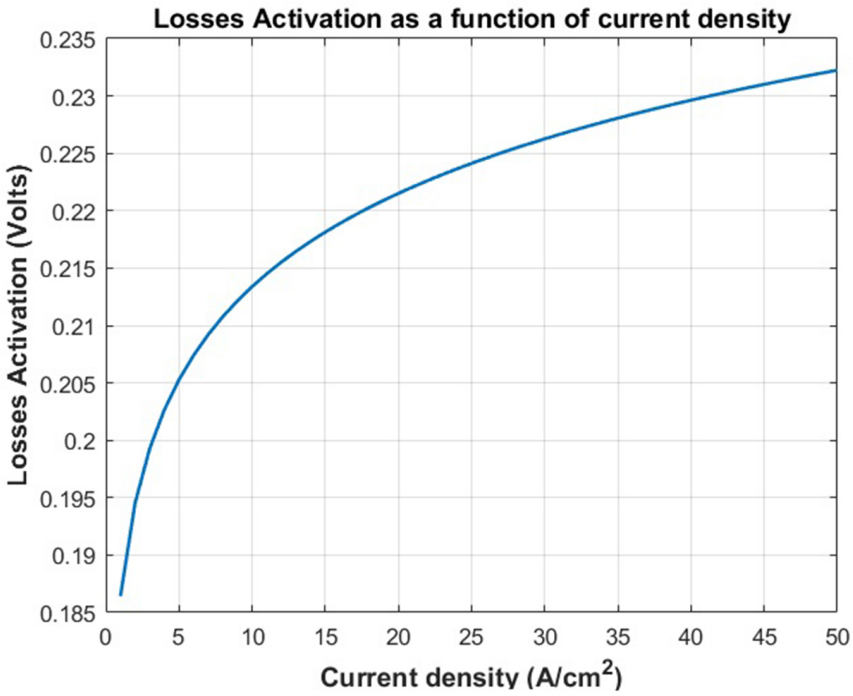

Figure 1.11: The activation loss curve (a).

According to Figure 1.11 its noticed that the activation losses is vary exponentially with the increase in current density.

- The activation loss curve as a function of temperature

The respective calculations of the activation loss as a function of temperature are shown in Figure 1.12. It is seen that the increase in cell temperature has impact on the activation losses. According to this figure its noticed that the activation losses vary linearly with increasing temperature, which means that increasing temperature affects the rate of activation losses.

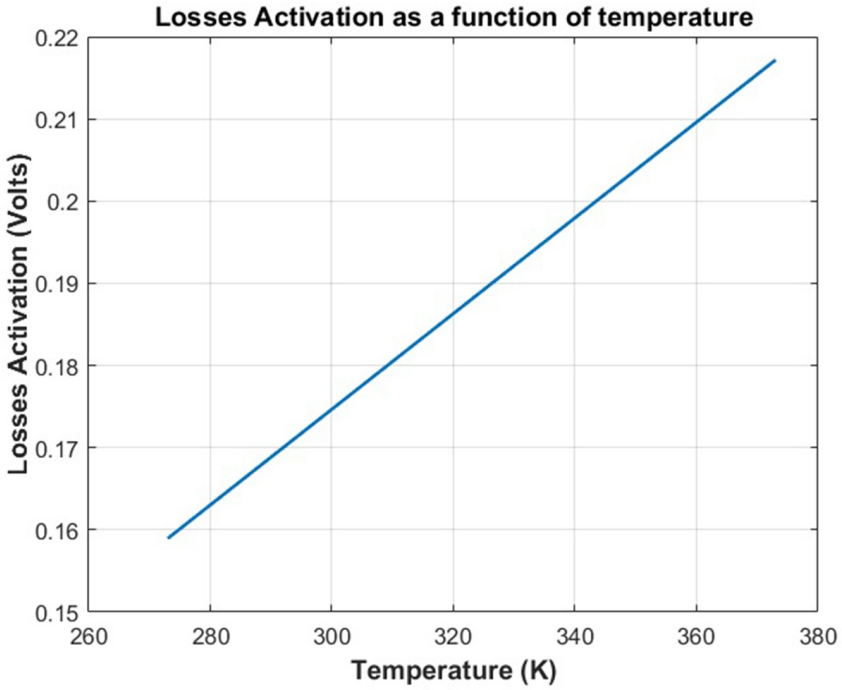

Figure 1.12: The activation loss curve (b).

Activation losses are other sources of thermal energy that cause a rise in temperature and originated in the electrodes.

The operating temperature causes an increase in activation losses and accelerates the kinetics of the reactions. It should be noted that the increase in temperature must be limited because it causes dehydration of the membrane.

- Impact of temperature on PEMFC performance

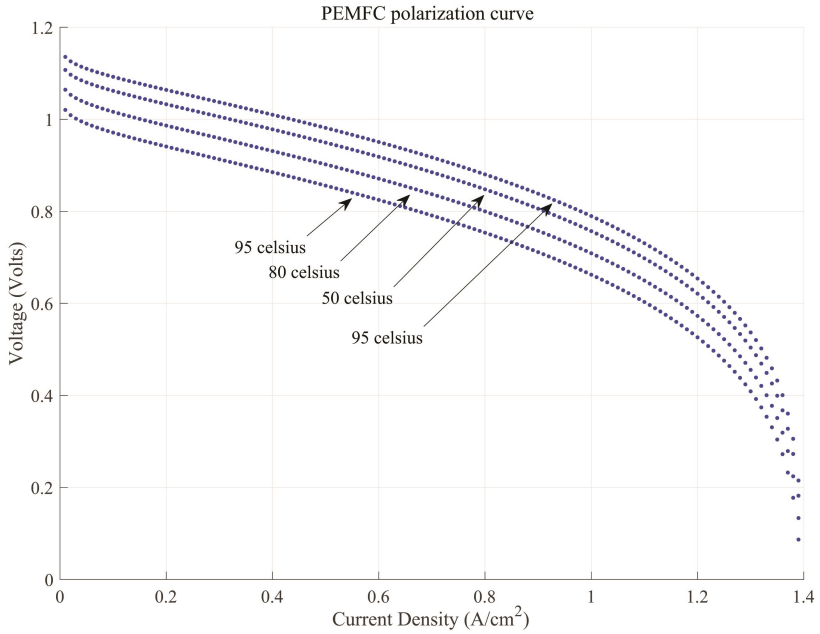

Figure 1.13: PEMFC polarization curve under different temperatures.

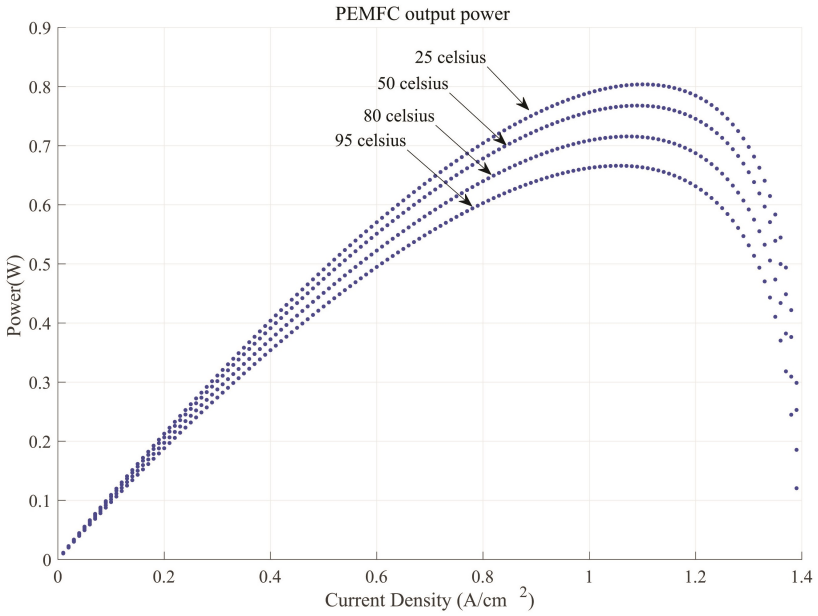

Figure 1.14: PEMFC power curve under different temperatures.

According to Figure 1.13 and 1.14, its noticed that the performance of

the PEMFC power system is enhanced by the change of the temperature. However, the rise in the temperature is not always lead to an increase in the power. For instance, the increase in temperature from 25 $°C$ to 95 $°C$ leads to a decrease in the output power and that, it has been experimentally proven in chapter 6.

- Impact of pressure on PEMFC performance

According to Figure 1.15 and 1.16, the performance of the PEMFC power system is enhanced by the change of the operating pressure from 0.1 bar to 1.25. Operating pressure can influence the real PEMFC performance by affecting the PEMFC open circuit voltage, the partial pressures of the reactant gases, exchange current densities, and mass transfer in the electrode reactions. Usually, the performance of a PEMFC in terms of voltage and power density can be improved by increasing the operating pressure. However, pressurization of the real PEMFC system can bring about increased gas permeation, water management issues, increased cost, size, and weight.

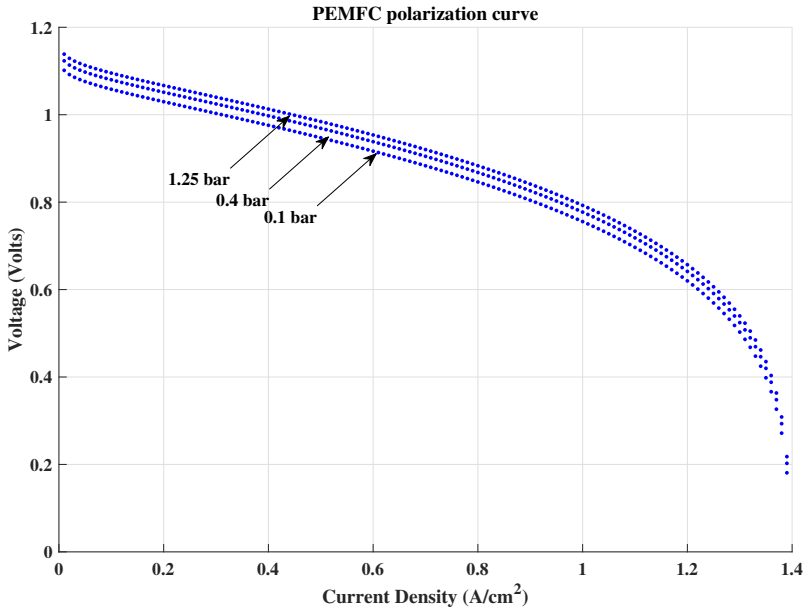

Figure 1.15: PEMFC polarization curve under different pressures.

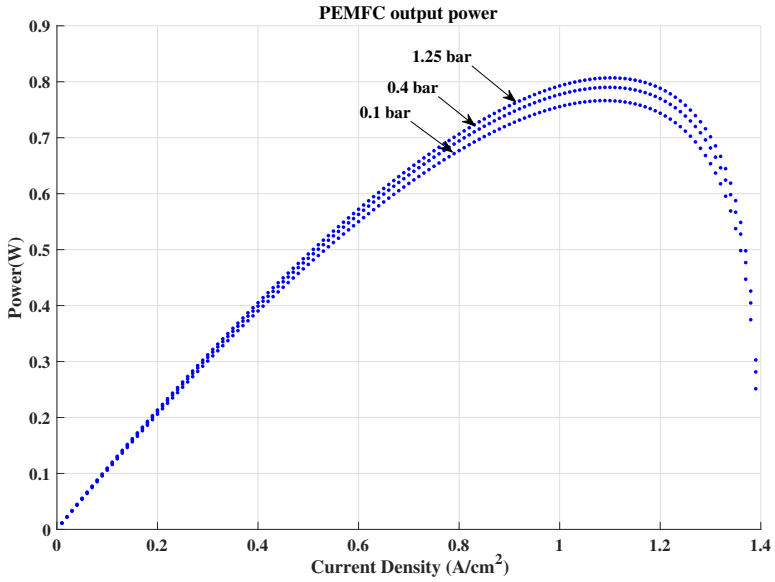

Figure 1.16: PEMFC power curve under different temperatures.

1.6 Conclusion

At the beginning of this first chapter, we presented the energy problem in the world. Hydrogen energy is renewable energy for the future. The PEMFC can efficiently transform chemical energy into electrical energy. In this context, we are interested in this work only with the proton exchange membrane polymer PEM (Proton Exchange Membrane) fuel cells for the reasons of their advantages and also is considered as the most suitable for many applications such as transportation, portable applications, space application.... ext. Furthermore, we present the characteristics curves of the PEMFC by simulation as well as the impact of the temperature and the gas pressures on his performance.

Chapter 2

POWER ELECTRONICS INTERFACES FOR PEMFC

> We will make electricity so cheap that only the rich will burn candles.
>
> *Thomas A Edison*

2.1 Introduction

As mentioned in the second chapter, a PEMFC is a non-linear system which is affected by the variable conditions such as inlet gases pressures and change in temperatures. In order to ensure the power conversion from the PEMFC to the load, an adaptation stage is required, and this can be done by direct coupling of a suitable load or by inserting an electronic device between the PEMFC and the electrical load. This device is a static DC/DC converter equipped with an insulated gate bipolar transistor (IGBT) which can be controlled by a command law. In order to design a more efficient power interface, a detailed study is made on the DC-DC static converters in the continuous conduction mode (CCM). In this study, we will choose the DC/DC boost converter, thanks to its simple structure and its highest

voltage transformation ratio compared to other typologies. After determining the structure of the converter adopted, we will present some existing control techniques which allow the PEMFC to operate at an adequate power point. The design of an adaptation stage equipped with a control algorithm makes it possible to optimize energy conversion and to connect the PEMFC to its load easily.

2.2 Direct connection PEMFC-load

Currently, many applications have a direct connection between the PEMFC and the load are still exist. This connection in the absence of stage electronics is simple, reliable and inexpensive. However, it does not guarantee an optimal transfer of energy from the PEMFC power system to the load. Another disadvantage is that the direct connection of the PEMFC is not valid on an AC load because the PEMFC provides a direct current. For the connection of a PEMFC to an AC load, an inverter-type adaptation stage is required [Escobar et al., 2011]. This configuration is shown in Figure 2.1, the anti-reverse diode placed between the PEMFC and the load serves as protection. Indeed, if this load were a battery when the module is not illuminated, it could function as a receiver. The battery could therefore discharge on the PEMFC and, in addition damage it.

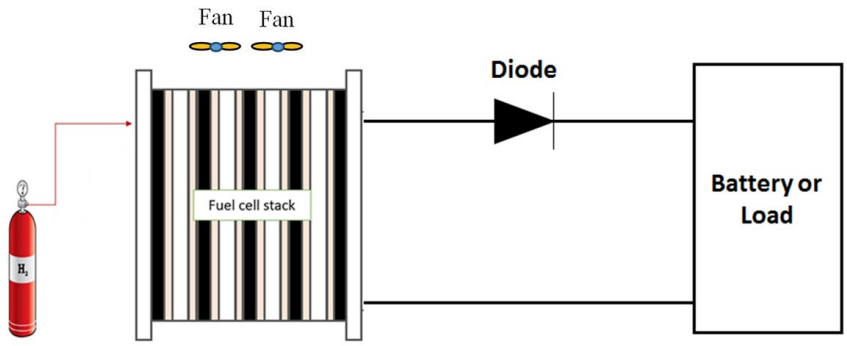

Figure 2.1: PEMFC-Charge direct connection through a diode.

2.3 Indirect connection PEMFC-load through an adaptation stage

The indirect connection consists of an adaptation stage called DC-to-DC converters, which are some of the most widely used power electronics circuits thanks to their high conversion efficiency and adjustable output voltage. These converters used for electronic devices are designed to regulate the output voltage against the changes of the input voltage and load current. This leads to the requirement of more advanced control methods to meet the real demand. Many control methods are developed in the literature for the control of DC-DC converters. As shown in Figure 2.2, the closed-loop for the indirect connection consists of a PEMFC power system, a DC-to-DC converter, a control technique and finally, a load.

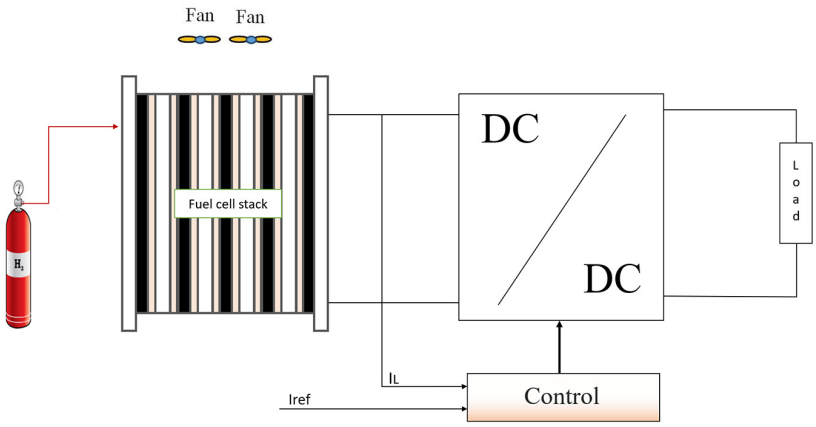

Figure 2.2: Principle of indirect adaptation with control technique.

2.3.1 Adaptation stages

The adaptation stages are represents in DC-DC converters which have different possible typologies such as: step-down (buck), step-up (boost), step-down, step-up (buck-boost, cuk, sepic). These DC-DC converters are an electronics circuits or electromechanical devices that convert a source of

direct current (DC) from one voltage level to another.

The boost converter

A DC-DC converter type boost. It is essentially composed of a switch K (like IGBT or MOSFET) and a diode D. The switch K is controlled by a PWM signal with a fixed chopping period T_d and ratio cyclic variable α. The conduction of the two switches is complementary, when K is closed, D is open; and when, K is open, D is closed. During each period, K is immediately closed at $t = 0$ to αT_d and open from αT_d to T_d. There are two operating modes depending on whether the current in inductance cancels out discontinuous conduction mode (DCM) or not CCM. We are interested in the second case, which is the most important. Figure 2.3 gives the block diagram of this converter, the conduction intervals of the switch and the diode, as well as the waveforms of its currents (left) and voltages (right).

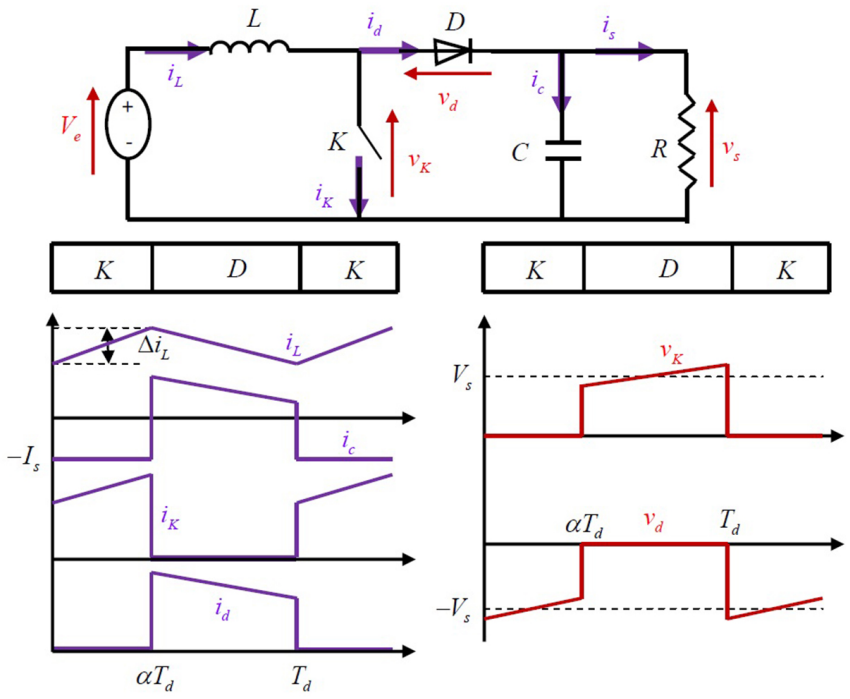

Figure 2.3: Waveforms of boost converter currents and voltages.

When the switch K is closed ($0 < t < \alpha T_d$), the converter circuit becomes Figure 2.4:

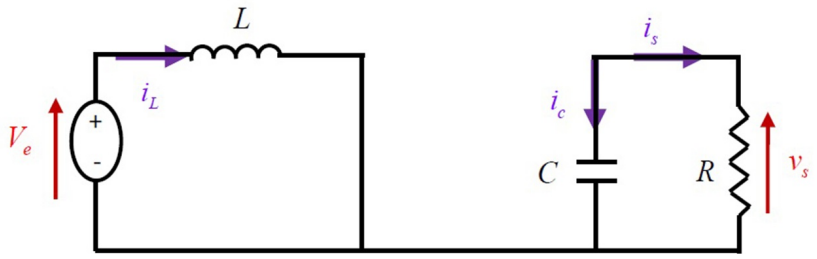

Figure 2.4: Boost converter equivalent circuit when the switch is closed.

$$L\frac{di_L}{dt} = V_e \tag{2.1}$$

$$i_L = I_{min} + \frac{V_e}{L}t \tag{2.2}$$

with I_{min} the minimum value of the current in the inductance.

At the instant $t = \alpha T_d$, the current in the inductance reaches its maximum value I_{max}

$$I_{max} = I_{min} + \frac{V_e}{L}\alpha T_d \tag{2.3}$$

When the switch K is open ($\alpha T_d < t < T_d$), the converter circuit will be as shown in Figure 2.5.

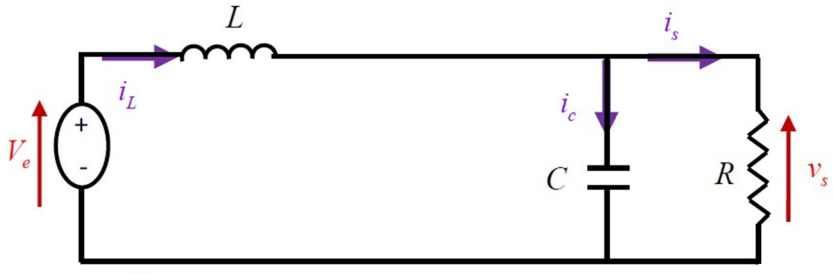

Figure 2.5: Boost converter equivalent circuit when the switch is opened.

$$L\frac{di_L}{dt} = V_e - V_s \tag{2.4}$$

$$i_L = I_{max} + \frac{V_e - V_s}{L}(t - T_d) \tag{2.5}$$

At the instant $t = T_d$, the current in the inductance returns to its minimum value I_{min}

$$I_{min} = I_{max} + \frac{V_e - V_s}{L}(1 - \alpha)T_d \tag{2.6}$$

Let $\Delta i_L = I_{max} - I_{min}$ be the rate of change of the current in the inductor.

By equalizing the values of the current ripple taken from Equations (2.3) and (2.6), we can deduce the average value of the output voltage V_s:

$$V_s = \frac{1}{1 - \alpha}V_e \tag{2.7}$$

Note that we can control the output voltage of the boost converter by varying its input voltage or by its duty cycle. This is always between 0 and 1, then the assembly operates as a voltage booster.

By applying the principle of conservation of power between the input and the output of the converter, we can establish the average value of the current in the inductor according to the average current in the load and the duty cycle:

$$I_L = \frac{1}{1 - \alpha}I_s \tag{2.8}$$

From expression (2.3), we express the current ripple in the inductor:

$$\Delta i_L = \frac{\alpha V_e}{L}T_d = \frac{\alpha V_e}{L f_s} \tag{2.9}$$

With f_s the switching frequency.

During the first operating sequence ($0 < t < \alpha T_d$), only the capacitor gives energy to the load, we can write:

$$C\frac{dv_s}{dt} = -i_s \tag{2.10}$$

Then the output voltage ripple can be expressed by:

$$\Delta V_s = \frac{\alpha i_s}{Cfs} = \frac{\alpha V_e}{(1-\alpha)RCf_s} \tag{2.11}$$

From the analysis of the two operating sequences, it can be seen that the stresses on the controlled switch and the diode are the same in current and in voltage.

$$i_{K,max} = i_{d,max} = I_{max} = I_L + \frac{\Delta i_L}{2} = \frac{I_s}{1-\alpha} + \frac{\Delta i_L}{2} \tag{2.12}$$

$$V_{K,max} = |V_{d,max}| = V_{s,max} = V_s + \frac{\Delta V_s}{2} = \frac{V_e}{1-\alpha} + \frac{\Delta V_s}{2} \tag{2.13}$$

The buck converter

We proceed in the same way in the study of the buck converter. Figure 2.6 shows the structure and waveforms of current and voltage of this converter which is characterized by the serial arrangement of the switch with the source. The output voltage in average value, the current ripple in the inductor and the output voltage ripple are given respectively by:

$$V_s = \alpha \cdot V_e \tag{2.14}$$

$$\Delta i_L = \frac{\alpha(1-\alpha) \cdot V_e}{Lf_s} \tag{2.15}$$

$$\Delta V_s = \frac{\alpha(1-\alpha) \cdot V_e}{8CLf_s^2} \tag{2.16}$$

Therefore, the converter is a voltage step-down.

The average current flowing through the inductance is equal to the average current in the load:

$$I_L = I_s \tag{2.17}$$

The constraints on the controlled switch and the diode are the same.

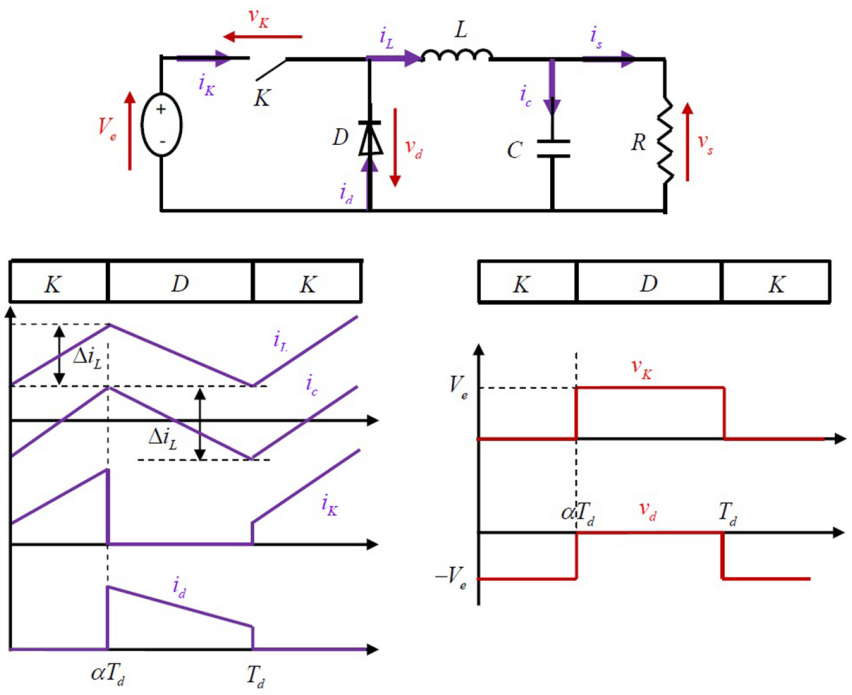

Figure 2.6: Buck converter currents and voltages waveforms.

In tension, we have:

$$V_{K,max} = |V_{d,max}| = V_e \tag{2.18}$$

And in the current we have:

$$i_{K,max} = i_{d,max} = I_{max} = I_L + \frac{\Delta i_L}{2} \tag{2.19}$$

The buck-boost converter

The topology and the current and voltage waveforms obtained from this converter are shown in Figure 2.7. The average output voltage is given by:

$$\Delta V_s = \frac{\alpha V_e}{1-\alpha} \tag{2.20}$$

The current ripple in the inductor is given by:

$$\Delta I_L = \frac{\alpha V_e}{L f_s} \tag{2.21}$$

and the output voltage ripple:

$$\Delta V_s = \frac{\alpha i_s}{C f_s} = \frac{\alpha^2 V_e}{(1-\alpha) R C f_s} \tag{2.22}$$

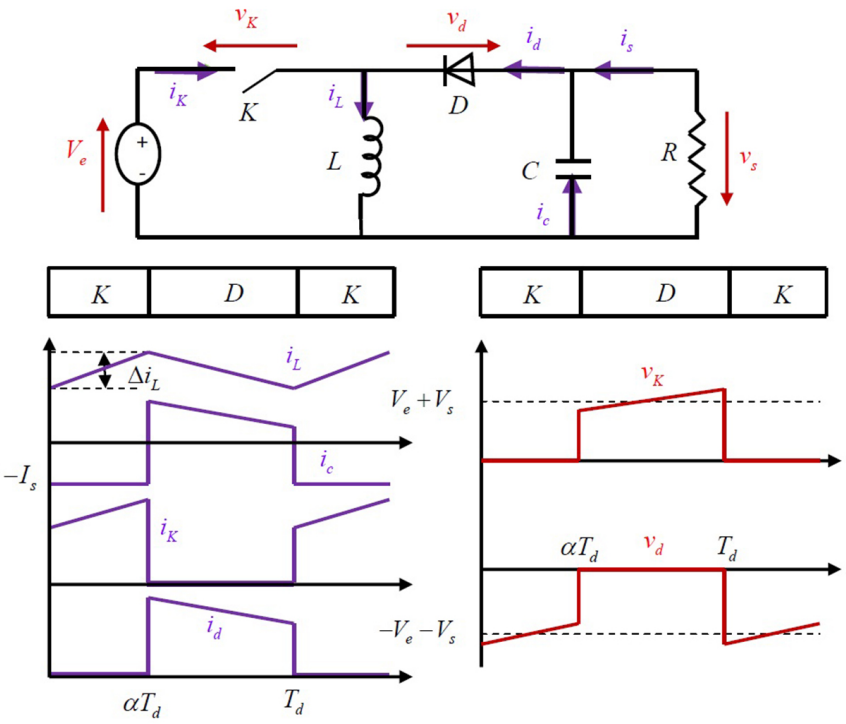

Figure 2.7: The buck-boost converter currents and voltages waveforms.

The output voltage of the buck-boost converter is negative relative to the input voltage. Its amplitude may be greater or less than that of the input voltage, depending on the value of the duty cycle. It is a voltage step-up-step-up-inverter. The average current flowing through the inductance is given by:

$$I_L = \frac{I_s}{1-\alpha} \tag{2.23}$$

The voltage and current constraints on the controlled switch and the diode are the same:

$$V_{K,max} = |V_{d,max}| = V_{s,max} + V_e = \frac{V_e}{1-\alpha} + \frac{\Delta V_s}{2} \tag{2.24}$$

$$i_{K,max} = i_{d,max} = I_{max} = \frac{I_s}{1-\alpha} + \frac{\Delta i_L}{2} \tag{2.25}$$

The cuk converter

Figure 2.8 illustrates the electrical circuit of the cuk converter and its current and voltage waveforms. The average output voltage is given by:

$$\Delta V_s = \frac{\alpha V_e}{1-\alpha} \tag{2.26}$$

Note that the transformation ratio is similar to that of buck-boost. Likewise, we can say that it is a step-down-step-up-inverter in voltage.

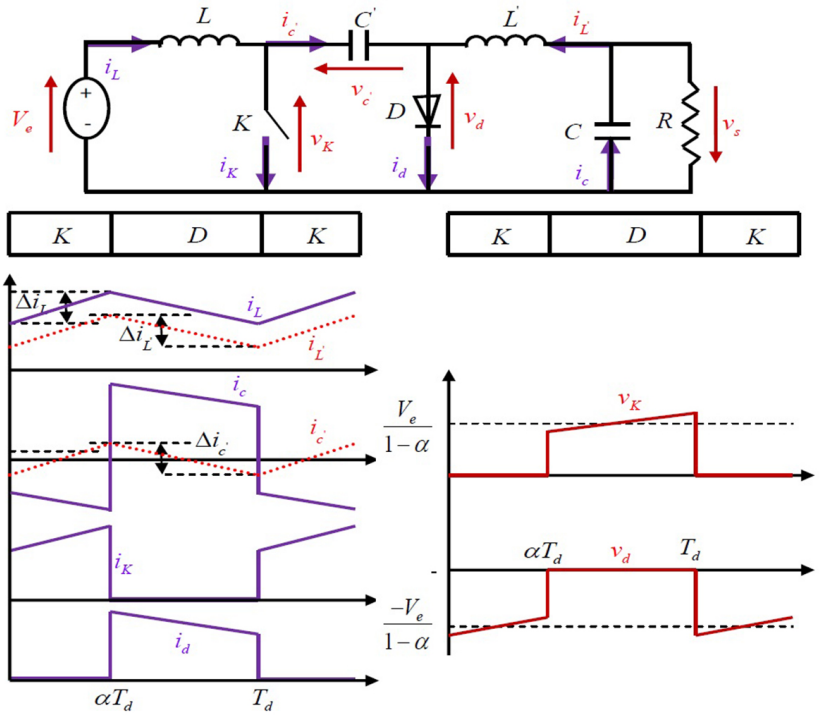

Figure 2.8: Cuk converter currents and voltages waveforms.

The expression relating the average currents is:

$$I_L = \left(\frac{\alpha}{1-\alpha}\right) I'_L = \left(\frac{\alpha}{1-\alpha}\right) I_s \tag{2.27}$$

The current ripples in the two inductors:

$$\Delta i_L = \frac{\alpha V_e}{L f_s} \tag{2.28}$$

$$\Delta i_{L'} = \frac{\alpha V_e}{L' f_s} \tag{2.29}$$

The output voltage ripple:

$$\Delta V_s = \frac{\Delta i_{L'}}{8 C f_s} = \frac{\alpha V_e}{8 L' C f_s^2} \tag{2.30}$$

The voltage ripple across the capacitor C':

$$\Delta V_{C'} = \frac{(1-\alpha) I_L}{C' f} = \frac{\alpha^2 V_e}{(1-\alpha) R C' f_s} \tag{2.31}$$

The constraints on the controlled switch and the diode are:

$$V_{K,max} = |V_{d,max}| = V_{C',max} = \frac{V_e}{1-\alpha} + \frac{\Delta V_{C'}}{2} \tag{2.32}$$

$$i_{K,max} = i_{d,max} = I_L + I_{L'} + \frac{\Delta I_L + \Delta I_{L'}}{2} \tag{2.33}$$

The sepic converter

Likewise, we start by giving the principle circuit of the sepic converter and its current and voltage waveforms obtained in continuous conduction mode in Figure 2.9. The characteristics of this converter are identical to those of the cuk, but it is not a voltage inverter.

The average output voltage is given by:

$$V_s = \frac{\alpha}{1-\alpha} V_e \tag{2.34}$$

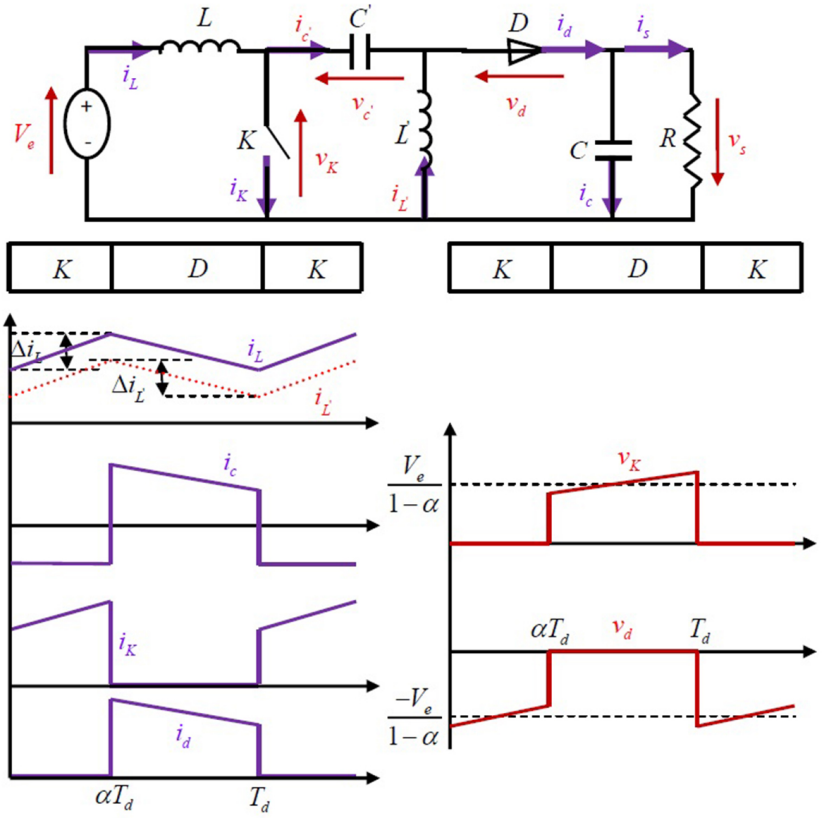

Figure 2.9: Sepic converter currents and voltages waveforms.

The expression relating the mean values of the currents is:

$$I_L = \left(\frac{\alpha}{1-\alpha}\right) I'_L = \left(\frac{\alpha}{1-\alpha}\right) I_s \tag{2.35}$$

The current ripples in the two inductors:

$$\Delta i_L = \frac{\alpha V_e}{L f_s} \tag{2.36}$$

$$\Delta i_{L'} = \frac{\alpha V_e}{L' f_s} \tag{2.37}$$

The output voltage ripple:

$$\Delta V_s = \frac{\alpha^2}{(1-\alpha)} \frac{V_e}{RC f_s} \tag{2.38}$$

The voltage ripple across the capacitor C':

$$\Delta V_{C'} = \frac{(1-\alpha)I_L}{C'f_s} = \frac{\alpha^2}{(1-\alpha)}\frac{V_e}{RC'f_s} \tag{2.39}$$

The constraints on the controlled switch and the diode are:

$$V_{K,max} = |V_{d,max}| = V_{C',max} + V_{s,max} = \frac{V_e}{1-\alpha} + \frac{\Delta V_{C'} + \Delta V_s}{2} \tag{2.40}$$

$$i_{K,max} = i_{d,max} = I_L + I_{L'} + \frac{\Delta I_L + \Delta I_{L'}}{2} \tag{2.41}$$

2.3.2 Analysis summary and choice of converter

A DC generator, for instance, a PEMFC stack or a solar panel. Are preferable to put a voltage step-up device as an impedance adapter stage between the source and the charge. All the converters mentioned above, except the buck, can play this role of voltage booster. In fact, the buck-boost, cuk and sepic structures are lifting for a duty cycle greater than one-half. If we look at the complexity of the structures, the boost is the simplest. The voltage and current stresses on switches and diodes are almost similar for the different lift typologies.

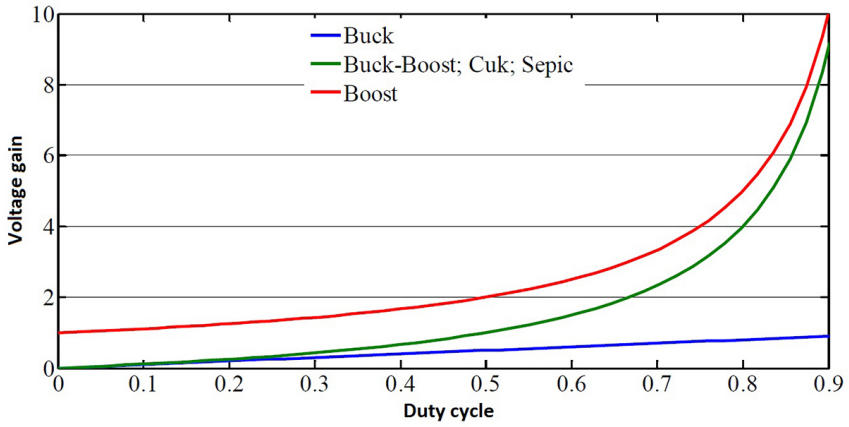

Figure 2.10: Evolution of the voltage gain as a function of the duty cycle of the converters [Huang, 2009].

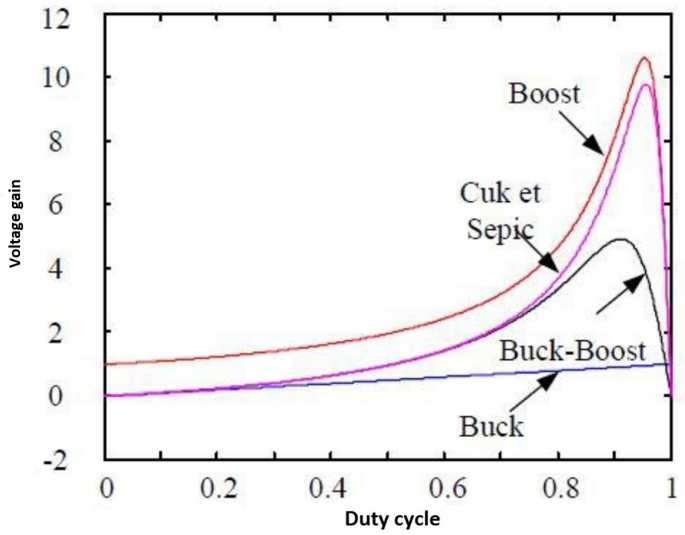

Figure 2.11: Evolution of the voltage gain taking into account the parasitic elements of the converters [Huang, 2009].

Table 2.1: Summary of the characteristics of DC-DC converters.

Converters	**Gain in tension** $\frac{V_s}{V_e}$	**Constraints in voltage** $V_{K,max} = \lvert V_{d,max} \rvert$	**Constraints in current** $i_{K,max} = i_{d,max}$
Boost	$\frac{1}{1-\alpha}$	$\frac{V_e}{1-\alpha} + \frac{\Delta V_s}{2}$	$\frac{I_s}{1-\alpha} + \frac{\Delta i_L}{2}$
Cuk	$\frac{\alpha}{1-\alpha}$	$\frac{V_e}{1-\alpha} + \frac{\Delta V_{C'}}{2}$	$I_L + I_{L'} + \frac{\Delta I_L + \Delta I_{L'}}{2}$
Sepic	$\frac{\alpha}{1-\alpha}$	$\frac{V_e}{1-\alpha} + \frac{\Delta V_{C'} + \Delta V_s}{2}$	$I_L + I_{L'} + \frac{\Delta I_L + \Delta I_{L'}}{2}$
Buck-Boost	$\frac{\alpha}{1-\alpha}$	$\frac{V_e}{1-\alpha} + \frac{\Delta V_s}{2}$	$\frac{I_s}{1-\alpha} + \frac{\Delta i_L}{2}$
Buck	α	V_e	$\mathrm{I_L} + \frac{\Delta i_L}{2}$

If we compare them from the point of view of voltage gain, also the boost takes the first place as shown in Figure 2.10 which gives the evolution of the voltage gain as a function of the duty cycle. Finally, a comparison

of these converters is given in Table. 2.1 which summarizes the analysis made previously on the various converters. We can also notice that the diode D presents in sepic and boost converters can play the protective role of the photo-voltaic system, which makes it possible to dispense with the non-return diode and to save costs compared to other typologies. For to better differentiate between converters, HUANG plotted the voltage gain as a function of the duty cycle Figure 2.11 taking into account the parasitic elements of the converters [Huang, 2009].

2.4 Study of a PEMFC structure based on a DC/DC converter type boost

2.4.1 Description of the PEMFC structure based on a boost converter

In this thesis, we will focus on the application of the control applied to a DC/DC type boost linked to a PEMFC. The converter whose equations in continuous conduction mode will be established later. When we speak of continuous conduction mode, the current i_L passing through the inductance never cancels out. The selection of the best power switching element for static converters is based on two aspects: the conduction voltage drop and the switching speed [Wang et al., 2013]. Due to these aspects, it is better to use the MOSFET having high switching speed for low voltage applications such as our case. But, the boost converters available in the VITORIA lab, are multi-application converters and are built with IGBT transistors. So our converter is sized according to the prototype made available by the laboratory. It consists of passive filtering elements, a diode and an IGBT.

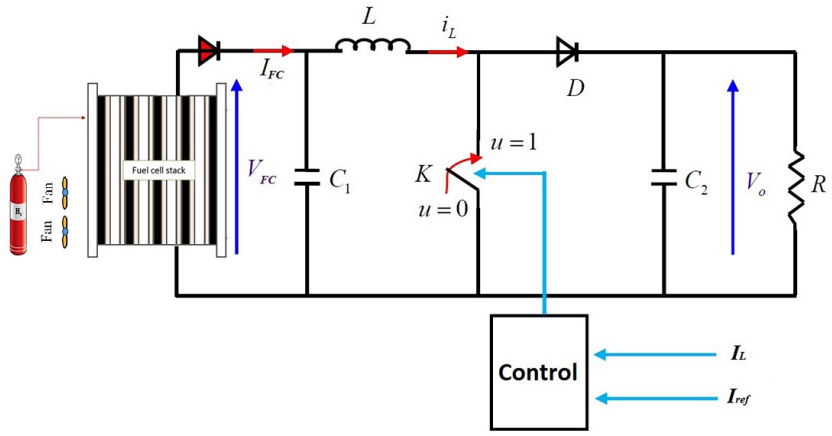

Figure 2.12: PEMFC conversion chain based on a DC/DC converter type boost.

Figure 2.12 illustrates the diagram of the PEMFC conversion chain, which is to be studied. With this structure, it is possible to dispense with the non-return diode. This reduces the complexity and cost of the system.

2.4.2 Boost converter state space modelling

A boost converter is a switching power supply that converts a DC voltage into another DC voltage of greater value. Its operation in continuous conduction mode. It includes two sequences depending on whether the controllable switch is closed or open. Figure 2.13 (a, b, c) respectively show the overall structure of the boost, the structure with the switch closed, the structure with the switch open. To model the converter, one applies the laws of Kirchhoff (law of meshes and law of nodes) to the electric circuits characterizing the two operating sequences.

The first sequence is characterized by $u = 1$, the switch closed, and the diode open. The equations which govern the converter are given by:

$$\begin{cases} \frac{di_L}{dt} = \frac{1}{L}(V_{FC}) \\ \\ \frac{dV_o}{dt} = \frac{1}{RC}(-V_o) \end{cases} \tag{2.42}$$

If we set $x = [x_1, x_2]^T = [i_L, V_o]^T$, then the expression (2.42) can be written:

$$\begin{bmatrix} \dot{x}_1 \\ \dot{x}2 \end{bmatrix} = \begin{bmatrix} 0 & 0 \\ 0 & -\frac{1}{RC} \end{bmatrix} . \begin{bmatrix} x_1 \\ x_2 \end{bmatrix} + \begin{bmatrix} \frac{1}{L} \\ 0 \end{bmatrix} V_{FC} \tag{2.43}$$

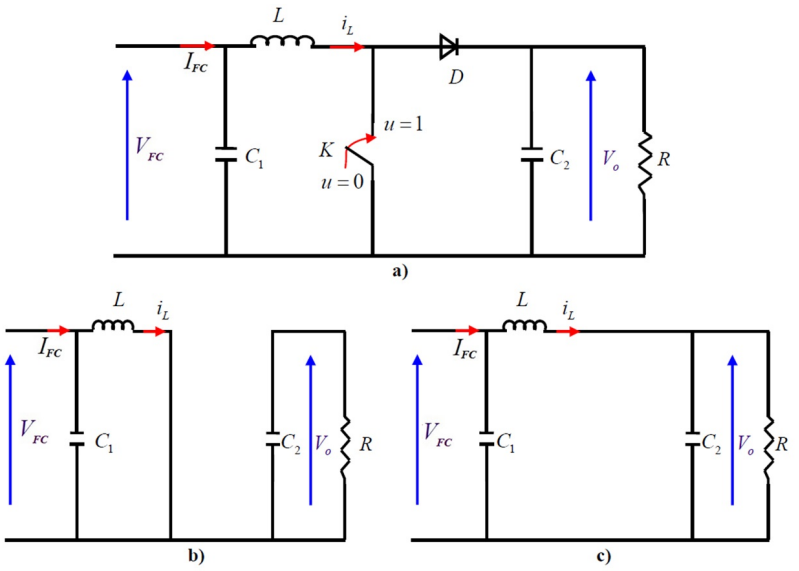

Figure 2.13: Basic electrical diagram of the boost converter.

The second operating sequence is characterized by u = 0, the switch opens, and the diode closed. The system of equations that controls the converter in the "off" state is presented below:

$$\begin{cases} \frac{di_L}{dt} = \frac{1}{L}(V_{FC} - V_o) \\ \\ \frac{dV_o}{dt} = \frac{1}{C}(i_L - i_o) \end{cases} \tag{2.44}$$

If we set $x = [x_1, x_2]^T = [i_L, V_o]^T$, then the expression (2.44) can be written:

$$\begin{bmatrix} \dot{x}_1 \\ \dot{x}2 \end{bmatrix} = \begin{bmatrix} 0 & -\frac{1}{L} \\ \frac{1}{C} & -\frac{1}{RC} \end{bmatrix} \cdot \begin{bmatrix} x_1 \\ x_2 \end{bmatrix} + \begin{bmatrix} \frac{1}{L} \\ 0 \end{bmatrix} V_{FC} \tag{2.45}$$

In state space description, if the state equations of two modes are described as following [Vangari et al., 2015]:

$$\begin{aligned} \dot{x} &= A_1 x + B_1 u \quad (Switch"1") \\ \dot{x} &= A_2 x + B_2 u \quad (Switch"0") \end{aligned} \tag{2.46}$$

Then the average state space model is:

$$\dot{x} = \bar{A}x + \bar{B}u \tag{2.47}$$

Where, $\bar{A} = A_1 d + A_2(1-d)$ and $\bar{B} = B_1 d + B_2(1-d)$

Averaging the state space matrix of two different working modes using equations (2.43), (2.45), (2.46) and (2.47), we get the average model as a function of the duty cycle.

$$\begin{cases} \begin{bmatrix} \dot{x}_1 \\ \dot{x}_2 \end{bmatrix} = \begin{bmatrix} 0 & \frac{-(1-d)}{L} \\ \frac{(1-d)}{C} & -\frac{1}{RC} \end{bmatrix} \cdot \begin{bmatrix} x_1 \\ x_2 \end{bmatrix} + \begin{bmatrix} \frac{1}{L} \\ 0 \end{bmatrix} V_{FC} \\ \\ y = \begin{bmatrix} 0 & 1 \end{bmatrix} \cdot \begin{bmatrix} x_1 \\ x_2 \end{bmatrix} \end{cases} \tag{2.48}$$

2.5 Conclusion

DC/DC converters play key roles within various applications that fulfil important functions in modern society, such as those of renewable energy conversion systems, electric vehicular applications or power delivery devices. These adaptation stages are required in order to convert the direct current DC from a voltage level to another level by a control technique that activates the trigger of the DC/DC converter IGBT. In this chapter, state-space modelling for boost converter is represented. In addition, we compare the boost converter, cuk and the sepic converter. By comparison, the buck-boost, cuk and sepic structures are lifting for a duty cycle greater than one-half. If we look at the complexity of the structures, the boost is the simplest, which we can use in our experience.

Chapter 3

CONVENTIONAL CONTROLLERS

> Automation is no longer just a problem for those working in manufacturing. Physical labour was replaced by robots; mental labour is going to be replaced by AI and software.
>
> *Andrew Yang*

3.1 Introduction

PI and PID controllers meet more than 90% of industrial needs. Unfortunately, despite the experience gained over the years, the values are chosen for the parameters P, I and D are not always satisfactory, nor adapted to the process to be controlled.

The first centrifugal type controllers appeared around 1750 to regulate the speed of windmills, followed in 1788 by the famous speed controller of a steam engine by James Watt.

In 1942, ZN proposed two approaches to easily find the optimum parameters

for a given installation. Over the years, ZN proposals have been adapted or modified as needed.
In the early 1990s, with the aim of providing simple adjustment rules that were more efficient than those of ZN, his collaborators analyzed the dynamic behavior of a large number of processes. This analysis led to the establishment of tables used to calculate the parameters P, I and D from simple measurements. Therefore, the PID controller is well suited to most industrial type processes, and it is relatively robust with respect to variations in process parameters, when one is not too demanding on the performance of the closed loop compared to those of the open loop (for example, very large acceleration of the response or very large increase in closed-loop damping) [O'dwyer, 2009].

3.2 Conventional controllers

Conventional controllers are the most widely-used in industrial applications. They are structurally simple and exhibit robust performance over a wide range of operating conditions. In the absence of the complete knowledge of the process, these controllers are the most efficient of choices. Three main parameters involved these controllers are the P action, I action and the D action. The P part is responsible for following the desired set-point, while the I and D part account for the accumulation of past errors and the rate of change of error in the process respectively. Where, the conventional controllers are based on these following principles:

- The control brings together all the techniques used to control a physical quantity. For example: Pressure, temperature, flow, level etc ...
- The controlled quantity is the physical quantity that one wishes to control. It gives its name to control. For example: speed control.
- The setpoint is the value that the controlled variable must take.

- The manipulated variable is the physical quantity that has been chosen to control the controlled variable. It is not generally of the same nature as the controlled quantity.
- The disturbing quantities are the physical quantities that influence the controlled quantity. They are not generally of the same nature as the controlled quantity.
- The regulating device is the element which acts on the regulating quantity [Solihin et al., 2011].

3.2.1 The overall objective of control

It can be summed up by these three key words: measure, compare, correct. However, each process has its own requirements, and each device has its own operating conditions. It is therefore essential that the control be designed to meet the specific needs related to safety, production requirements and equipment.

3.2.2 Control loop

A control loop is the fundamental building block of industrial control systems. It consists of all the physical components and control functions necessary to automatically adjust the value of a measured process variable to equal the value of a desired set-point. A control loop must include at least the following elements:

- A measurement sensor.
- A transmitter often integrated into the sensor.
- A controller; an actuator.

It is often supplemented by: a recorder, converters, safety devices.
The controller receives two pieces of information:

- The measurement signal from the sensor.
- The set point (which can be local or external).

Depending on the difference between these two values and the calculation algorithm for which it has been configured, it delivers an output signal directed to the actuator in order to cancel this difference and bring the measurement back to the value of set point [Méndez-Barrios et al., 2008].

3.3 Types of control loops

There are two common control loop systems used in industrial processes. They are the open loop system and the closed loop system. The systems are distinguished by the control actions.

3.3.1 Open-loop control

We speak of open-loop operation Figure 3.1 when the magnitude of the correction is independent of the measurements magnitude. The controller is in manual mode consists of leaving the user the choice of the value of the control signal applied to the actuator.

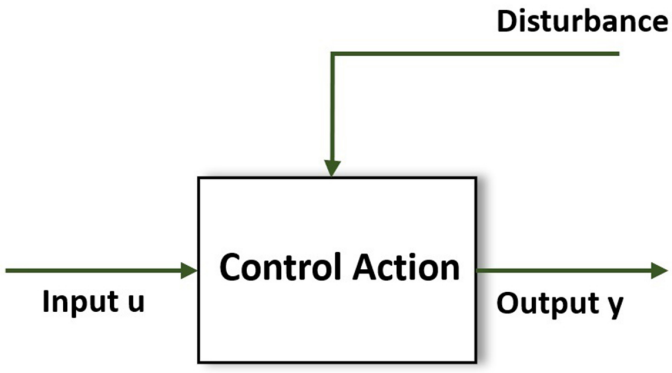

Figure 3.1: Open loop system.

3.3.2 Closed-loop control

This is the normal operation of a control. Suppose the magnitude of the measurement affects the magnitude of the correction (manipulated magnitude). The controller compares the measurement of the controlled variable and the setpoint and acts accordingly to approximate them Figure 3.2.

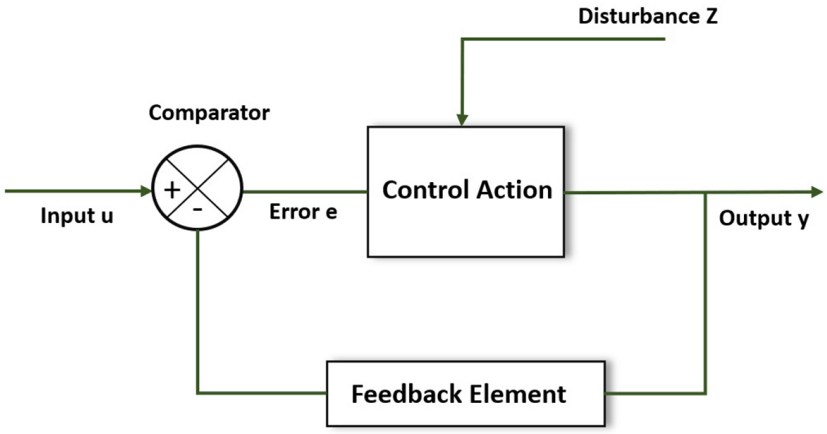

Figure 3.2: Closed loop system.

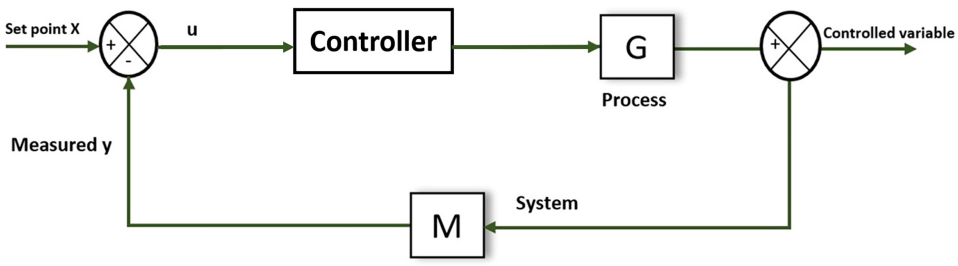

Figure 3.3: Control loop.

The Figure 3.3 summarizes the different functionalities in a control loop.

3.4 PID controller

3.4.1 Definition

PID controller it is a self-control system (closed loop), which seeks to reduce the error between the reference and the measurement [Silva et al., 2007].

e=set point – measurement

The purpose of control is to maintain at the desired value (reference quantity), a physical quantity (controlled quantity) such as temperature, relative humidity, pressure, etc.

Subject to disturbance by measuring its value. After comparison between the controlled variable and the reference variable, a control deviation results. Depending on this difference, the controller forms a control signal (control variable) which will vary the control power via an actuator (control device).

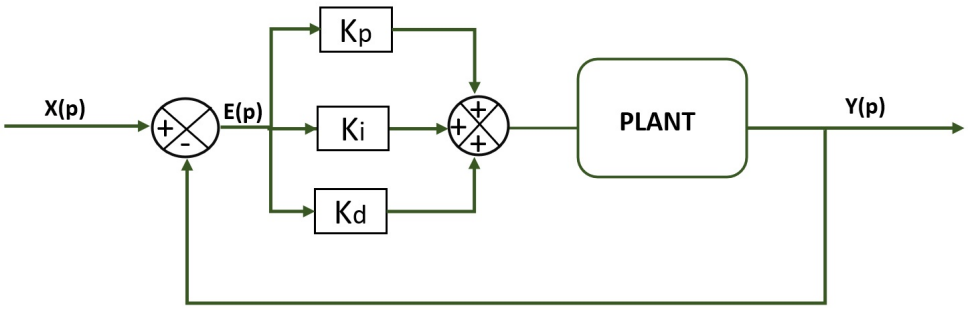

Figure 3.4: PID controller.

A PID controller is obtained by combining these three actions, and it essentially performs the following three functions:

- It provides a control signal taking into account the evolution of the output signal compared to the setpoint;

- It eliminates the static error thanks to the integrator term;
- It anticipates the variations of the output thanks to the derivative term.

3.4.2 Proportional action "P"

In the case of P controller, the error is virtually amplified by a certain constant gain which should be determined as a function of the system.

$$setpoint(t) = k_p e(t) \tag{3.1}$$

In Laplace gives

$$setpoint(p) = k_p e(p) \tag{3.2}$$

The idea is to increase the effect of the error on the system so that it reacts more quickly to changes of instructions. The greater the value of k_p, the greater the response. On the other hand, the stability of the system is deteriorates, and in the case of an excessive k_p, the system can even diverge.

3.4.3 Integrated action "I"

To the P controller, we can add the integration of the error. In this case, we obtain a PI control.

The error between the setpoint and the measurement is integrated with respect to time and multiplied by a constant which must also be determined according to the system.

$$setpoint(t) = k_p e(t) + k_i \int e(\tau) d\tau \tag{3.3}$$

In Laplace gives

$$setpoint(p) = k_p e(p) + k_i \frac{e(p)}{p} \tag{3.4}$$

Well, during a simple P controller, there remains a static error. When the system approaches its set point, the error is no longer large enough to move the motor forward. The integral term thus makes it possible to compensate

for the static error and therefore provides a more stable system in steady state. The higher k_i, the more the static error is corrected.

3.4.4 Derivative action "D"

To get PID controller, we need to add another term. This consists of deriving the error between the setpoint and the measurement with respect to time and also multiplying it by a constant.

$$setpoint(t) = k_p e(t) + k_i \int e(\tau)d\tau + k_d \frac{d}{dt} e(t) \tag{3.5}$$

In Laplace gives

$$setpoint(p) = k_p e(p) + k_i \frac{e(p)}{p} + k_d p e(p) \tag{3.6}$$

Well, the PI controller can lead to the setpoint being exceeded, which is not always very desirable (example of polarity inversion in the case of electric motors).

The term derivative helps to limit this. When the system approaches the setpoint, this term breaks the system by applying an action in the opposite direction and thus allows faster stabilization.

3.4.5 Type of controllers

Proportional action controller

The P controller, is a simple action and since it constructs a command $u(t)$ proportional to the error $e(t)$. This action is similar to a spring effect (return spring) [Akpakpavi, 2017].

- P controller transfer function:

$$u(p) = \frac{U(p)}{E(p)} = k_p \tag{3.7}$$

-P controller control law:

$$C(p) = k_p.e(t) \tag{3.8}$$

- Functional diagram of the P controller:

Figure 3.5: Functional diagram of the controller P.

Proportional-integral controllers

- PI controller transfer function [Mamizadeh et al., 2018]:

$$C(p) = k_p + \frac{1 + T_i p}{T_i p} \tag{3.9}$$

-Temporal equation:

$$u(t) = k_p.e(t) + \frac{1}{T_i} \int e(t)dt \tag{3.10}$$

-Functional diagram of PI controller:

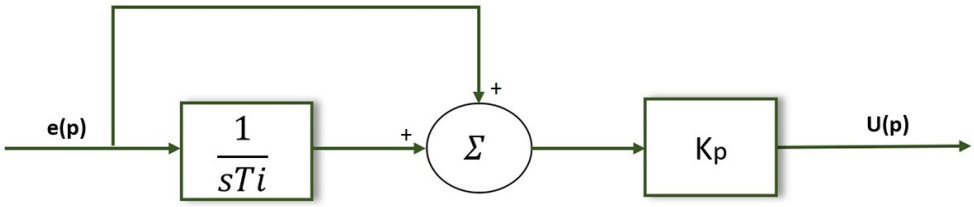

Figure 3.6: Functional diagram of PI controller.

Proportional-derivative action controller

-PD controller transfer function [Johnson and Moradi, 2005]:

$$C(p) = \frac{U(p)}{E(p)} = k_p(1 + T_d p) \tag{3.11}$$

-Temporal equation:

$$u(t) = k_p \left(e(t) + T_d . \frac{de(t)}{dt} \right) \tag{3.12}$$

-Functional diagram of the PD controller:

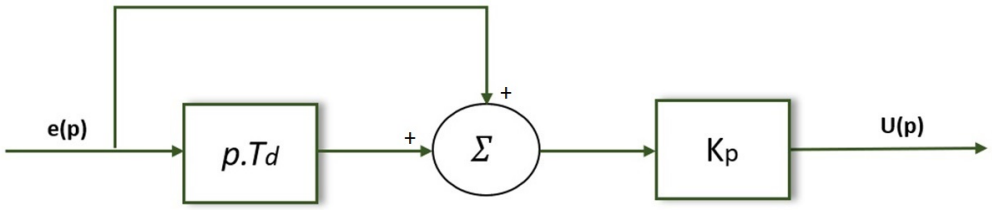

Figure 3.7: Functional diagram of the PD controller.

3.4.6 PID structures

The basic actions of a controller can be combined in several ways. We are talking about the algorithm structure of the controller. The values of the PID parameters do not give the same behavior of the process depending on whether the structure is parallel or mixed. This is why it is essential for the automation engineer to know the existing structures of the controller [Johnson and Moradi, 2005].

For the different structures we take:

- X(p): control set point
- Y(p): Adjusting variable

- e(p): Measurement / set point difference
- W(p): Controlled quantity (measurement)

Parallel structure

This structure is illustrated in Figure 3.8. Where, the output is given by:

$$Y(t) = k_p.(e(t) + \frac{1}{T_i}\int e(\tau)d\tau + T_d\frac{de(t)}{dt}) \tag{3.13}$$

By considering the initial conditions to be zero and by applying the Laplace transform to Equation (3.13), we obtain the transfer function of the PID controller with a parallel structure.

$$C(p) = \frac{Y(p)}{E(p)} = k_p + \frac{1}{T_i p} + T_d p \tag{3.14}$$

Where: $T_i = \frac{1}{k_i}$ and $T_d = kd$

With: T_i and T_d are the integration constant and the derivative constant, respectively.

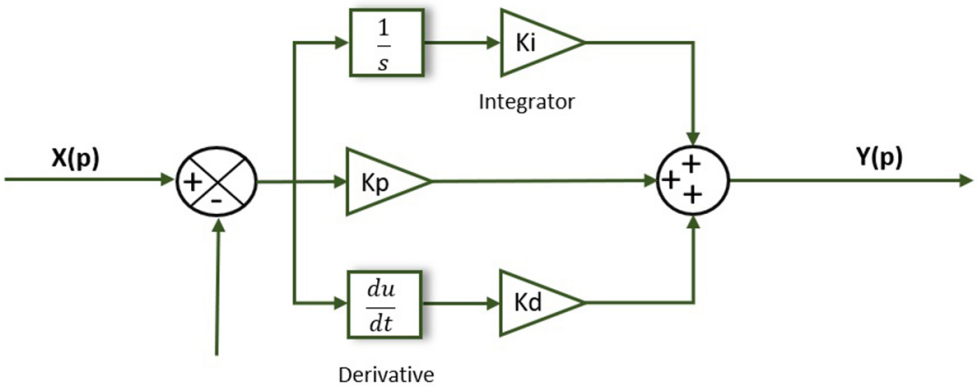

Figure 3.8: Parallel structure.

Series structure

This structure is illustrated by Figure 3.9.

In this case the output $Y(t)$ is given by:

$$Y(t) = \alpha k_p e(t) + \frac{k_p}{T_i}\int e(\tau)d\tau + T_d\frac{de(t)}{dt} \tag{3.15}$$

with: $\alpha = \frac{T_i+T_d}{T_i}$ theoretical coefficient of interaction between integral action and derivative action.

We consider the initial conditions to be zero, and by applying the Laplace transform to Equation (3.15), we obtain the transfer function of the PID controller with series structure.

$$C(p) = \frac{Y(p)}{E(p)} = k_p + (1 + \frac{1}{T_i p}) + (1 + T\alpha p) \tag{3.16}$$

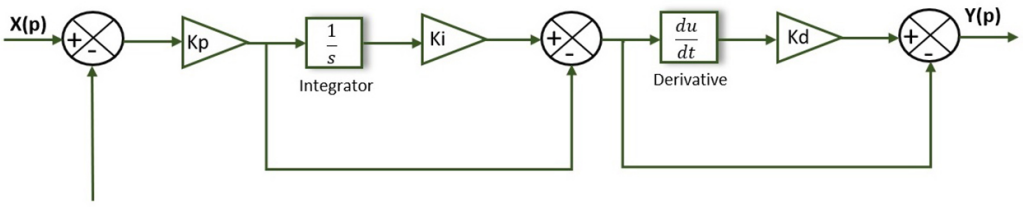

Figure 3.9: Series structure.

Mixed structure

It is the structure most currently used by manufacturers. The expression of the PID controller output is given by:

$$Y(t) = k_p e(t) + \frac{k_p}{T_i}\int e(\tau)d\tau + T_d\frac{de(t)}{dt} \tag{3.17}$$

By applying the Laplace transform, we obtain:

$$C(p) = \frac{Y(p)}{E(p)} = k_p + (1 + \frac{1}{T_i p} + T_d p) \tag{3.18}$$

This structure is represented by Figure 3.10.

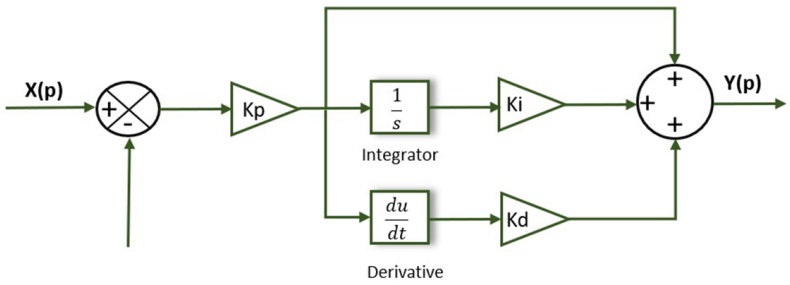

Figure 3.10: Mixed structure.

3.5 Performance criterion

Precision, damping, speed, make it possible to express the performance of a control. As a general rule, we seek to obtain a response time T_e. The figure of 15% can be used as the acceptable average value of the exceedance. It should be emphasized that if the adjustment of the control is carried out from a response due to changes in the set point, it is generally to variations in disturbing magnitude that the control is subject. The theory shows that if the stability, which is the indispensable condition, is assured in the first case, it will be in the second, but the pace of the transient will be different.

3.5.1 Dynamic precision performance criteria

In order to have good dynamic precision of a system with a step input, the transient regime must be characterized by a low overshoot and an optimal

response time. For this, the parameters of a controller are chosen so as to minimize the dynamic error $e(t) = y(t) - y_d(t)$ so we must minimize one of the following criteria [Gertler, 1998]:

The integral of absolute error (IAE)

The integral of absolute error is given by:

$$IAE = \int |e(t)|.dt \tag{3.19}$$

This criterion expresses the area generated by the difference between the setpoint and the actual value, and its role is to eliminate small errors [Gertler, 1998].

The integral of squared error (ISE)

The integral of squared error is given by:

$$ISE = \int e(t)^2.dt \tag{3.20}$$

The interest of this performance index is to correct the systems whose transient regime which lasts too long and takes much less account of overruns lower than one [Gertler, 1998].

The integral of time weighted absolute value of error (ITAE)

The integral of time weighted absolute value of error is given by:

$$ITAE = \int t.|e(t)|.dt \tag{3.21}$$

The introduction of the time parameter will correct systems with a very oscillatory response [Ho et al., 1996].

The integral of time weighted squared error (ITSE)

The integral of time weighted squared error is given by:

$$ITSE = \int t.e(t)^2.dt \tag{3.22}$$

This criterion places little emphasis on the initial errors and strongly penalizes the errors which occur towards the end of the transient response to a rung entry [Ho et al., 1996].

3.6 PID Controller parameters optimisation strategies

In industrial practice, PI and PID controllers, constructed by specialists in the field, are used directly. The problem of the corrector's synthesis is then no more than a problem of adjusting the proportional, integrator and derivative actions, that is to say, K_p, T_i, T_d. The adjustment of these parameters is a daily problem for the automation technician: for this, it is necessary to have methods that are simple to implement, fast and sufficiently precise [Astrom, 1988].

3.6.1 Optimization problem

An optimization problem is defined as the search for the minimum or the maximum (the optimum) of a given function.

The variables of this function are often forced to evolve in a certain part of the search space. We will therefore have an optimization problem under constraints. Mathematically, we try to minimize f on E, i.e., we look for $x^* \in E$ such that:

$$f(x^*) = minf(x) \tag{3.23}$$

3.6.2 Ziegler and Nichols method

Among all the methods proposed for calculating and the tuning of the P, PI and PID controllers parameters, the best documented is still that of ZN. It was developed by John G. Ziegler and Nathaniel B. Nichols in November 1942. It is based on observation of the response of the process and knowledge of the structure of the controller used. Three variants were proposed at that time, the first for closed loop tuning, the other for open loop, and the last for frequency tuning [Astrom, 1988].

Critical gain method

This method requires looping the system to a simple proportional controller whose gain increases until the system oscillates permanently Figure 3.11; we are thus at the limit of system stability. After having noted the critical gain K_{cr} and the oscillation period T_{cr} of the response, the parameters of the chosen controller can be calculated using Table. 3.1.

The values proposed by ZN have been tested in a large number of situations, and it should be noted that here too, they lead to a relatively short rise time with a high overshoot [Astrom, 1988].

Table 3.1: Adjustment of the P, PI and PID controller gains according to the first method of ZN [Astrom, 1988].

Type	**PID series**	**Parallel PID**	**Mixed PID**
K_p	$K_{cr} \cdot 0.3$	$K_{cr} \cdot 0.6$	$K_{cr} \cdot 0.6$
T_i	$\frac{T_{cr}}{4}$	$\frac{T_{cr}}{1.2 \cdot K_{cr}}$	$\frac{T_{cr}}{2}$
T_d	$\frac{T_{cr}}{4}$	$\frac{T_{cr} \cdot K_{cr}}{13.3}$	$\frac{T_{cr}}{8}$

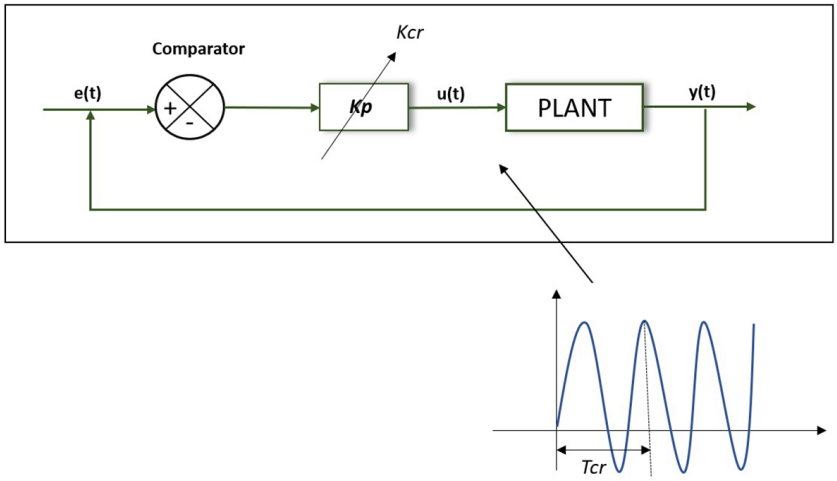

Figure 3.11: Critical gain method.

As this situation is not always satisfactory, we have to slightly correct the proposed coefficients. A possible modification is proposed by Table. 3.2. It is important to note that the parameters T_i and T_d proposed in the second method of ZN were set in a constant ratio equal to 4.

Table 3.2: ZN adjustment by the critical gain method [Astrom, 1988].

Type	K_p	T_i	T_d
P	$K_{cr} \cdot 0.5$	∞	0
PI	$K_{cr} \cdot 0.45$	$T_{cr} \cdot 0.38$	0
PID	$K_{cr} \cdot 0.6$	$T_{cr} \cdot 0.5$	$T_{cr} \cdot 0.125$

Step response method

Most of the methods of calculating control parameters consist of making calculations on the response curves of the open-loop process, following the application of a step Figure 3.12. In all cases. We consider the linear zone or the response curve presenting the maximum slope, we draw a straight

line " marrying " this linear zone and we are interested in the point of intersection of this straight line with the x-axis (time axis): we define the time T_u. We then define the time T_a, as is the time it takes for the control variable to vary by the same amplitude as the output of the controller, this at the maximum variation speed (the line previously plotted must therefore be answered). These two parameters then make it possible to define the controller adjustment parameters [Astrom, 1988].

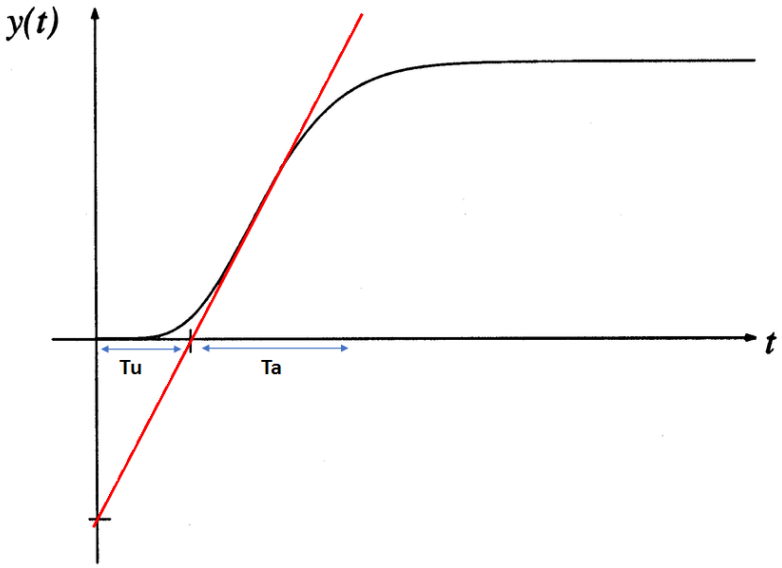

Figure 3.12: Step response method.

The coefficients of the chosen controller can then be calculated using Table. 3.3:

Table 3.3: Adjustment of the P, PI and PID controller gains according to the first method of ZN [Astrom, 1988].

Type	**PID series**	**Parallel PID**	**Mixed PID**
K_p	$\frac{T_a \cdot 0.6}{T_u}$	$\frac{T_a \cdot 1.2}{T_u}$	$\frac{T_a \cdot 1.2}{T_u}$
T_i	T_u	$\frac{T_u^2 \cdot 1.67}{T_a}$	$T_u \cdot 2$
T_d	T_a	$T_a \cdot 0.6$	$\frac{T_u}{2}$

Advantages and disadvantages of the ZN method

Advantages

-Easy to implement (physically and from a computational point of view)

-Tested on the system in production, corresponds to reality, can be done on the fly if the characteristics of the system are modified (wear, change of the environment).

The disadvantages

- The system can become unstable or go into dangerous states (chemistry)

- Can take a long time if the system reacts very slowly (days, weeks in chemistry)

3.7 Particle swarm optimization method

PSO is an evolutionary algorithm that uses a population of candidate solutions to develop an optimal solution to the problem. This algorithm was proposed by Russel Eberhart (electrical engineer) and James Kennedy (socio-psychologist) in 1995. It was originally inspired by the living world, more precisely by the social behavior of animals evolving in swarms, such as schools of fish and grouped flights of birds. The particle swarm is a population of simple agents called particles. Each particle is considered as a solution of the problem, where it has a position (the solution vector) and a speed. In addition, each particle has a memory allowing it to remember its best performance (in position and in value) and the best performance achieved by the "neighboring" particles (informants): each particle has indeed a group of d informants, historically called her neighborhood [Kennedy and Eberhart, 1995].

3.7.1 PSO operating principle

In this algorithm, candidate solutions of a population, called particles, coexist and evolve simultaneously based on knowledge sharing with neighboring particles. As it flew through search space, each particle generates a solution using its velocity vector. Each particle changes its speed to find a better solution (position) by applying its own flight experience (i.e., the memory having the best position found in previous flights) and the experience of neighboring particles (i.e., d best solution found from the population)

The movement of a particle is influenced by three components [Bai, 2010]:

-A component of inertia: the particle tends to follow its current direction of movement.

-A cognitive component: the particle tends to trust its own experience and, thus, to go to the best site through which it has ever been.

-A social component: the particle tends to rely on the experience of its congeners and, thus, to go to the best site already reached collectively by the swarm.

In a D-dimensional search space, the particle i of the swarm is modeled by its position vector $\vec{x}_{ij} = (x_{i1}x_{i2}.....x_{iD})^T$ and by its velocity vector $\vec{v}_{ij} = (v_{i1}v_{i2}.....v_{iD})^T$.

The quality of its position is determined by the value of the objective function at that point. This particle remembers the best position it has ever passed through, which is noted by $\vec{p}_{ij} = (p_{i1}p_{i2}.....p_{iD})^T$, and the position reached by its neighboring particles which is denoted by:

$$\vec{g}_{ij} = (g_{i1}g_{i2}.....g_{iD})^T \tag{3.24}$$

The principle of the particle swarm method is summarized in Figure 3.13.

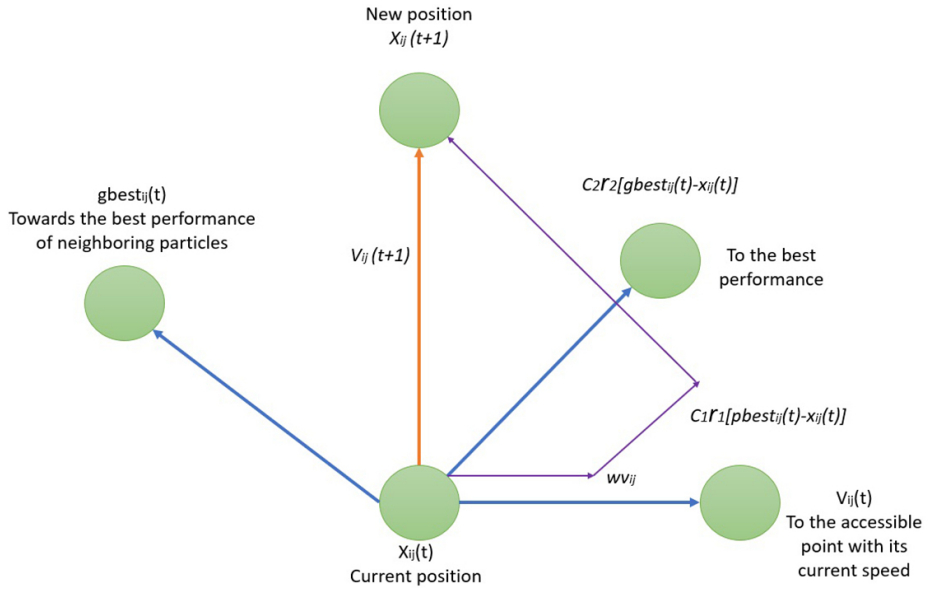

Figure 3.13: Displacement of a particle.

The speed vector is calculated from the following Equation (3.25) [Bai, 2010]:

$$v_{ij}(k) = wv_{ij}(k-1) + c_1 r_1(p_{ij}(k-1) - x_{ij}(k-1)) + c_2 r_2(g_i(k-1) - x_{ij}(k-1)) \quad (3.25)$$

The position at the iteration of particle i is then defined by Equation (3.26):

$$x_{ij}(k) = x_{ij}(k-1) + v_{ij}(k) \quad (3.26)$$

$i = 1, 2, 3....N_p \; j = 1, 2, 3....N_d \; k = 1, 2, 3....N_{k_{max}}$

With:

N_p is the number of particles in the swarm.

N_d is the number of variables in the problem (ie dimension of a particle).

$N_{k_{max}}$is the maximum number of iterations.

$v_{ij}(k)$ is the speed of the j^{th} component of the i^{th} particle of the swarm, at the k^{th} iteration.

p_{ij} is the j^{th} component of the best position occupied by the i^{th} particle of the swarm recorded in the previous iterations (local best).

g_i is the j^{th} component of the best position occupied by the i^{th} global particle of the swarm (global best).

$x_{ij}(k)$ the j^{th} coordinate of the current position of particle i, at the k^{th} iteration.

w is usually a constant called the coefficient of inertia, c_1 and c_2 are two constants called acceleration coefficients, r_1 and r_2 are two random numbers drawn uniformly in $[0, 1]$ at each iteration and for each dimension.

$wv_{ij}(k-1)$ correspond to the physical component of displacement. The parameter controls the influence of the direction of travel on the future displacement. It should be noted that, in certain applications, the parameter w can be variable.

$c_1r_1(p_{ij}(k-1) - x_{ij}(k-1))$ correspond to the cognitive component of the displacement where $c_1$controls the cognitive behavior of the particle.

$c_2r_2(g_i(k-1) - x_{ij}(k-1))$ corresponds to the social component of displacement, where control the social aptitude of the particle.

The appropriate value ranges for c_1 and c_2 are, from 1 to 2, but 2 is most appropriate in many cases [Eberhart and Shi, 2000].

The coefficient of inertia can vary depending on:

$$w = w_{max}\left(\frac{w_{max} - w_{min}}{k_{max}}\right) \cdot k \tag{3.27}$$

Where k_{max}, k are respectively the maximum number of iterations and the number of current iterations. w_{min} and w_{max} are respectively the minimum and maximum inertia coefficients.

The coefficient of inertia w plays an important role in the search procedure. It guarantees a balance between local search and global search, a good choice of this function increases the efficiency of the method to have a global solution. Experience has shown that linearly decreasing the value from 0.9 to 0.4 during the search procedure gives better results [Eberhart and Shi, 2000].

3.7.2 Confinement mechanism

It sometimes happens that taking into account the current position and the current speed of a particle, the latter tends to leave the search space during its movement. When this is the case, the algorithm uses a confinement mechanism, called interval confinement, in order to manage the displacement of the particle and this so that it brings it to a new point belonging to him also to the search space. In general, this mechanism consists of bringing the particle back to the closest admissible point [Nouaouria et al., 2014].

$$\begin{cases} if \quad x_{ij} > x_{jmax}, \quad then \quad x_{ij} = x_{jmax} \\ \\ if \quad x_{ij} < x_{jmin}, \quad then \quad x_{ij} = x_{jmin} \\ \\ \qquad v_{ij} = 0 \end{cases} \tag{3.28}$$

To explain the principle of the PSO algorithm applied to solve an optimization problem, consider the minimization problem [Kim et al., 2008].

$$\begin{cases} minf(x) \\ x \in D \end{cases} \tag{3.29}$$

The associated fitness function is:

$$fitness(x_j) = f(x_j) \tag{3.30}$$

The PSO algorithm takes place in the following steps [Qi et al., 2009]:

Step 1: initialize a population of particles and velocities, uniformly distributed in the search space D, and fix the stopping criterion.

Step 2: evaluate the objective function, for each particle.

Step 3: update the best position P_{best} for each particle and the best global position g_{best} population.

Step 4: Update position and velocity using the chair.

Step 5: if a particle, moved by the algorithm towards the limit or outside the search space, the particle confinement mechanism expressed by Equation (3.28) intervenes and brings the particle back to l inside the search space.

Step 6: check the stopping criterion. If the stop criterion is not satisfied, go to step 2 otherwise, the program ends, and the optimal solution is produced.

The flowchart which summarizes the steps for the basic PSO algorithm is shown in Figure 3.14

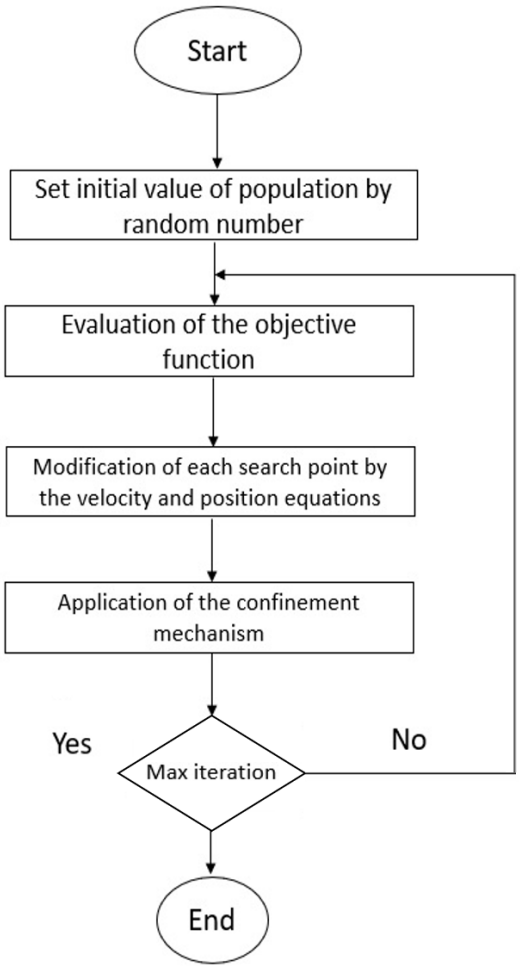

Figure 3.14: PSO algorithm steps.

3.7.3 Advantages and Disadvantages of PSO

The PSO algorithm has a definite advantage over classical methods in that it allows a random exploration of the solution space. In addition, its simplicity to implement and its execution leads to obtaining very good results, quickly and easily with few parameters to adjust.

Although the PSO finds good solutions in a much shorter time than other evolutionary algorithms, improving the quality of solutions cannot be

guaranteed by increasing the number of iterations.

The PSO algorithm has two main drawbacks:

The first drawback is that the swarm can prematurely converge.

The second drawback is that stochastic approaches have a dependency problem; any change in one of their parameters can have an effect on the operation of the algorithm as well as on the solution obtained [Nekoui et al., 2010].

3.8 Conclusion

PI and PID controls are some of the most widely used controls today for several reasons.
First, they are straightforward to set up, and they are effective for most real systems. In addition, the calculation of his coefficients leaves the choice between several methods which we have presented in order to decrease the difficulty of implementation.
On the other hand, an experimental and simulation method that is very easy to set up makes it possible to quickly obtain correct coefficients for systems that do not require very great precision in control.
Thus, the implementation of a controllers PI and PID can be at the same time fast and effective and allow an optimization of the coefficients for the most advanced systems.

Chapter 4

SLIDING MODE CONTROL STRATEGY

Mathematics is the queen of the science.

Carl Friedrich Gauss

4.1 Introduction

In the control of non-linear systems or having non-constant parameters, conventional control laws may be insufficient because they are not robust, especially when the requirements on accuracy and other dynamic characteristics of the systems are strict. One must appeal to control laws insensitive to variations in parameters, disturbances and non-linearity. To this end, several tools are proposed in the literature, including variable structure control (VSC) and fuzzy logic. The SMC is part of the family of VSC control, which means controls switching between several different control laws. The importance of sliding mode controllers lies in: high precision, fast dynamic response, stability, simplicity of design and implementation, and robustness with respect to variation of internal or external parameters [Slotine et al., 1991, Fridman and Levant, 2002]. The

principle of control by sliding modes is very simple, which represent to force the trajectories of the system to reach a given surface (sliding surface), and then to stay there. However, the control by sliding mode control in practice induces high-frequency switching known as chattering. This final is a harmful phenomenon that leads to low control accuracy and heat loss in the energy circuits. There are various methods to reduce this phenomenon, one of which consists of replacing the sign function with a continuous approximation in the vicinity of the sliding surface (saturation function or sigmoid function). Another method consists of using the high order sliding modes [Bartolini et al., 2000, Fridman and Levant, 2002, Bühler, 1986, Levant, 1993], the principle of which is to reject the discontinuities at the level of the high derivatives of the input of the system.

This chapter is divided into two parts: In the first part, we will present the basic concepts of the 1 st order sliding mode as well as the major problem of this control which is represented in the chattering effect. An overview for the HO-SMC is presented in the second part, which is considered as an ideal solution for the chattering effect and ensures a better convergence.

4.2 System with variable structure

A system with a variable structure is the system whose structure changes during operation. It is characterized by choice of a function and switching logic. This choice allows the system to switch from one structure to another at any time. In sliding mode control of VSCs, the state path is brought to a surface, then using the commutation law, it is forced to remain in the vicinity of this sliding surface. Controllers with variable structures appeared in Soviet literature [Gao and Hung, 1993, Utkin, 1977].

In VSCs, we can find two different basic configurations. The first changes the structure by switching between two different state returns Figure 4.1. The

second configuration, called: "configuration by switching at the level of the controller", is the simplest. It modifies the structure of the system by simple switching of switches Figure 4.2, which is the case with all static converters [Liutanakul, 2007].

For the first configuration, the control is given by:

$$u = \begin{cases} -k_1(x), if & s(x) > 0 \\ -k_2(x), if & s(x) < 0 \end{cases} \tag{4.1}$$

In sliding mode, the system evolves on the sliding surface, consequently $s(x) = 0$.

The second configuration requires a controller which has a two position action with rapid switching from one position to another. Switching between these two values is imposed by the switching law according to:

$$u = \begin{cases} u^+, if & s(x) > 0 \\ u^-, if & s(x) < 0 \end{cases} \tag{4.2}$$

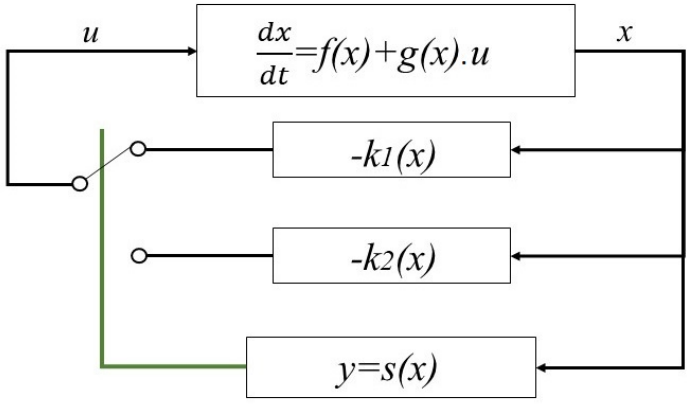

Figure 4.1: Configuration by switching on the status feedback.

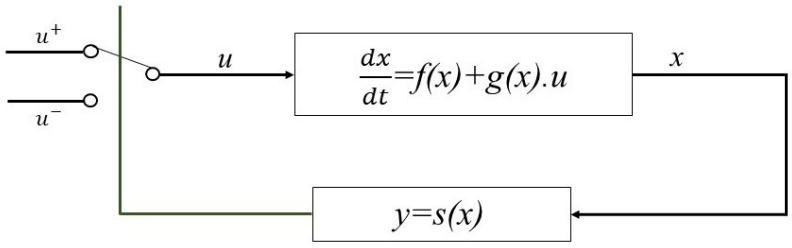

Figure 4.2: Configuration by switching on the control unit.

4.3 Sliding mode control

4.3.1 Principle

The sliding mode control is a robust control based on the concept of changing the structure of the controller with the state of the system in order to obtain the desired response [Utkin, 1977]. The sliding mode controller is based on the assumption of a zero hysteresis on the sliding surface $s(x,t) = 0$ and therefore on a variable and theoretically infinite switching frequency. It is clear that from a practical point of view, it is not possible to verify this hypothesis. Due to the technological limitations of using high switching frequencies, it is preferable to limit this frequency.

The idea is to divide the state space by a decision boundary called: "sliding surface". This surface delimits two subspaces corresponding to two possible states of the control device Figure 4.3. Stabilization on the sliding surface is obtained by switching over each time the decision boundary is crossed.

This control principle, is therefore essentially based on the use of a discontinuous control in order to maintain the evolution of the system on a carefully chosen sliding surface. The synthesis must therefore aim to make the sliding surface attractive (condition of attractiveness) from any point of the state space. Once the surface is reached, it is necessary to ensure the

sliding along this surface (sliding condition) and the stability of the system (stability condition). In other words, it is necessary to find the condition for which the dynamics of the system slide on the surface towards the desired point of equilibrium Figure 4.3. On the surface, the dynamics of the system are independent of that of the initial process, which implies that this type of control enters in the field of robust controls. These notions of stability are demonstrated by taking into account the principle of stability according to the criterion of Lyapunov theorem (4.32).

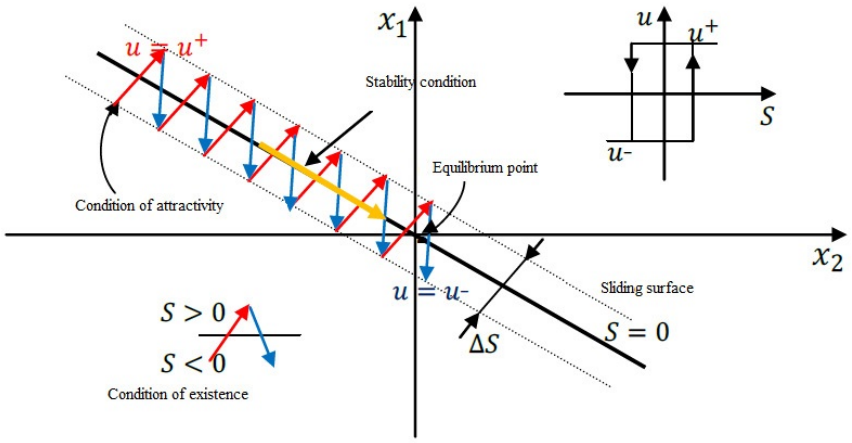

Figure 4.3: Principle of sliding mode control.

For each switch, the control is performed by a hysteresis comparator. The direction of the hysteresis should be chosen so that the change of state brings the trajectory back within the range. Thus, we may have to choose:

$$u = \begin{cases} 1, if & S(x) > 0 \\ 0, if & S(x) < 0 \end{cases} \tag{4.3}$$

Let $V(x)$ be a function differentiable from R^N into R^N, called the Lyapunov function, which satisfies the following conditions [Hijazi, 2010]:

$$\begin{cases} V(0) = 0 \\ V(x) > 0 \forall x \neq 0 \\ V^*(x) \leq 0 \forall x \neq 0 \end{cases} \tag{4.4}$$

If these three conditions are satisfied, $x = 0$ is a point of stable equilibrium. If the last condition becomes $V^*(x) \leq 0$ for $x \neq 0$, the point $x = 0$ is asymptotically stable.

In the case of the control by sliding mode, this function of Lyapunov is deduced using a pseudo-output which is the surface of sliding $s(x,t) = 0$.

4.3.2 Sliding mode control objective

The objective of sliding mode control can be summed up in two essential points:

- Synthesize a surface $s(x,t)$ such that all the trajectories of the system obey a desired behavior of pursuit, regulation and stability;
- Determine a control (commutation) law $u(x,t)$ which is capable of attracting all state trajectories towards the sliding surface and maintaining them on this surface.

4.3.3 Choice of sliding surface

The surface $s(x)$ presents the desired dynamic behavior of the system. Slotine [Slotine, 1984] proposes a form of the general equation to determine the sliding surface which ensures the convergence of a variable to its desired value:

$$s(x) = \left(\frac{\partial}{\partial t} + \lambda_x\right)^{r-1} e(x) \tag{4.5}$$

Where:

$e(x)$: Deviation of the variable to be adjusted, $e(x) = x_{ref} - x$
λ_x: Positive constant that interprets the bandwidth of the desired control.
r: Relative degree, equal to the number of times it takes to derive the output to make the control appear.
$s(x) = 0$: is a linear differential equation whose unique solution is $e(x) = 0$.

4.3.4 The sliding surface existence condition

The existence condition of the sliding surface $s(x,t) = 0$ results in [Utkin, 2013, Komurcugil, 2012]:

$$\lim_{s \to 0} s \cdot s^* < 0 \tag{4.6}$$

These conditions are deduced from Theorem (4.32) by applying the Lyapunov stability criterion in a neighborhood of the sliding surface and by taking $V(x) = \frac{s^2}{2}$ as candidate function of Lyapunov. In this case, the derivative of the function of Lyapunov V^* is equal to $s \cdot s^*$.

The Lyapunov conditions stated in Theorem (4.32) are verified if s and s^* are of opposite signs. Note that these latter conditions become sufficient conditions to ensure the surface's attractiveness if they are valid over the entire state space and not only in a region close to the sliding surface.

4.3.5 Control output

The zig-zag curve between u^+ and u^- shown in Figure 4.3 is the actual (practical) state path of the system. It surrounds the line $s = 0$, which is the ideal (theoretical) or reference state trajectory. It is possible to subdivide the displacement of the real trajectory into two components; a high-frequency component and a low frequency component. The high-frequency component

is a discontinuous path that alternates between u^+ and u^-, while the low-frequency component forms a continuous path that moves along the sliding surface. Ignoring the often filtered fast switching component, the state path will then be determined by the slow switching component. This is called the equivalent control, which can be interpreted as the average value taken by the control quantity during rapid switching between u^+ and u^- as shown schematically in Figure 4.4.

The equivalent control makes the switching surface time invariant $s = 0$ [Trigeassou et al., 2003].

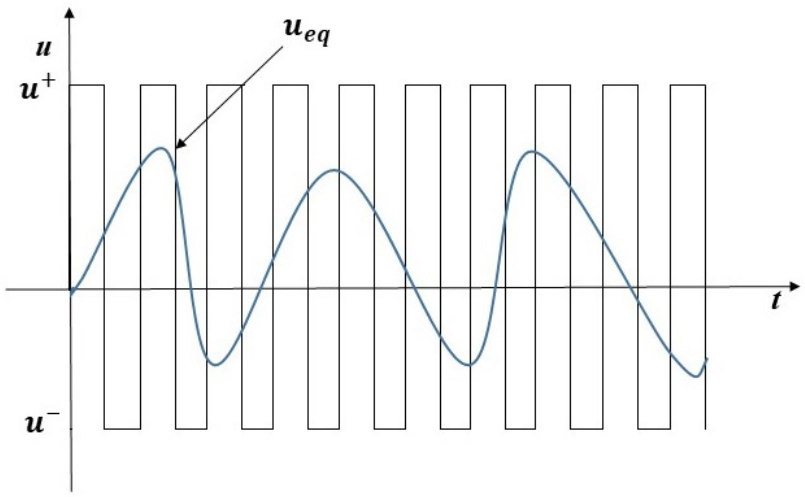

Figure 4.4: Equivalent control as average switching value between u^+ and u^-.

Consider as an example the system controlled by the following differential equation:

$$\dot{x} = f(x,t) + g(x,t)u \tag{4.7}$$

Let us assume that the slid regime exists on the switching surface $s(x,t) = 0$, its derivative is given by:

$$s^* = \frac{ds(x,t)}{dt} = \frac{1}{dt}\left(\frac{\partial s}{\partial x}dx + \frac{\partial s}{\partial t}dt\right) = \frac{\partial s}{\partial x}x^* + \frac{\partial s}{\partial t} \tag{4.8}$$

Let ∇s be the gradient of s, then:

$$s^* = \nabla s.x^* + \frac{\partial s}{\partial t} = \nabla s.f(x,t) + \nabla s.g(x,t)u + \frac{\partial s}{\partial t} \tag{4.9}$$

In sliding mode and in the steady-state, the surface's derivative is zero (because its antiderivative is equal to zero). This condition makes it possible to determine the equivalent control to maintain the state trajectory on this surface. We must therefore solve:

$$\nabla s.f(x,t) + \nabla s.g(x,t)u_{eq} + \frac{\partial s}{\partial t} = 0 \tag{4.10}$$

Thus, we get:

$$u_{eq} = -\left[\nabla s.g(x,t)\right]^{-1} \cdot \left[\nabla s.f(x,t) + \frac{\partial s}{\partial t}\right] \tag{4.11}$$

It is then possible to express the dynamics of the system on the sliding surface by:

$$x^* = f(x,t) - g(x,t) \cdot \left[\nabla s.g(x,t)t\right]^{-1} \cdot \left[\nabla s.f(x,t) + \frac{\partial}{\partial t}s(x)\right] \tag{4.12}$$

The control by sliding mode consists of two terms, a discontinuous control as a function of the sign of the sliding surface u_n and a so-called equivalent control u_{eq} characterizing the dynamics of the system on the sliding surface.

$$u = u_n + u_{eq} \tag{4.13}$$

u_n corresponds to the nonlinear component. It is determined to guarantee the attractiveness of the variable to be controlled towards the sliding surface and to satisfy the convergence condition.

$$s \cdot s^* < 0 \tag{4.14}$$

From (4.7), (4.8), and (4.13) we can write:

$$s^* = \frac{\partial s}{\partial x}(f(x,t) + g(x,t).u_{eq}) + \frac{\partial s}{\partial x}(g(x,t).u_n) + \frac{\partial s}{\partial t} \tag{4.15}$$

By using the sliding mode condition, the expression (4.15) becomes:

$$s^* = \frac{\partial s}{\partial x}(g(x,t).u_n) \tag{4.16}$$

The problem comes down to finding u_n such that:

$$s \cdot s^* = s(x).\frac{\partial s}{\partial x}(g(x,t).u_n) < 0 \tag{4.17}$$

The simplest solution verifying this condition is given by the sign function "sign" illustrated in Figure 4.5.

$$u_n = k.sign(s(x)) \tag{4.18}$$

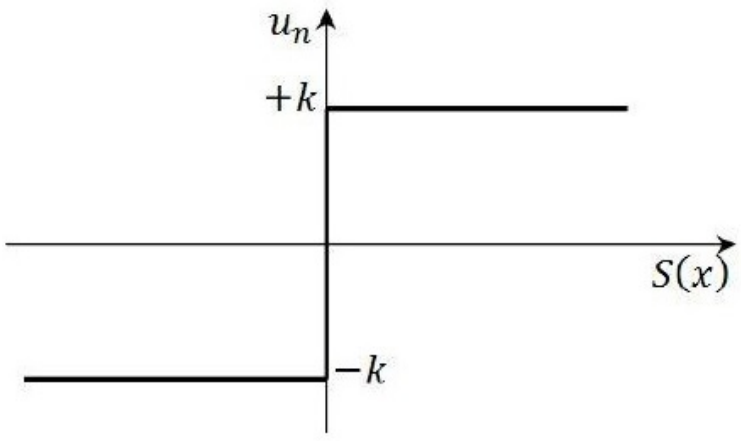

Figure 4.5: Representation of the sign function.

By replacing the expression (4.18) in (4.17), we obtain:

$$s \cdot s^* = s(x).\frac{\partial s}{\partial x}(g(x,t)k.sign(s(x))) < 0 \tag{4.19}$$

Where the factor $\frac{\partial S}{\partial x}g(x,t)$ is always negative for the class of system we are considering.

The gain k is chosen to be positive to satisfy condition (4.18). The choice of this gain is very influential because if it is very small, the response time will be very long and, if it is chosen very large, we will have strong oscillations at the level of the controller. These oscillations can excite neglected dynamics (chattering phenomenon) or even deteriorate the controller [Utkin, 2013].

4.3.6 Chattering effect

An ideal slip speed requires control that can switch at an infinite frequency. Thus, during the sliding regime, the discontinuities applied to the control can lead to an unwanted osculation or the phenomenon of chattering. This is characterized by strong oscillations of the trajectories of the system around the sliding surface Figure 4.6. The main reasons for this phenomenon are the limitations of the actuators or the switching delays at the control level. These switchings degrade the precision of the control and can be detrimental to the controller by causing premature deterioration of mechanical systems and a rise in temperature in electrical systems (significant loss of energy).

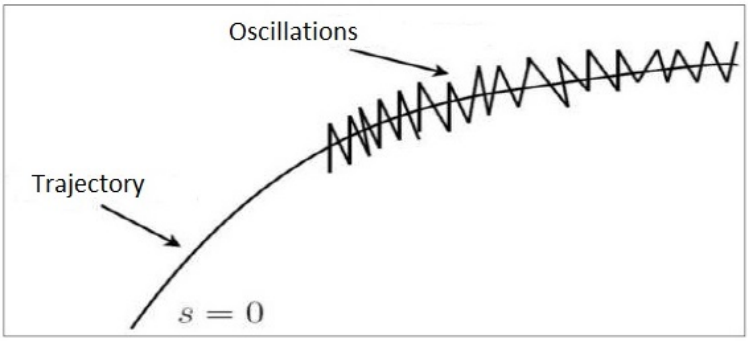

Figure 4.6: Chattering phenomenon.

4.3.7 Chattering reduction solutions

In order to reduce or eliminate this phenomenon, many solutions have been proposed, such as the boundary layer solution, fuzzy sliding mode, high order sliding mode, approach law, etc ...

Boundary layer solution

This solution, also known under the name of "boundary layer solution", consists of replacing the sign function by a continuous approximation, of the large gain type, only in a neighborhood of the surface. Among the functions used, we will cite the saturation function:

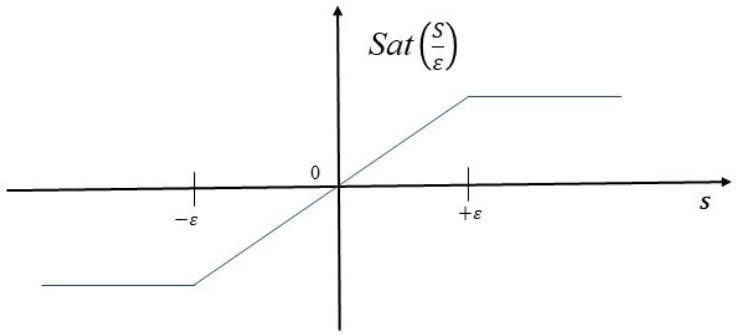

Figure 4.7: Saturation function [Asad et al., 2017]

$$u = \begin{cases} \frac{s}{\epsilon}, if & |\frac{s}{\epsilon}| \leq 1 \\ sign(s), if & |\frac{s}{\epsilon}| > 1 \end{cases} \tag{4.20}$$

ϵ: Width of the threshold of the saturation function.

Other functions are exist such as functions, $tanh\frac{s}{\epsilon}$, $2\pi \arctan\frac{s}{\epsilon}$ ext....

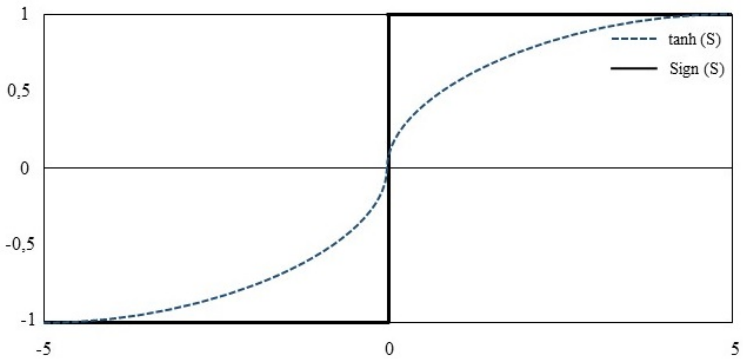

Figure 4.8: Hyperbolic tangent function [Fang et al., 2019]

This method is parameterized by a positive constant ϵ adjusted to have a good compromise between reduction of chattering and conservation of robustness. In the methods presented here, the smaller ϵ is, the more approximation tends towards the sign function, and therefore better the robustness, to the detriment of the reduction in chattering.

HO-SMC techniques

HO-SMC were introduced to overcome the problem of chattering while retaining the finite-time convergence and robustness properties of classical sliding mode control [Slotine et al., 1991, Bühler, 1986]. In this approach, the term discontinuous no longer appears directly in the expression of the synthesized control but in one of its high derivatives, which has the merit of reducing chattering [Isidori et al., 1995].

4.4 HO-SMC control

The HO-SMC, which is a modified version of the first-order sliding mode that is presented in the precedent section. The theory of control by high order sliding modes [Bühler, 1986] is an alternative to the problem of classical sliding modes.

In this approach, the term discontinuous no longer appears directly in the synthesized control but in one of its high derivatives, which has the merit of reducing chattering.

The high order sliding modes (HO-SMCs) were introduced to overcome the problem of chattering while keeping the properties of finite time convergence and robustness of the controls by classical sliding modes they also make it possible to improve the asymptotic precision. Most of the controls using this concept are based on the notion of homogeneity, with a particular set of coefficients (weights).

Consider a nonlinear system described by:

$$\dot{x} = f(x,t) + g(x,t).u \tag{4.21}$$

The objective is to establish a sliding regime of order two with respect to s, by forcing the state trajectories of the system to evolve at the end of a finite time on the set s_2 and not to leave it afterwards:

$$s_2 = \{x : s = \dot{s} = 0\} \tag{4.22}$$

This is achieved by a control acting on the second derivative of the slip variable which in general, can be written in the form:

$$\ddot{s} = \phi(x,t) + \psi(x,t).\nu \tag{4.23}$$

In order to carry out sliding mode algorithms of order two, it is necessary to check the following working hypothesis to validate the reachability of the sliding surface, and the boundness of the variable $\ddot{s}$ [Bühler, 1986]:

- The uncertain functions $\phi(x,t)$ and (x,t) are bounded.
- There are four positive constants s_0, C_0, K_m and K_M such that, in a neighborhood $\mid s(x,t) \mid < s_0$, the following inequalities which verified:

$$\mid \phi(x,t) \mid < C_0, 0 < K_m < \mid \psi(x,t) \mid < K_M \tag{4.24}$$

The assumptions stated above explain that the second derivative of the switching function is uniformly bounded in a certain domain E for the considered input.

By respecting the conditions already defined, we can write that any solution relating to Equation (4.27) satisfies the following differential inclusion [Bühler, 1986]:

$$\ddot{S} \in [-C_0, C_0] + [K_m, K_M] .\nu \tag{4.25}$$

There are several types of second-order sliding mode which will be described in the next sections.

4.4.1 Twisting algorithm (TWG)

In addition to switching the sign of the control, its amplitude is switched between two values depending on the quadrant in which the state of the system is located. The path of the system in the phase plane revolves around the origin, approaching it like a spiral [Levant, 1993].
Its expression for a system of relative degree of 2 is:

$$u = -r_1.sign(s) - r_2.sign(\dot{s}) \quad with \quad r_2 > r_1 \tag{4.26}$$

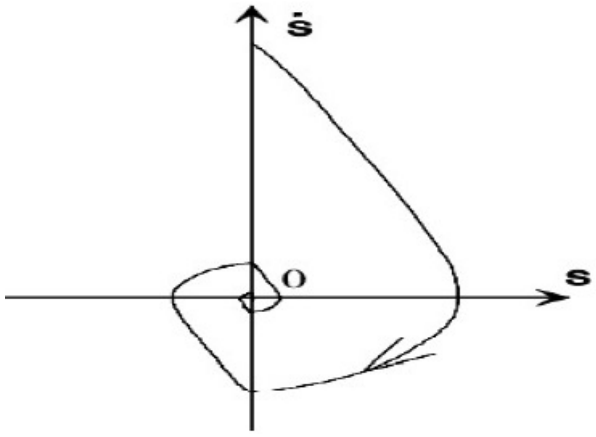

Figure 4.9: Convergence of the TWG algorithm [Guesmi et al., 2018]

Under the conditions described by the inequalities Equation (4.25), the trajectory of the differential system Equation (4.22) converges at the equilibrium point $s = 0$ in a finite time under the following conditions:

$$\begin{cases} (r_1 + r_2).K_m - C_0 > (r_1 - r_2).K_M + C_0 \\ \\ (r_1 + r_2).K_m > C_0 \end{cases} \tag{4.27}$$

The homogeneity of this control law is obvious because its expression does not depend on the value of s or $\dot{s}$, but only on their sign, which does not vary by multiplying them by $K > 0$.

4.4.2 Super-twisting algorithm (STWG)

This algorithm was developed for the control of systems with a relative degree equal to 1 with respect to the sliding surface. This control law was proposed by Emelyanov in 1990. It was studied by Levant in [Levant, 1993]. Super-twisting does not use information about $\dot{s}$ this can be seen as an advantage. It is composed of two parts, a discontinuous part u_1 and a continuous part u_2.

$$u = u_1(t) + u_2(t) \tag{4.28}$$

$$\dot{u_1} = \begin{cases} -u, if & \mid u \mid > U_M \\ -\alpha.sign(s), if & Not \end{cases} \tag{4.29}$$

$$u_2 = \begin{cases} -\lambda \mid S_0 \mid^{\rho} .sign(s), if & \mid u \mid > S_0 \\ -\lambda \mid s \mid^{\rho} .sign(s), if & Not \end{cases} \tag{4.30}$$

With α, λ, ρ satisfying the following inequalities:

$$\begin{array}{l} \alpha > \frac{C_0}{K_m}, 0 < \rho < 0.5 \\ \\ And, \lambda \geq \frac{4C0.KM(\alpha+C0)}{Km^2.Km^2(\alpha-C0)} \end{array} . \tag{4.31}$$

In the following, we will fix $\rho = 0.5$.

This control breaks down into an algebraic term (not dynamic) and an integral term. We can therefore consider this algorithm as a nonlinear generalization of a PI.

If $s_0 = \infty$ we can simplify the algorithm:

$$\begin{array}{l} u = -\lambda \mid S \mid^{\rho} .sign(s) + u_1 \\ \dot{u}_1 = -\alpha.sign(s) \end{array} . \tag{4.32}$$

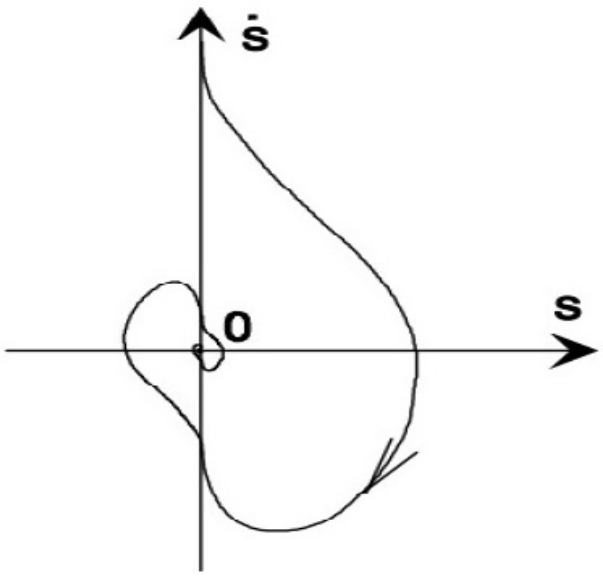

Figure 4.10: Convergence of the STWG algorithm [Derbeli et al., 2019b]

The trajectory of the algorithm in the phase plane $(s, \dot{s})$ is given in Figure 4.10, and it is shown that the consecutive intersections of the

latter with the axes of the plane $(s, \dot{s})$ evolve while approaching the origin which is reached in finite time. By a particular choice of the model and of the sliding surface, the super twisting sliding mode control algorithm [Levant, 2001, Bühler, 1986], can be formulated as an observation algorithm for the estimation of the derivative of a signal measured.

4.4.3 Prescribed convergence law algorithm (PCL)

This choice is justified by the simplicity of implementation and by a need for a relatively small amount of information on the state of the system.
The general formulation of this controller is given by the following expression [Fridman and Levant, 2002]:

$$u = -\alpha.sign(\dot{s} - g_c(s)) \tag{4.33}$$

α is a positive constant and g_c a continuous function defined by:

$$g_c(s) = -\lambda \mid s \mid^{\rho} .sign(s), \alpha, \lambda > 0, 0.5 \leq \rho < 1 \quad . \tag{4.34}$$

A sufficient condition for a convergence in finite time towards the sliding surface is defined by the following relation:

$$\alpha.Km - C0 > \frac{\lambda^2}{2} \tag{4.35}$$

Where $C0$ and Km are positive constants presented in Equation (4.24)

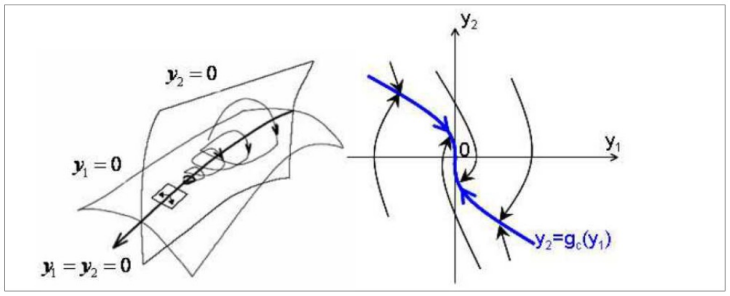

Figure 4.11: Convergence of the trajectories of the system towards the origin of the phase plane (left) and the continuous function $g_c(s)$ (right) [Fridman and Levant, 2002].

Important values of λ. Equation (4.34) allowing to accelerate the convergence towards the sliding surface. Only the knowledge of the function of slip s, as well as its derivative $\dot{s}$ are necessary for the computation of the control law. Knowing other system parameters explicitly is not necessary, which not only reduces the computational time required by the controller but also simplifies its tuning by adjusting only the three parameters ρ, λ and α.

4.4.4 Levant algorithm

The control law is based on the use of different sliding surfaces, each one which converges the system in finite time towards the next surface. Once the new surface is reached, the system can leave the previous surface. The state of the system passes from one surface to another alternately until it reaches the origin, in finite time [Levant, 2001].
We set:

$$\begin{cases} N_{1,n} = \mid S \mid^{(n-1/n)} \\ N_{i,n} = \left(\mid s \mid^{(m/n)} + (\mid \dot{s} \mid^{(m/(n-1))} .. \mid s^{(i-1)} \mid^{(m/(n-i+1))} \right)^{(n-i/m)}, 1 \leq i \leq n-i \\ N_{n-1,n} = \left(\mid s \mid^{(m/n)} + (\mid \dot{s} \mid^{(m/(n-1))} .. \mid s^{(n-2)} \mid^{(m/(m/2))} \right)^{(1/m)} \\ \phi_{0,n} = s \\ \phi_{1,n} = \dot{s} + \beta_1 N_{1,n} sign(s) \\ \phi_{i,n} = S^i + \beta_i N_{i,n} sign(\phi_{i-1,n}), 1 \leq i \leq n-i \end{cases} \tag{4.36}$$

The control for a n order system is written:

$$u = -\alpha . sign . \phi_{n-1,n}(s, \dot{s}, \ddot{s}, \cdots, s^{(n-1)}) \tag{4.37}$$

This control is discontinuous, a second algorithm makes it possible to remove the discontinuities except at the origin (quasi-continuous control algorithm).

4.4.5 Quasi-continuous control algorithm

The quasi-continuous high order sliding mode control (QC-HOSM) was recently developed by [Levant, 2003] according to the principle of homogeneity [Levant, 2005]. This type of control belongs to the theory of systems with variable structure and ensures the convergence of the state of the system to the origin in finite time Figure 4.12. The QC-HOSM is defined by:

$$u = -\alpha.\psi_{n-1,n}(s, \dot{s}, \ddot{s}, \cdots, s^{(n-1)}) \tag{4.38}$$

Where $\phi_{0,n} = 0$, $N_{0,n} =\mid s \mid$

$$\begin{cases} \psi_{0,n} = \frac{\phi_{0,n}}{N_{0,n}} = sign(s) \\ \\ \phi_{i,n} = s^{(i)} + \beta i N_{i-1,n}^{\frac{n-i}{n-i+1}} \psi_{i-1,n} \\ \\ N_{i,n} =\mid s \mid^{(i)} \beta i N_{i-1,n}^{n-i+1} \psi_{i-1,n} \\ \\ \psi_{i,n} = \frac{\phi_{i,n}}{N_{i,n}} \end{cases} \tag{4.39}$$

Moreover, $N_{i,n}$ is a positive value, ($N_{i,n} = 0$ if $s = \dot{s} = \ddot{s} = \cdots = s^{(n-1)} = 0$). The function $\psi_{n-1,n}(s, \dot{s}, \ddot{s}, \cdots, s^{(n-1)})$ is continuous everywhere except at the point where

$$s = \dot{s} = \ddot{s} = \cdots = s^{(n-1)} = 0$$

The choice of parameters $\beta_1, \beta_2, \cdots, \beta_{n-1}$, $\alpha > 0$ determines a valid control family for systems of relative degree n. The parameter α is chosen specifically for all fixed values K_m, K_M, C_0 such that:

$$\alpha.K_m - C_0 > 0 \tag{4.40}$$

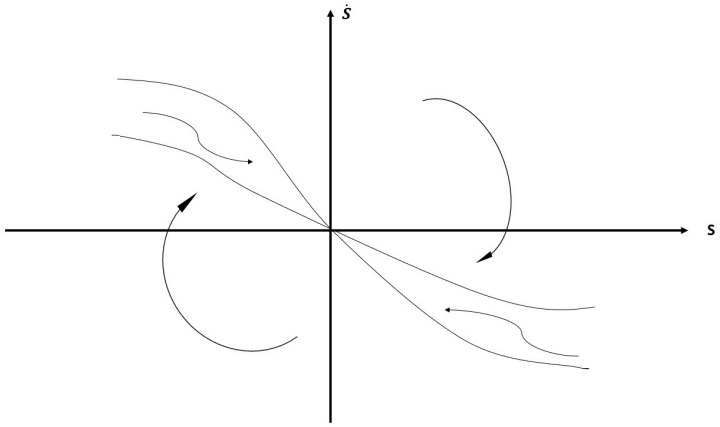

Figure 4.12: Convergence of the QC-HOSM algorithm.

The command (4.38) for 1 to 3 is chosen as follows:

$$u = -\alpha \cdot sign(s) \tag{4.41}$$

$$u = -\alpha \frac{\dot{s} + \mid s \mid^{\frac{1}{2}} sign(s)}{\mid \dot{s} \mid + \mid s \mid^{\frac{1}{2}}} \tag{4.42}$$

$$u = -\alpha \frac{\ddot{s} + 2(\mid \dot{s} \mid + \mid s \mid^{\frac{2}{3}})^{\frac{-1}{2}} [\dot{s} + \mid s \mid^{\frac{2}{3}} sign(s)]}{\mid \ddot{s} + \mid + 2(\mid \dot{s} \mid + \mid s \mid^{\frac{2}{3}})^{\frac{1}{2}}} \tag{4.43}$$

4.5 Integral fast terminal sliding mode control

IFTSMC is a new type of terminal sliding mode control which was invented by the scientist Venkataraman and Gulati [Venkataraman and Gulati, 1993] in the jet propulsion laboratory. It is a nonlinear and robust control based on the concept of the conventional TSMC and through the development of SMC. The command law u of the IFTSMC consists of two terms, a discontinuous

term u_{sw} that remains the system on the sliding surface, and an equivalent term u_{eq} that brings the system to the sliding surface [Slotine et al., 1991]. The total command law can be expressed as Equation (4.44).

$$u = u_{eq} + u_{sw} \tag{4.44}$$

The discontinuous term u_{sw} is defined in Equation (4.45); where, where k is a positive constant and sign(s) is the signum function [Utkin et al., 1999].

$$u_{sw} = -k \cdot sign(s) \tag{4.45}$$

The equivalent term u_{eq} is obtained by setting a sliding surface s and is finally achieved by establishing $\dot{s} = 0$ [Slotine et al., 1991]. The sliding surface given in Equation (4.46) is proposed; where the parameters α, λ, p and q are constants that satisfy the following condition: $\alpha > 0$, $\lambda > 0$, $p > 0$, $q > 0$, $1 < p/q < 2$ [Rizi and Eliasi, 2020, Feng et al., 2002, Yu and Zhihong, 2002].

$$s = e_r + \alpha \int_0^t e_r.dt + \lambda \left(\int_0^t e_r.dt \right)^{p/q} \tag{4.46}$$

4.6 Conclusion

In this chapter, we have presented the principle of sliding mode such as the first order, the high order and the new strategy integral fast terminal sliding mode. These controllers are consist of two elements: A hypersurface on which the system must evolve. A control law forcing the system to reach this sliding surface and remain there until equilibrium. Besides, we give a detailed presentation of several types of controllers, based on high order sliding modes (particularly the best known: order 2 and 3) with a convergence in finite time towards an objective of relative degree greater than 1. These methods can improve asymptotic precision or reduce chattering.

Chapter 5

CONTROL TECHNIQUES IMPLEMENTATION

> It is the hard work, passion, and constant and consistent improvement that results in success.
>
> *Jon Gordon*

5.1 Introduction

This chapter will focus on the real-time implementation of the IFTSMC and the QC-HOSM high order sliding mode controller on DC/DC converter type boost linked to a PEMFC power system. In addition to this work, a simulation implementation is used to verify the effectiveness of the PID controller optimised by PSO. We start first with the mathematical modelling of the boost and the calculation of the corresponding equivalent command. The experimental and simulation results are presented with discussion.

5.2 SMC implementation

The first step in the design of the control is the choice of the switching surface. We consider the nonlinear system described by Equation (5.1):

$$\dot{x} = f(t, x) + g(t, x)u \tag{5.1}$$

Where, $f(t, x)$ and $g(t, x)$ are nonlinear functions, u is a discontinuous and bounded command depending on the state x and time t. The tracking error e_r is defined by Equation (5.2), while x_d represents the desired current.

$$e_r = x_1 - x_d \tag{5.2}$$

The general formula of the sliding surface is defined by Equation (5.3):

$$s = \left(\frac{d}{dt} + \lambda\right)^{n-1} e_r \tag{5.3}$$

Where n is the system's relative degree ($n = 1$), λ is a positive constant chosen by the operator. It should be noted that a large value of λ implies a fast system response. However, very fast response can lead to overshoot or even system instability. On the other hand, low value of λ implies a slow system response but this leads to decrease the overshoot. Thereby, the sliding surface also can be written as Equation (5.4):

$$s = e_r \tag{5.4}$$

Using the boost converter model Equation (2.48) and Equations (5.2), (5.3), and (5.4), the surface derivative can be expressed as Equation (5.5):

$$\dot{s} = \frac{1}{L}(V_{FC} - x_2) + \frac{x_2}{L}u \tag{5.5}$$

The command law u is the sum of two components, the equivalent component u_{eq}, and the discontinuous component u_{sw}. It can be written as Equation (5.6):

$$u = u_{eq} + u_{sw} \tag{5.6}$$

Where, u_{eq} is the equivalent control which is deduced from the relation of ($\ddot{s} = 0$). Its main role is ensuring that the system hits the sliding surface. The equivalent control can be expressed as Equation (5.7):

$$u_{eq} = -\frac{1}{x_2}\left(V_{FC} - x_2\right) \tag{5.7}$$

u_{sw} is the switching control its key aim is to ensure the stability and the convergence by holding the system on the sliding surface. In this work, the firs order switching control is given by the equation (5.8) :

$$u_{sw} = -k\frac{L}{x_2}sign(s) \tag{5.8}$$

In order to prove the stability, the following Lyapunov function is proposed: $V = \frac{1}{2}\dot{s}^2$. The time derivative of this function is calculated in Equation (5.9).

$$\begin{aligned}
\dot{V} &= s\dot{s} \\
&= s\left[\frac{1}{L}(V_{FC} - x_2) + \frac{x_2}{L}u\right] \\
&= s\left[\frac{1}{L}(V_{FC} - x_2) + \frac{x_2}{L}(u_{eq} + u_{sw})\right] \\
&= s\left[\frac{1}{L}(V_{FC} - x_2) + \frac{x_2}{L}u_{eq} + \frac{x_2}{L}u_{sw}\right] \\
&= s\left[\frac{1}{L}(V_{FC} - x_2) + \frac{x_2}{L}\left(-\frac{1}{x_2}\left(V_{FC} - x_2\right)\right) + \frac{x_2}{L}\left(-k\frac{L}{x_2}sign(S)\right)\right] \\
&= -k \cdot s \cdot sign(s) \\
&= -k \cdot |s| \\
&\leq 0
\end{aligned} \tag{5.9}$$

$V \geq 0$ and $\dot{V} \leq 0$, therefore, according to the Lyapunov theory, the PEMFC system is stable.

5.3 IFTSMC implementation

The total command law of the IFTSMC controller can be expressed as Equation (5.10).

$$u = u_{eq} + u_{sw} \tag{5.10}$$

The discontinuous term u_{sw} is defined in Equation (5.11); where k is a positive constant and sign(s) is the signum function.

$$u_{sw} = -\frac{L}{V_o} \cdot k \cdot sign(s) \tag{5.11}$$

The sliding surface of the IFTSMC is given in Equation (5.12)

$$s = e_r + \alpha \int_0^t e_r.dt + \lambda \left(\int_0^t e_r.dt \right)^{p/q} \tag{5.12}$$

The time derivative of the surface can be expressed as in Equation (5.13).

$$\dot{s} = \dot{e_r} + \alpha \cdot e_r + \lambda \left(\frac{p}{q} \right) \cdot e_r \cdot \left(\int_0^t e_r.dt \right)^{\frac{p-q}{q}} \tag{5.13}$$

Also, the error expression was already defined in the Equation (5.2). As the reference current is constant, therefore, the error derivative expression can be obtained in the following Equation (5.14).

$$\dot{e}_r = -\frac{(1-d)}{L} i_L + \frac{1}{L} \cdot V_{FC} \tag{5.14}$$

Thus, through a combination of Equation (5.13), with the latter Equation (5.14), a complete expression of the surface derivative is gathered in the following Equation (5.15).

$$\begin{aligned} \dot{s} &= -\frac{(1-d)}{L}.V_o + \frac{1}{L}.V_{FC} + \alpha \cdot e_r + \lambda \left(\frac{p}{q} \right) \cdot e_r \cdot \left(\int_0^t e_r.dt \right)^{\frac{p-q}{q}} \\ &= \frac{u}{L}.V_o - \frac{1}{L}.V_o + \alpha \cdot e_r + \frac{1}{L}.V_{FC} + \lambda \left(\frac{p}{q} \right) \cdot e_r \cdot \left(\int_0^t e_r.dt \right)^{\frac{p-q}{q}} \end{aligned} \tag{5.15}$$

Finally, stating that that $\dot{s} = 0$, the equivalent term of the control law is achieved as in Equation (5.16).

$$u_{eq} = 1 - \frac{V_{FC}}{V_o} - \frac{\alpha \cdot e_r \cdot L}{V_o} - \frac{\lambda . e_r . L}{V_o} \left(\frac{p}{q}\right) \cdot \left(\int_0^t e_r . dt\right)^{\frac{p-q}{q}} \tag{5.16}$$

Previous remarks in terms of the chosen surface, provided certain limitations to take into account at the moment of the constants tuning. However, these have also been adjusted through the minimization of the IAE that belongs to the Equation (5.17). This aims to achieve a suitable performance by taking into account the error reduction in real time.

$$IAE = \int_0^t |e(t)| dt \tag{5.17}$$

The previous obtained control law can be analyzed in terms of the Lyapunov theory of stability. This states that if there exist a positive definite function: $R^n \rightarrow R$ so that $V\ (x) > 0$, $V\ (0) = 0$, $V(\infty) = \infty$ and $\dot{V}(x) < 0$, $\forall\ x \neq 0$; therefore the dynamical system is asymptotically stable. Consequently, to prove the stability of the PEMFC system, a positive definite Lyapunov candidate function is chosen as the Equation (5.18).

$$V(s) = \frac{1}{2} s^2 \tag{5.18}$$

Thus, the derivative of the latter expression is established in the next expression such that $\dot{s}$ from (5.15) is replaced as follows.

$$\begin{aligned} \dot{V}(s) &= s.\dot{s} \\ &= s \left(\frac{u}{L} . V_o - \frac{1}{L} . V_o + \frac{1}{L} . V_{FC} + \alpha \cdot e_r + \lambda \left(\frac{p}{q}\right) \cdot e_r \cdot \left(\int_0^t e_r . dt\right)^{\frac{p-q}{q}} \right) \end{aligned} \tag{5.19}$$

The replacement of the control term u with the Equations (5.10), (5.11) and (5.16), yields to the following expression. Further mathematical development as follows, accomplishes with the Lyapunov stability proof since $\dot{V}(s)$ is concluded to be less or equal to zero.

$$\begin{aligned}
\dot{V}(s) &= s\left(\frac{u}{L}.V_o - \frac{1}{L}.V_o + \frac{1}{L}.V_{FC} + \alpha.e_r + \lambda\left(\frac{p}{q}\right).e_r.\left(\int_0^t e_r.dt\right)^{\frac{p-q}{q}}\right) \\
&= \frac{s.V_o}{L}\left(1 - \frac{V_{FC}}{V_o} - \frac{\alpha.e_r.L}{V_o} - \frac{\lambda.e_r.L}{V_o}\left(\frac{p}{q}\right).\left(\int_0^t e_r.dt\right)^{\frac{p-q}{q}} + u_{sw}\right) \\
&\quad + s\left(-\frac{1}{L}.V_o + \frac{1}{L}.V_{FC} + \alpha \cdot e_r + \lambda\left(\frac{p}{q}\right) \cdot e_r \cdot \left(\int_0^t e_r.dt\right)^{\frac{p-q}{q}}\right) \\
&= -k \cdot s \cdot sign(s) \\
&= -k \cdot |s| \\
&\leq 0 \qquad (5.20)
\end{aligned}$$

In order to reduce ripples and chattering phenomenon, a digital filter was designed in Matlab. The command (b,a,x) requires the numerator b and denominator a coefficients which represent a rational transfer function, whereas the data input is defined as x. Provided that $a = 1$ and $b = 1/N$, the result is a moving-average expression that filters the high frequency signals along the the number of elements N to be filtered (this is also known as the filter order) expressed in Equation (5.21) [Zhao et al., 2020].

$$y[k] = \sum_{i=1}^{N} \frac{1}{N} x[k-i] \qquad (5.21)$$

The implementation of previous expression has been done through a Finite Impulse Filter (FIR) block in Simulink. The filter order was defined along the research as it is explained in the following sections. The sampling frequency was chosen is $10kHz$ since it fits with the hardware limitations and data acquired.

5.4 QC-HOSM implementation

In order to design the QC-HOSM controller, we consider the nonlinear system of the boost converter described by the Equation (2.48) and the error

equation which is described by the Equation (5.2) and using the formula of the sliding surface which defined by Equation (5.22):

$$s = (\frac{d}{dt} + \lambda)^{n-1} \int_0^t e_r dt \tag{5.22}$$

Where n is the system's relative degree ($n = 2$). Thereby, the sliding surface also can be written as Equation (5.23):

$$s = e_r + \lambda \int_0^t e_r dt \tag{5.23}$$

Using the boost converter model Equation (2.48) and Equations (5.22), and (5.23), the surface derivative can be expressed as Equation (5.24):

$$\dot{s} = \frac{1}{L}(V_{FC} - x_2) + \lambda e_r + \frac{x_2}{L}u \tag{5.24}$$

To design the QC-HOSM, the uncertain second-order system should be written as Equation (5.25)

$$\ddot{s} = \psi(x,t) + \gamma(x,t)\nu \tag{5.25}$$

Where $\nu = \dot{u}$ is the command derivative, $\psi(x,t)$ and $\gamma(x,t)$ are determined by Equation (5.26):

$$\begin{aligned}
\ddot{s} &= \frac{1}{L}\left(\dot{V_{FC}} - \dot{x}_2\right) + \lambda\dot{e} + \frac{1}{L}\left(\dot{x}_2 \cdot u + x_2 \cdot \dot{u}\right) \\
&= \frac{1}{L}\left(\dot{V_{FC}} - \dot{x}_2\right) + \lambda\left(\frac{1}{L}\left(V_{FC} - x_2\right) + \frac{1}{L}x_2 \cdot u\right) + \frac{1}{L}\left(\dot{x}_2 \cdot u + x_2 \cdot \dot{u}\right) \\
&= \frac{1}{L}\left[(u-1)\dot{x}_2 + \dot{V_{FC}} + \lambda(u-1)x_2 + \lambda V_{FC}\right] + \frac{1}{L}x_2 \cdot \dot{u} \\
&= \underbrace{\frac{1}{L}\left[(u-1)\dot{x}_2 + \dot{V_{FC}} + \lambda(u-1)x_2 + \lambda V_{FC}\right]}_{\psi} + \underbrace{\frac{1}{L}x_2}_{\gamma} \cdot \nu
\end{aligned} \tag{5.26}$$

Assuming that $\psi(x,t)$ and $\gamma(x,t)$ are bounded as Equation (5.27):

$$|\ \psi(x,t)\ | < C_0, 0 < K_m \leq |\ \gamma(x,t)\ | \leq K_M \tag{5.27}$$

Where C_0, K_m, K_M are positive constants. The command law ν is the sum of two components, the equivalent component, and the discontinuous component. It can be written as Equation (5.28):

$$\nu = \nu_{eq} + \nu_{sw} \tag{5.28}$$

Where, ν_{eq} is the equivalent control. Which is deduced from the relation of ($\ddot{s} = 0$). Its main role is ensuring that the system hits the sliding surface. The equivalent control can be expressed as Equation (5.29):

$$\nu_{eq} = -\frac{\psi}{\gamma} = -\frac{1}{x_2} \cdot [(u-1)\dot{x_2} + \dot{V_{FC}} + \lambda(u-1)x_2 + \lambda V_{FC}] \tag{5.29}$$

ν_{sw} is the switching control. Its key aim is to ensure the stability and the convergence by holding the system on the sliding surface. In this work, we propose the switching control as Equation (5.30):

$$\nu_{sw} = -\alpha \frac{\dot{s} + |s|^{1/2} sign(\dot{s})}{|\dot{s}| + |s|^{1/2}} \tag{5.30}$$

Where, the parameter α could be determined using the condition given in Equation (5.31).

$$\alpha \cdot K_m < C_0 \tag{5.31}$$

In order to prove the stability, the following Lyapunov function is then proposed: $V = \frac{1}{2}\dot{s}^2$. The time derivative of this function is calculated in Equation (5.32).

$$
\begin{aligned}
\dot{V} &= \dot{s}\ddot{s} \\
&= \dot{s}(\psi + \gamma\nu) \\
&= \dot{s}\left(\frac{1}{L}\left[(u-1)\dot{x}_2 + \dot{V_{FC}} + \lambda(u-1)x_2 + \lambda V_{FC}\right] + \frac{1}{L}x_2\nu\right) \\
&= \dot{s}\left(\frac{1}{L}\left[(u-1)\dot{x}_2 + \dot{V_{FC}} + \lambda(u-1)x_2 + \lambda V_{FC}\right]\right) + \\
&\quad \dot{s}\frac{x_2}{L}\left(-\frac{1}{x_2}\left[(u-1)\dot{x}_2 + \dot{V_{FC}} + \lambda(u-1)x_2 + \lambda V_{FC}\right] + \nu_{sw}\right) \\
&= -\alpha \cdot \frac{x_2}{L} \cdot \dot{s} \cdot \frac{\dot{s} + |s|^{1/2} sign(\dot{s})}{|\dot{s}| + |s|^{1/2}} \\
&= -\alpha \cdot \frac{x_2}{L} \cdot \dot{s} \cdot sign(\dot{s}) \cdot \frac{\dot{s} \cdot sign(\dot{s}) + |s|^{1/2}}{|\dot{s}| + |s|^{1/2}} \\
&= -\alpha \cdot \frac{x_2}{L} \cdot |\dot{s}| \cdot \frac{|\dot{s}| + |s|^{1/2}}{|\dot{s}| + |s|^{1/2}} \\
&= -\alpha \cdot \frac{x_2}{L} \cdot |\dot{s}| \\
&\leq 0
\end{aligned}
\tag{5.32}
$$

$V \geq 0$ and $\dot{V} \leq 0$, therefore, according to the Lyapunov theory, the PEMFC system is stable.

5.5 Experimental device overview

The control strategies are configured and installed in the Matlab/Simulink environment, and then, it is loaded into the DSP card system for real-time operation. The experimental test bench, including the FC50 fuel cell, programmable load resistance (BK-PRECISION), DSPACE DS1104, DSPACE DS1202, workstation computer, and step-up converter, are presented in Figure 5.1.

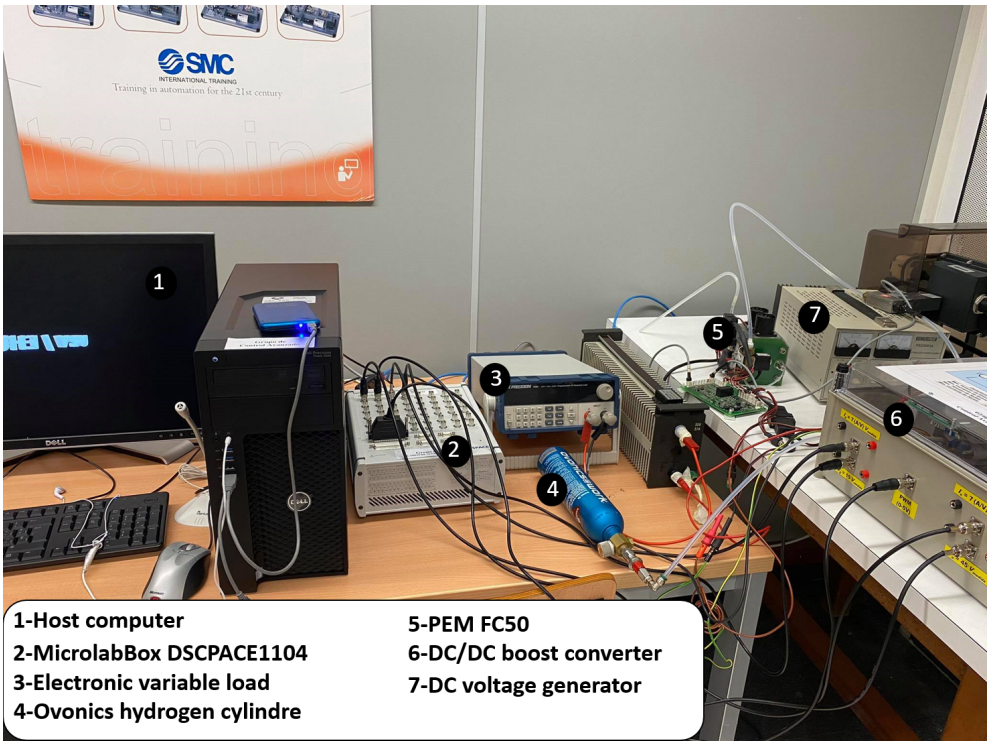

Figure 5.1: Integrated experimental system.

The fuel cell FC50 stack characteristics are listed in Table. 5.1. It is composed of ten cells that are able to generate power up to more than 50W at DC voltage equal to 5V. It is alimented by a hydrogen cylinder, which is linked to a manometer to reduce the inlet pressure. It also consists of an external ventilator that provides oxygen and cooling to the stack. The controller board 9 is the main component of the fuel cell auxiliaries. It plays the role of the distribution centre for all the data among the fuel cell components such as the software, the H_2 flow meter, the fans, and the temperature sensors. It has many functions such as measuring the system parameter, controlling the Fans, connecting/disconnecting load by integrated relay, communicating to the PC, providing simple operation, protect the stack from short circuits and over-loads, as well as ensuring the safety of the PEMFC.

Table 5.1: FC50 fuel cell stack technical data.

Specific properties	**Symbol**	**Parameters**
PEM fuel class	FC50	PEM fuel cell
Dimensions	W× D× H	$12 \times 10.3 \times 13.5\ cm$
Number of cells	N_{fc}	10 Cells
PEM surface area	S_{pem}	$25cm^2$
Operating fuel	H_2	Hydrogen gas
Cooling system	-	Integrated ventilator
Stack weight	-	1150 g
Open-circuit voltage	V_{oc}	9 V
Nominal stack voltage	$V_{nominal}$	5 V
Nominal stack current	$I_{nominal}$	8 A
Maximum generated current	I_{max}	10 A
Nominal stack power	$P_{nominal}$	40 W
Maximum generated power	P_{max}	50 W
Operating temperature range	T	15- 50
Maximum start temperature	T_{start}	45
Inlet-Outlet pressure kit 15 bar	-	1-15, 0.6 bar
Inlet-Outlet pressure kit 200 bar	-	200, 1-15 bar
Hydrogen purity	-	5.0 (99.99 %)
Hydrogen input pressure	-	0.4-8 bar
Rated hydrogen consumption	-	580 sml/min
Maximum hydrogen consumption	-	700 sml/min

The control of continuous systems in real-time is done using a PC connected to the DSPACE DS1202 and DSPACE DS1104 cards. The first is used for the implementation of the IFTSMC where, the second is used for the implementation of the QC-HOSM. The MicroLabBox DSPACE DS1202 card is a powerful tools that used to linkage between the software (Simulink) and the hardware (the converter), via its real-time interface (RTI). It has

the ability to receive and send the information among the converter, the Matlab/Simulink™ and ControlDesk software, as well as monitoring the signals of the real processes throughout the operation. It contains two digital input/output PWM ports, two RS232, two CAN, as well as 48 input/output channels which make it adapted to many different functions and activities. Furthermore, it has a powerful CPU of 2GHz and a field-programmable gate array (FPGA) that allows the user to make tests even for speedy control loops. The DSPACE DS1104 card, which have a powerful central processor MPC8240 with a frequency speed up to 250 MHZ. It also contains eight digital to analogue converters (DAC) and eight analogues to digital converters (ADC). These converters are related to a specific signal. As shown in Figure 5.2, whose supplied voltage is between -10V and +10V. The DSPACE DS1104 uses two types of ADC: four multiplexed ADC converters (ADC-C1 to ADC-C4) for the channels signals (ADCH1 to ADCH4), with 16-bit resolution and signal-to-noise ratio SNR $>$ 80 dB, and four ADC converters (ADC-C5 to ADC-C8) for the channels signals (ADCH5 to ADCH8), with 12-bit resolution and signal-to-noise ratio SNR $>$ 70 dB. In addition to that, it has several interfaces, including digital input and output as well as incremental encoders. It also has a DSP slave, the TMS320F240 DSP, which is used to generate the PWM signals. Where this latter is used to control the step-up DC/DC converter. The control process is built through the following three stages: construction of the control system using simulink blocks, simulation of the system to display the results in different scenarios, and finally the execution of the model in real-time through the DS1104 and DSPACE DS1202 cards for the two experimental study IFTSMC and QC-HOSM respectively.

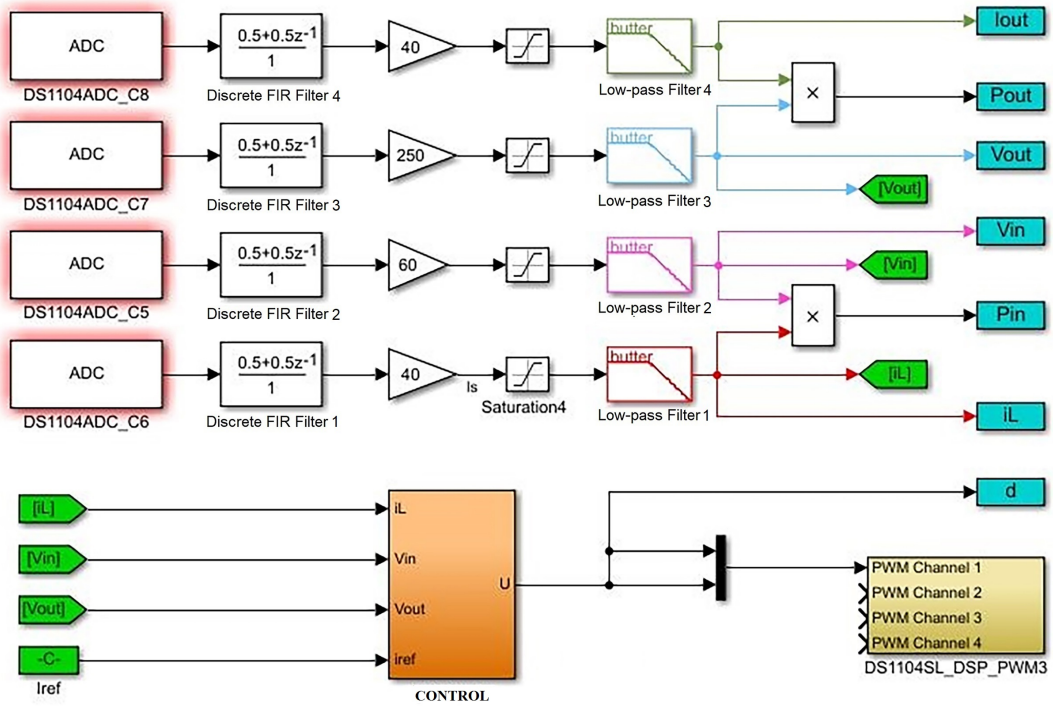

Figure 5.2: Real-time control structure.

The step-up DC/DC converter is constructed by the research-group-TEP192, Huelva University, Spain. Its characteristics are listed in Table. 5.2.

Table 5.2: Step-up converter characteristics

Components	**Symbol**	**Parameters**
Schottky Barrier Diode	SBD	MURF1560 GT
Input Capacitor	C_{in}	1500 μF
Output Capacitor	C_{out}	3000 μF
Inductance	L	6 μH
Max input-output current	I_{inMax}, I_{outMax}	20-20
Max input-output voltage	V_{inMax}, V_{outMax}	60-200 Volt
Insulated gate bipolar transistor	IGBT	HGT40N60B3
Switching frequency	F_{sw}	20 KHZ

5.6 Results and Discussion

The Figure 5.3 shows the FC50 current-potential (IV) and current-power (IP) characteristics curves for different operating temperatures. According to this figure, it is notable that the FC50 performance is improved by enhancing the temperature from 20 to 46. This could be interpreted by the raise of the membrane conductivity. However, for temperatures up to more than 46, the membrane starts to dry, which causes a lack of the relative humidity. As a consequence, a drop in the fuel cell performance has occurred.

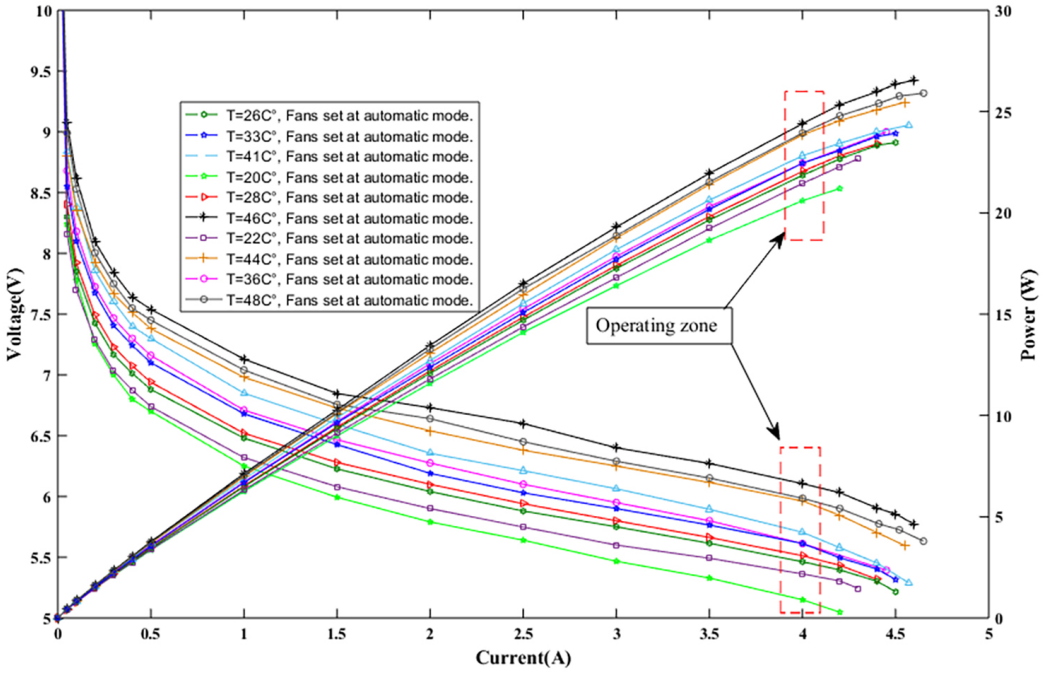

Figure 5.3: Graph showing the characteristics of I-V and I-P for a different temperature.

Aiming to hold the PEMFC operating at an adequate power point, the MPPT algorithms are used. However, due to the integrated security system which protects the stack from damage, the implementation of the MPPT could be a hard task. Hence, it prevents the PEMFC to operate with high currents in the concentration zone at which the locale of the maximum power.

In other words, the operating current which corresponds to the MPP could be near to the maximum generated current at which the security system turns the PEMFC off so as to protect the membrane from the damage. Therefore, it is not possible to achieve the MPP value experimentally. To deal with this condition, we have constructed an operating zone, as shown in Figure 5.3, at which up to more than 91% of the maximum generated power could be extracted.

In order to reveal the effectiveness, and the performance of the proposed algorithms QC-HOSM and IFTSMC, load resistance are varied from 20Ω to 50Ω at time $t = 20s$, and from 50Ω to 20Ω at time $t = 40s$ for IFTSMC and 20Ω to 50Ω at time $t = 25s$, and from 50Ω to 20Ω at time $t = 45s$ for the QC-HOSM. Furthermore, to find out the advantages of the proposed algorithms, a comparison study is done with conventional first-order SMC for the QC-HOSM and PI controller for the IFTSMC. The proposed controllers coefficients used in this work are enlisted in Table. 5.3, 5.4.

Table 5.3: QC-HOSM and SMC parameters gains.

QC-HOSM	**SMC**
$\lambda = 0.5$	$k = 0.5$
$\alpha = 0.1$	–

Table 5.4: IFTSMC and PI parameters gains.

IFTSMC	**PI**
$p = 1$	$K_{cr} = 0.04$
$q = 3$	$P_{cr} = 12.08$
$\alpha = 0.1$	$K_p = 0.02$
$\lambda = 0.1$	$K_i = 10$
$k = 0.5$	–

5.6.1 QC-HOSM results

Thus, Figure 5.4.**a** shows the duty cycle signal for both algorithms. It is noticed that both of the algorithms show a soft and smooth rise to the desired reference value. However, it is clearly shown that the proposed QC-HOSM algorithm effectively overcomes the drawbacks of the conventional first SMC by reducing its chattering phenomenon. Figure 5.4.**b** and (**c**) show the FC50 current and voltage signals. The effectiveness of both algorithms when experiencing significant changes in load resistance is clearly demonstrated at $t = 25s$ and $t = 45s$. Hence, at the instant $t = 25s$, the SMC shows an undershoot current of $1A$, and an overshoot voltage of $0.54V$. For the instant $t = 45s$, an overshoot current of $2.1A$, and an undershoot voltage of $0.96V$. On the other hand, at the instant $t = 25s$, the QC-HOSM algorithm shows an undershoot current of $1.85A$, and an overshoot voltage of $1V$. For the instant $t = 45s$, an overshoot current of $3.63A$, and an undershoot voltage of $1.82V$. However, these undershoot and overshoots are appeared only for short durations and then, they converge to the reference value. Thus, at the instant $t = 25s$, the response time of the SMC and the QC-HOSM are only $0.33s$ and $0.74s$, while at $t = 45s$ they are $0.42s$ and $0.92s$ respectively. Therefore, high robustness against load variations is achieved using both algorithms. The effectiveness of the proposed QC-HOSM over the conventional SMC appears in its capability to reduce the oscillations. Hence, chattering reduction of 84% could be attained. The Figure 5.4.**d** shows the trajectory of the generated power. It is obvious that the operating zone, which is already presented in Figure 5.3, is achieved with high robustness and global stability of the closed-loop system. The chattering magnitude using the conventional SMC is in the range of $20W$ and $26.6W$, while it is only in the range of $22.57W$ and $23.55W$ using the proposed QC-HOSM algorithm. It is therefore proven that the proposed algorithm succeeded in decreasing the chattering effect,

which will improve as a consequence of the fuel cell efficiency, lifetime, and the dynamic system behaviour.

The Figure 5.5 shows the behaviour of the step-up DC-DC converter output current, output voltage and output power, as well as the load resistance variation. According to this figure, despite of facing sharp resistance variation, the QC-HOSM shows gradual and smooth movements to the desired voltage at which the system runs in the operating zone. Furthermore, high performances such as low response-time, great robustness, high precision, as well as outstanding dynamic behaviour, are achieved.

According to these results, it is noticed that the SMC and QC-HOSM show a good behaviour against load resistance variations. However, it is clearly seen that the advantage of the QC-HOSM is its effectiveness to reduce the unwanted oscillation (chattering effect) with significant value. Thus, a chattering reduction of 84% is obtained which, as a consequence, will increase the accuracy and the overall system efficiency.

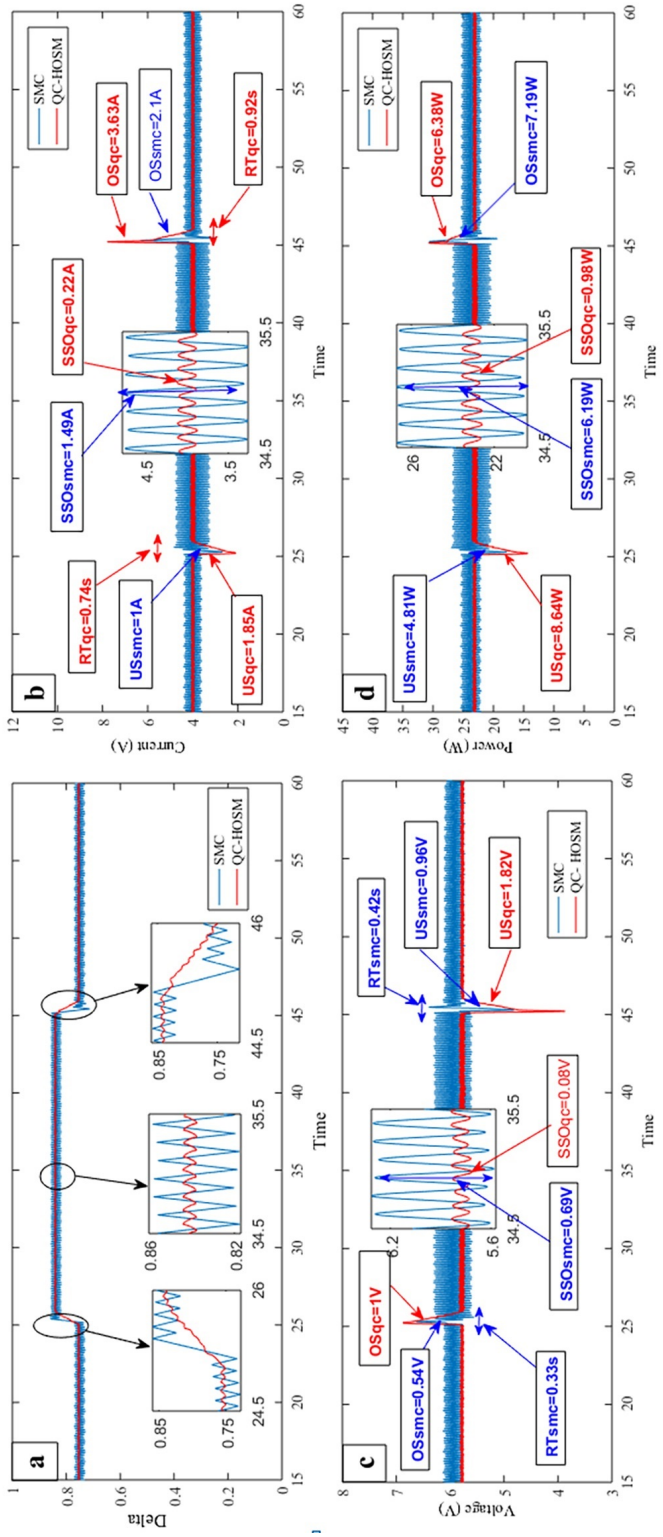

Figure 5.4: PEMFC different signals ; **a**: Duty cycle ; **b**: Stack current; **c**: Stack voltage ; **d**: Stack power.

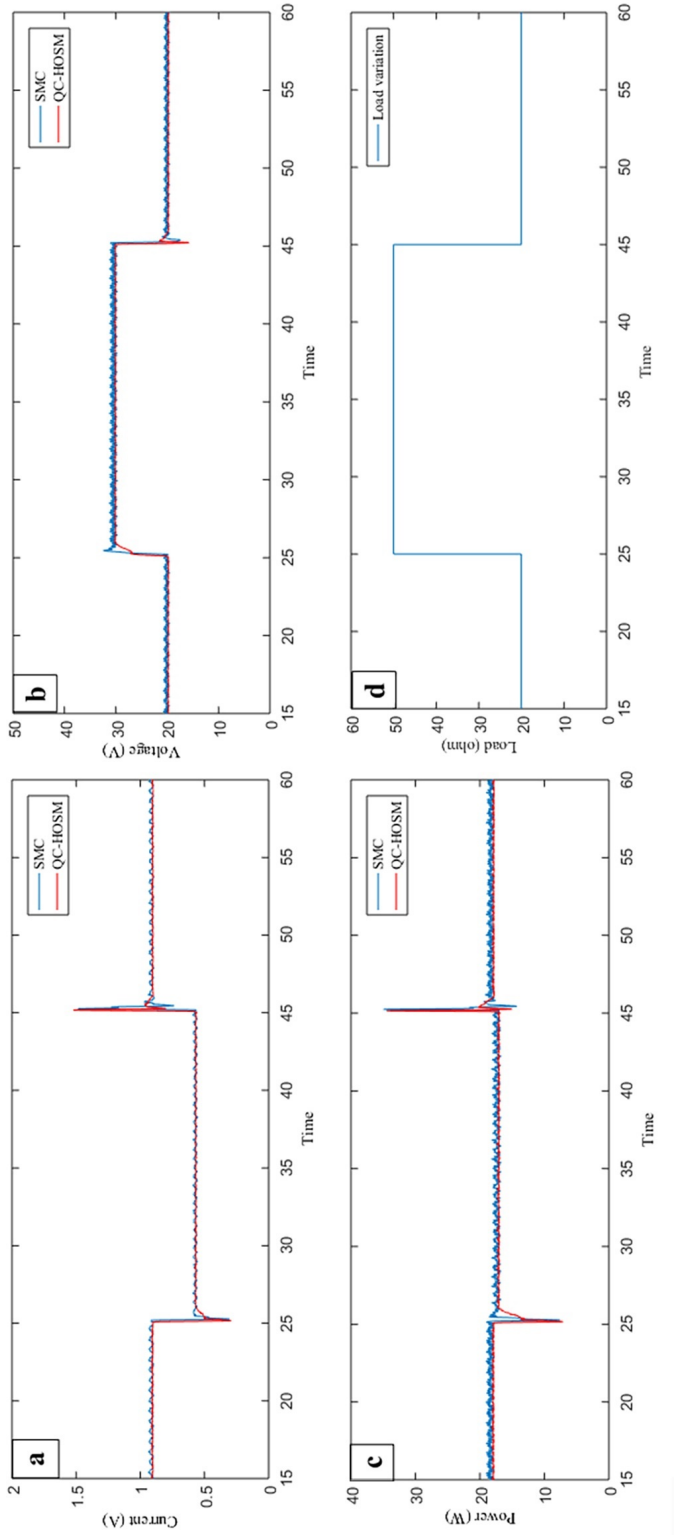

Figure 5.5: Step-Up converter output signals ; **a**: output current ; **b**: Output voltage ; **c**: Output power ; **d**: Load variations.

5.6.2 IFTSMC results

Load variations, the duty cycle signal for both PI and IFTSMC, as well as their generated errors, are presented in Figure 5.6. Despite the sharp variations of the load resistance, it is clearly shown that both of controllers succeeded to converge the error to zero value; which will guarantee as a result the stability of the system. The Figure 5.6 also demonstrates the drawbacks of the PI controller in terms of the converging time; hence, it takes up to more than 12 s to reach the equilibrium point while the proposed IFTSMC algorithm takes only 0.45 s.

The electric outputs of the FC-50W stack, under the application of PI and IFTSMC, are presented in Figure 5.7; where the three graphs shows, respectively, the stack current, stack voltage and stack power. At $t = 20$ s, by applying load variation from 20 Ω to 50 Ω, the PI shows an undershoot of 2.006 A in current, an overshoot of 1.147 V in voltage, and an undershoot of 10.05 W in power; while the proposed IFTSMC shows an undershoot of 1.997 A in current, an overshoot of 1.107 V in voltage, and an undershoot of 9.99 W in power. On the other hand, at $t = 40$ s, by applying load variation from 50 Ω to 20 Ω, the PI shows an overshoot of 4.086 A in current, an undershoot of 2.014 V in voltage, and an overshoot of 9.17 W in power; while the proposed IFTSMC shows an overshoot of 4.141 A in current, an undershoot of 2.012 V in voltage, and an overshoot of 9.26 W in power. According to these results, it is clear that both of PI and IFTSMC have almost the same performance in term of overshoots and undershoots; where the IFTSMC has an improvement of 0.06 W over the PI when increasing the load resistance, while the PI has an improvement of 0.09 W over the IFTSMC when decreasing the load resistance. However, it is clearly shown that the feature of the proposed IFTSMC appears in its capability to converge the

system to the reference value with high speed (response time = 0.45 s).

The Figure 5.8 shows the output signals behaviour of the step-up DC-DC converter. According to this figure, gradual and smooth movements to the desired value are obtained. However, in spite of the chattering phenomenon which is caused by the proposed IFTSMC control during the steady state, its robustness to converge the system in a short times which will results in a high tracking accuracy, is an important advantage over the conventional PI.

According to Figures 5.7 and 5.8, it is noticed that the chattering phenomenon, which is a normal behavior of sliding mode control, occurred in the steady state could represent an obstacle for the proposed IFTSMC control; therefore, to eliminate these ripples, a a digital filter that diminished the high frequency components along 400 points was applied to the duty cycle (command law). The filtered signals of the FC-50W stack are presented in Figure 5.9. This latter demonstrates that by applying a digital filter, a chattering reduction from 0.65 A, 0.33 V, 2.76 W Figure 5.7 to 0.08 A, 0.03 V, 0.36 W Figure 5.9, are respectively obtained. By means of power percentage, a chattering reduction up to 91% is obtained which results in a soft and smooth signals.

According to these results, it is clearly seen that the IFTSMC with the application of the digital filter has succeeded to keep the FC-50W stack operating at the desired power point while providing high tracking performance. Hence, high convergence speed with chattering reduction up to more than 91% are obtained using the proposed IFTSMC algorithm. Besides, soft and fast dynamic behavior while guaranteeing the system stability are also obtained.

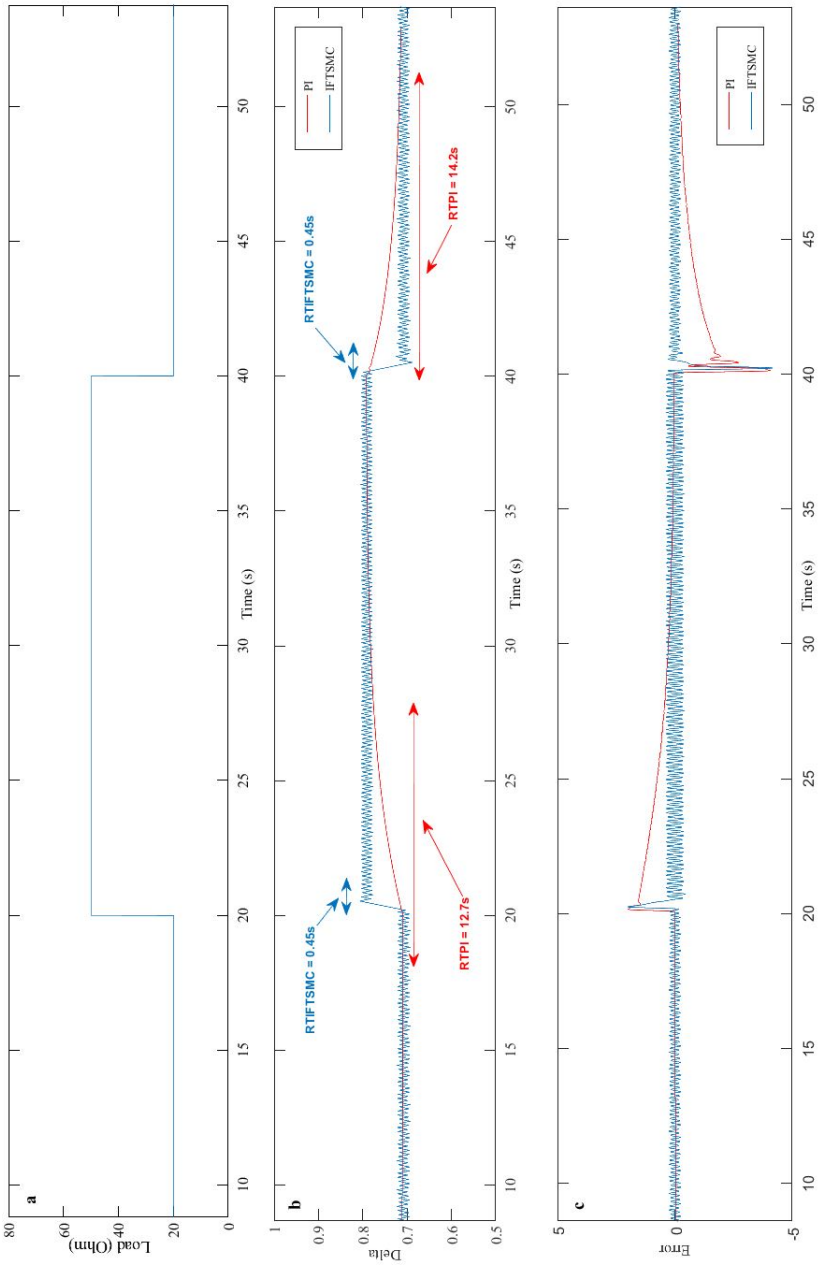

Figure 5.6: **a**: Load variations ; **b**: Duty cycle signal ; **c**: Error.

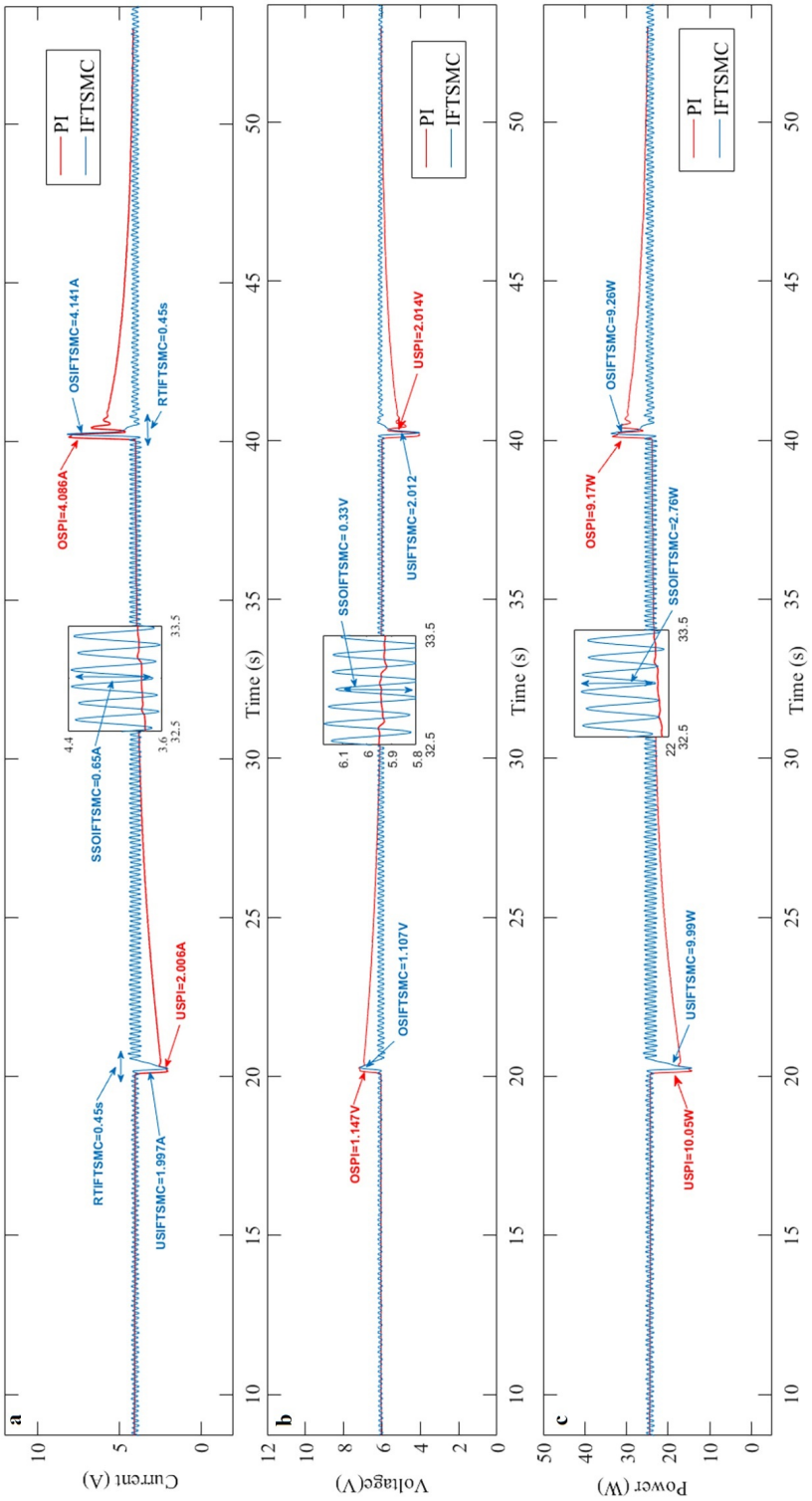

Figure 5.7: **a**: Stack current ; **b**: Stack voltage signal ; **c**: Stack power.

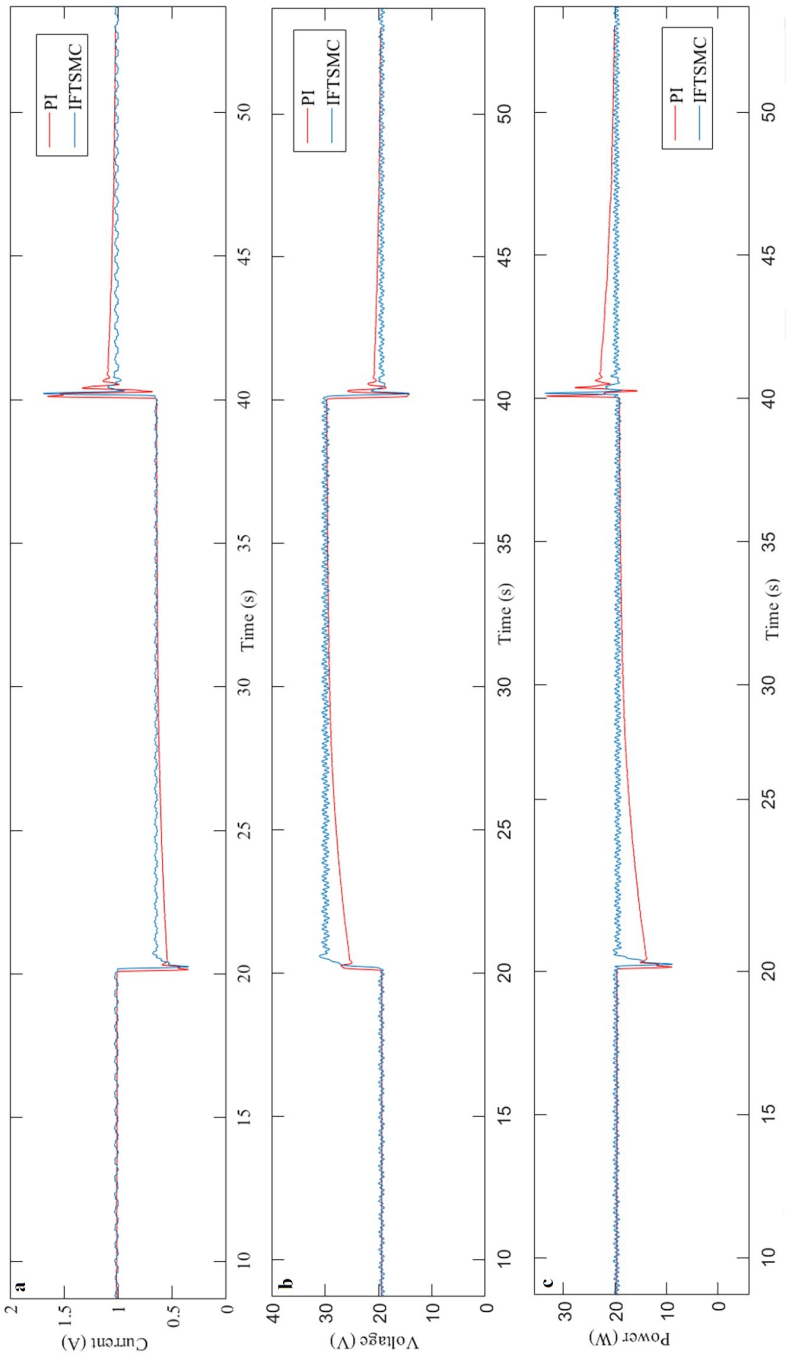

Figure 5.8: **a**: Boost converter output current ; **b**: Boost converter output voltage ; **c**: Boost converter output power.

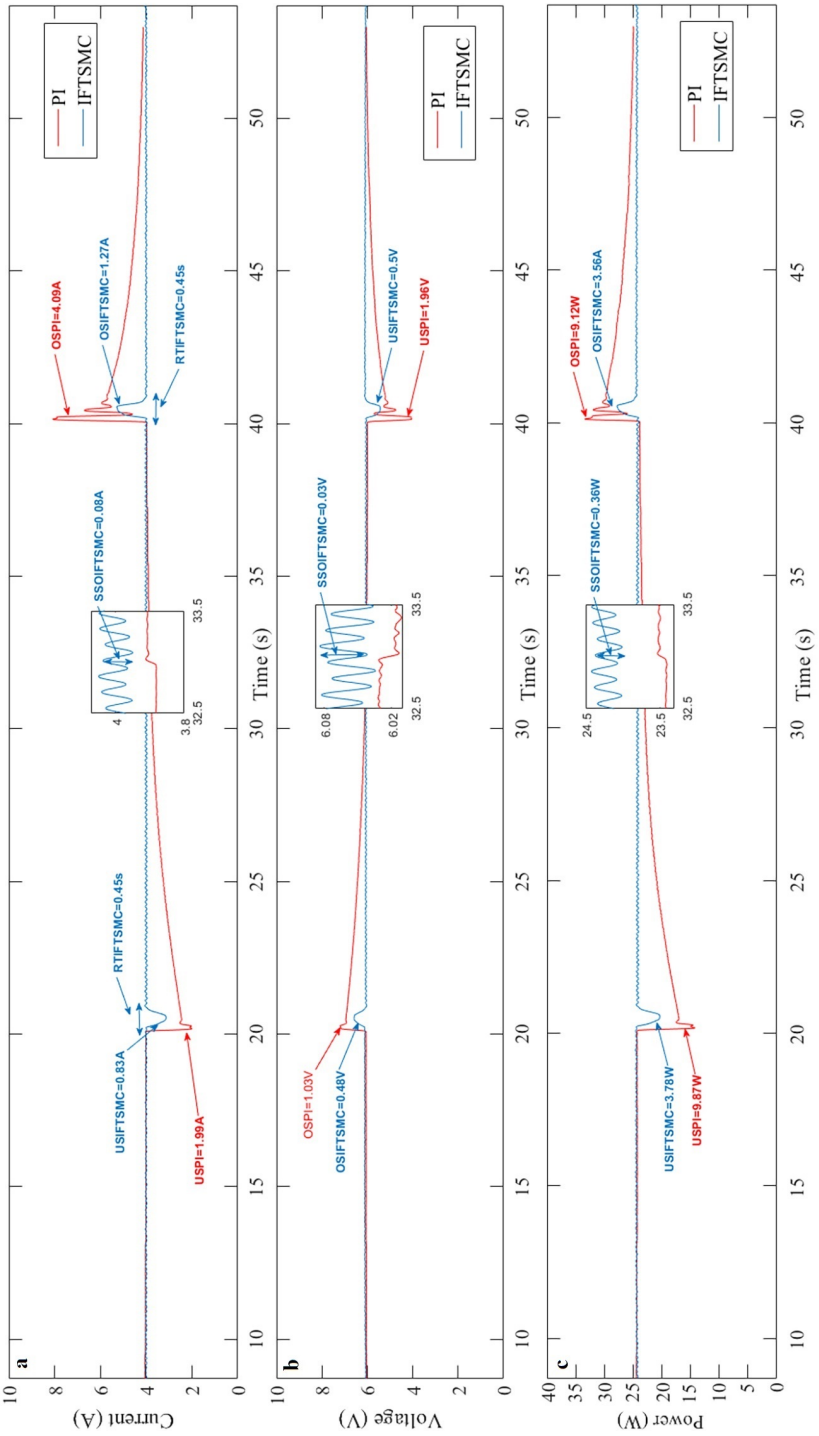

Figure 5.9: **a**: Filtered stack current ; **b**: Filtered stack voltage ; **c**: Filtered stack power.

5.6.3 PSO PID simulation results

The PID controller transfer function is given in Equation (5.33):

$$u = k_p.e(t) + k_i \int e(t)dt + k_d \frac{de(t)}{dt} \tag{5.33}$$

Aiming to keep and hold the PEMFC works at a desired current equal to $9A$, which is near to the MPPT zone, two control algorithms are based on PSO-PID and ZN are applied to the DC/DC boost converter under the Matlab/Simulink environment. The DC/DC boost converter, which we want to control, these parameters are: $C = 1500.10^{-}6F$, $L = 69.10^{-3}H$.

In order to see the robustness of the proposed controllers we applied a variable load from 20 Ω to 100 Ω, at time $t = 1.5s$ and a variable resistance from 100 Ω to 10 Ω at the time of $t = 3s$ as shown in Figure 5.10. The H_2 gas pressure is varied from $0.1bar$ at $t = 2s$ and $0.6bar$ at $t = 2s$ as shown in Figure 5.11. The specifications of the PSO method which is used in the simulation are given in Table. 5.5.

Table 5.5: Specifications of the PSO method.

Parameter	**Specification**
Swarm size	50
Cognitive parameters $c_1 = c_2$	1.494
Max inertia weigh	0.80
Min inertia weigh	0.40
Max iteration	100

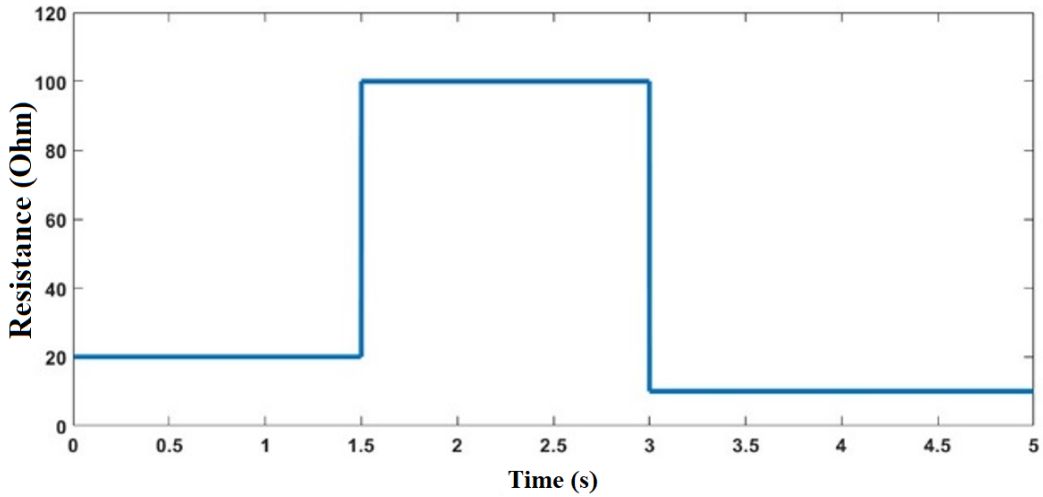

Figure 5.10: Load variations .

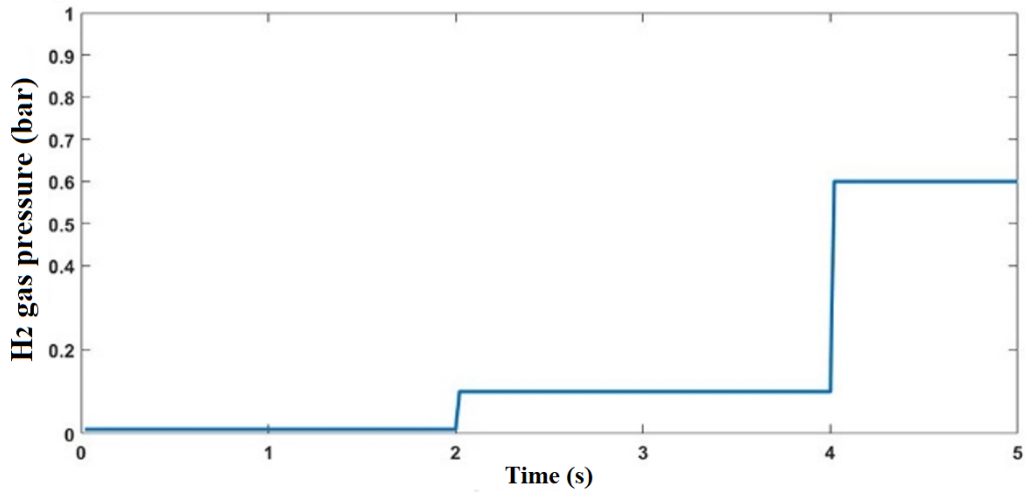

Figure 5.11: Inlet H_2 gas pressure

By taking the ITAE as an objective function, the obtained parameters gain for the proposed controllers used in our study are enlisted in Table. 5.6.

Table 5.6: The obtained PID parameters.

PSO-PID	**ZN PID**
$k_p = 0.52$	$k_p = 0.03$
$k_i = 1.5$	$k_i = 0.67$
$k_d = 0.007$	$K_d = 0.000334$

Figure 5.12 shows the duty cycle for both algorithms. It's clearly seen that both algorithms have the same performance in the tracking of the error besides, show a gradual and smooth rise to the reference value. But there is a superiority for the PSO-PID in the response time. Figure 5.13 shows the current signals for both algorithms. At t=1.5 s, an undershoot of 0.141 A for the PSO-PID, and an undershoot of 1.375 A for the ZN PID. On the other hand, at t=3s an overshoot of 0.255 A for the PSO-PID, and an undershoot of 1 A for the ZN PID. According to Figure 5.14, it is clearly shown that using the PSO-PID, the operation point is achieved quickly with great precision and global stability of the closed-loop system. Besides, it offers high robustness even for large load variation. On the other hand, the ZN PID, at t = 3 s, the power drop to zero, which means that the system loses its efficient power point. Moreover, it is noticeable that the drawback of the ZN- PID controller also appears in a low start-up. According to these results, it is clearly noticed that the PSO-PID bears the sharp load variation. Also, from the results, the PID controller designed using the PSO algorithm exhibits superior performance over the traditional ZN method. However, the traditional method provides us an overview to set the initial PID gain values for tuning optimization. Therefore, the advantage

of using a modern artificial intelligence optimization approach is seen as a complementary solution to improve the performance of the conventionally designed PID controller. However, there are many techniques that can be used as optimization tools, and PSO is one of the recent and effective optimization tools.

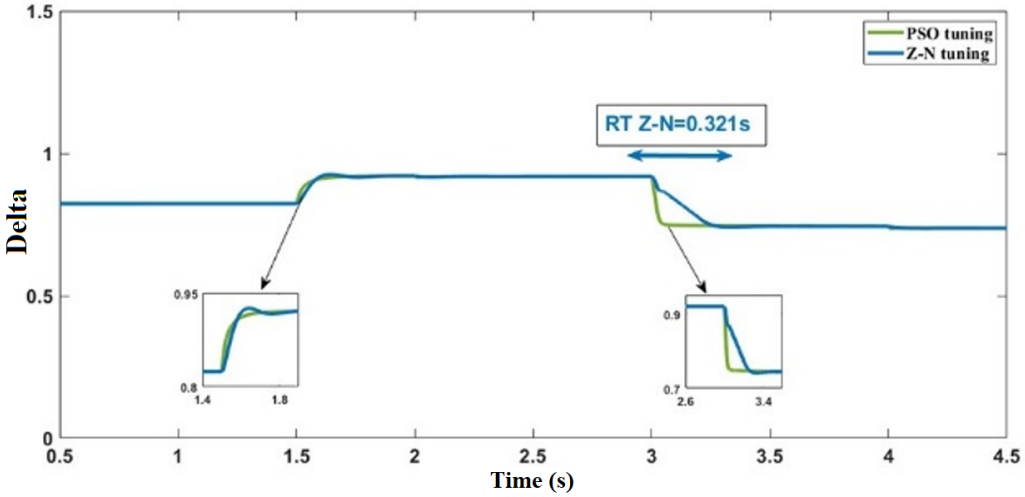

Figure 5.12: Duty cycle signals

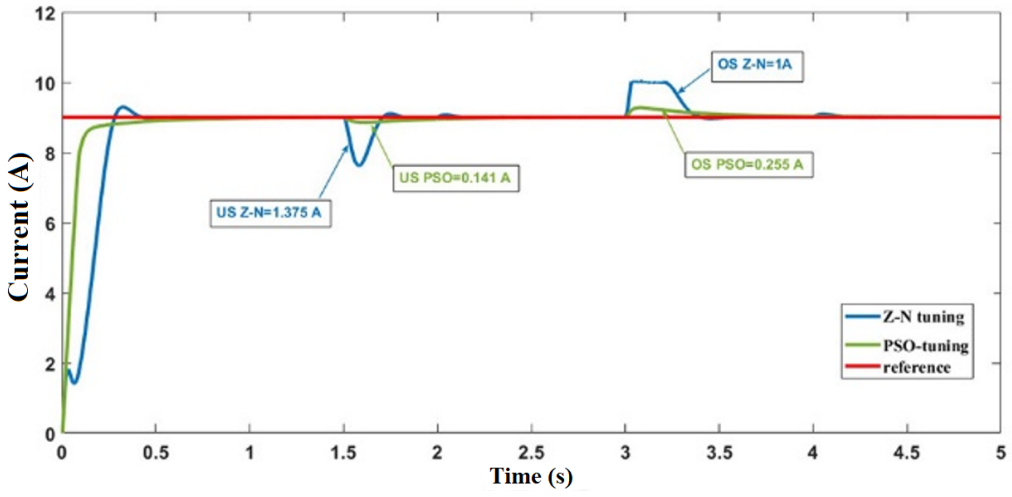

Figure 5.13: PEMFC output current signals

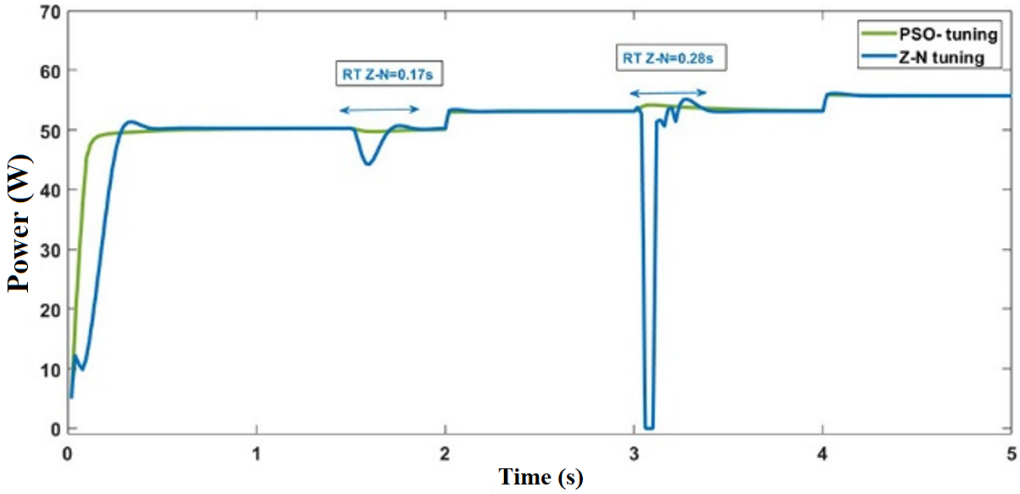

Figure 5.14: PEMFC output power signals

5.7 Conclusion

The objective of this part is to validate and improve the performance of the PEMFC system by using a specific control algorithm. The model of the entire PEMFC system has been established and studied so as to facilitate its analysis. The PEMFC is interfaced by a high step-up DC-DC converter. This study also presents the application of several non-linear controls command approaches for regulating the PEMFC current. The first approach is the conventional SMC. However, although this latter has given satisfactory results in terms of control robustness in real-time, its chattering phenomenon still bears a significant problem since it reduces the accuracy and the overall system efficiency. However, to overcome these drawbacks, a QC-HOSM and integral fast terminal sliding mode combined with digital filter are proposed so as to maintain the robustness of the conventional SMC and to enhance the efficiency of the overall system by decreasing the chattering phenomenon. It has been demonstrated through experimental results that the proposed QC-

HOSM and IFTSMC combined with a digital filter keep effectively the system operating at the adequate power point even under large load resistance variation. Besides, it has been clearly proven the effectiveness of the proposed algorithms over the conventional SMC. Thus a reduction in the chattering effect of 84% and 91% for the QC-HOSM and the IFTSMC combined with a digital filter, respectively are achieved which, accordingly, will increase the accuracy and the overall system efficiency. Finally, a simulations part was done, aiming to apply an optimization methods based on PSO and ZN for the controller of the DC/DC boost converter linked to a PEMFC power system in order to force this latter work at an adequate power point. The simulation results indicate that the suggested approach has considerable advantages compared to the classical controller. Thus, the PSO-PID can yield better performance in terms of rising time, settling time and robustness even for large load variations better than the PID whose parameters are obtained by the ZN method.

GENERAL CONCLUSION

This thesis is devoted to the study and the command of the DC/DC converter type boost linked to a PEMFC controlled by a specific algorithm in order to improve the PEMFC output power quality.

First, we gave a general overview of PEMFC. Then we presented the apparent trajectory of the hydrogen and energy issues and a description of the PEMFCs systems and their performance.

Then we were focusing on the analysis and the comparison of the different typologies of DC-DC converters. After comparison between the different DC/DC converter structures, the boost converters have been selected. The selection criteria are simplicity of structure and gain in tension.

A deep explanation for the different controllers P, PI and PID as well as the classical methods of adjustment of control loops such as the method of ZN and the optimisation method of PSO.

Conventional controller based on the first-order sliding system generally has the major drawback of chattering. In order to attenuate or eliminate it, many solutions have been proposed by replacing the discontinuous term (sign function) with a continuous function (hyperbolic tangent, saturation etc...). However, even by applying this method, one could not eliminate those drawbacks. Recently, researchers have been interested in new methods of HO-SMC. Thereafter, we studied several HO-SMC laws (order two and arbitrary). Where, the control is based on the sliding variable and the rejection of discontinuities from the control to high order derivatives.

The PEMFC configuration based on a simple DC/DC step-up converter,

which is considered for the verification of the proposed IFTSMC, QC-HOSM control methods and the PSO PID optimisation method. An experimental comparative study is investigated between the IFTSMC and the well-known PI controller so as to reveal the merits of the proposed technique. Results have indicated that despite the sharp variations of the load resistance, both controllers succeeded to converge the error to zero value; where, gradual and smooth movements to the desired value with global system stability are obtained. Results also have indicated that both PI and IFTSMC have almost the same performance in terms of overshoots and undershoots; however, it is clearly proven that the feature of the proposed IFTSMC appears in its capability to converge the system to the reference value with high speed (response time = 0.45 s).

The experimental comparative study also has proven the effectiveness of the digital filter application. Hence, up to more than 91% of the chattering phenomenon of the IFTSMC could be eliminated. Therefore, it is clearly proven that the IFTSMC ,with the application of the digital filter, has succeeded to keep the FC-50W stack operating at the desired power point while providing high tracking performance such as high convergence speed with significant chattering reduction. Finally, the obtained results of this work are quite encouraging, and they give prospects for further advanced research to enhance and improve the performance of the PEMFC.

The experimental comparative study is investigated between the QC-HOSM and the well-known SMC so as to reveal the merits of the proposed technique. The first approach is the conventional SMC. However, although this latter has given satisfactory results in terms of control robustness in a real-time, its chattering phenomenon still bears a significant problem since it reduces the accuracy and the overall system efficiency. However, to overcome these drawbacks, a QC-HOSM is proposed so as to maintain the robustness of the conventional SMC and to enhance the efficiency of the overall system by decreasing the chattering phenomenon. It has been demonstrated through experimental results that the proposed QC-HOSM effectively keeps

the system operating at the adequate power point even under large load resistance variation. In addition, it has been clearly proven the effectiveness of the proposed algorithm over the conventional SMC. Thus, a reduction of 84% in the chattering effect is achieved which, accordingly, will increase the accuracy and the overall system efficiency.
The comparative simulation study is investigated between the PSO and ZN so as to reveal the merits of the proposed technique for the controller of the DC/DC boost converter linked to a PEMFC power system in order to force this latter work at an adequate power point. The simulation results indicate that the suggested PSO-PID approach has considerable advantages compared to the classical controller using the ZN. Thus, the PSO-PID can yield better performance in terms of rising time, settling time and robustness even for large load variations better than the PID whose parameters are obtained by the ZN PID method.
The experimental test bench was built at the laboratory of advanced control in the university of Vitoria-Gasteiz, Spain. It consists of a Heliocentric hy-Expert^{TM} FC-50W and its auxiliaries, DSPACE DS1104, DSPACE DS1202, step-up DC-DC boost converter, programmable DC power, and control algorithm. The latter is implemented in Matlab/Simulink, which finally loaded to the DSPACE card. Therefore, the objective of this study is achieved, and we can say that the proposed control strategy can be considered as an interesting solution in the field of control of PEMFC systems.
The work discussed in this thesis is very encouraging and motivates us more and more to continue in this same area of research.

Future Work

Further research is required. Some of the possible problems and direction of solutions are suggested for future work.

1. Modelling of the PEMFC power system by using artificial neural networks.

2. Applying the cognitive algorithm and neural networks topology in the design of an adaptive nonlinear controller for a DC/DC converter in order to ensure high power conversion with a good performance.

3. Applying the optimisations techniques in a DC/DC boost converter linked to a PEMFC in order to tune the controllers parameters.

4. Real-time implementation of an adaptive sliding mode using gradient descent for the DC/DC boost converter linked to PEMFC.

Appendix

Program 1:

```
R = 8.314; % Ideal gas constant (J/molK)
F = 96487; % Faraday constant
T_c = 25; % Temperature in degrees C
P_H_2 = 0.6; % Hydrogen pressure in bar
P_O_2 =0.6; % Air pressure in bar
A_cell=10; % Area of cell
N_cells=10; % Number of Cells
r_i = 0.19; % Internal Resistance (Ohm-cm^2)
Alpha = 0.5; % Transfer coefficient
Alpha1 = 0.085; % Amplification constant
i_o = 10^-6.912; % Exchange Current Density (A/cm^2)
i_l = 1.4; % Limiting current density (A/cm2)
%Gf_l = -228170; % Gibbs function in liquid form (J/mol)
k = 1.1; % Constant k used in mass transport
%%%%%%%%%%%%%%%%%%%%%%%%%%%%%%%%%
% Convert degrees C to K
T_k = T_c + 273.15;
% Create loop for current
loop = 1;
i = 0;
for N = 0:150
i = i + 0.01;
% Calculation of Partial Pressures
% Calculation of saturation pressure of water
x=-2.1794+0.02953.*T_c-9.1837.*(10.^-5).
*(T_c.^2)+1.4454.*(10.^-7).*(T_c.^3);
P_H2O=(10.^x);
% Calculation of partial pressure of hydrogen
pp_H2 = 0.5.*((P_H_2)./(exp(1.653.*i./(Tk.^1.334)))-P_H2O);
% Calculation of partial pressure of oxygen
pp_O2 = (P_O_2./exp(4.192.*i/(T_k.^1.334)))-P_H2O;
% Activation Losses
b = R.*Tk./(2.*Alpha.*F);
V_act = -b.*log10(i./io); % Tafel equation
% Ohmic Losses
V_ohmic = -(i.*r);
% Mass Transport Losses
term = (1-(i./il));
if term > 0
V_conc = Alpha1.*(i.^k).*log(1-(i./il));
else
V_conc = 0;
```

```
end
% Calculation of Nernst voltage
E_nernst=1.229-((R.*T_k).*log(P_H2O.
/(pp_H2.*(pp_O2.^0.5)))./(2.*F);
% Calculation of output voltage
V_out = E_nernst + V_ohmic + V_act + V_conc;
fig1=E_nernst+ V_act;
fig2=E_nernst+ V_act+ V_ohmic;
if term < 0
V_conc = 0;
break
end
if V_out < 0
V_out = 0;
break
end
figure(1)
title('PEMFC polarization curve')
xlabel('Current Density (A/cm^2)');
ylabel('Voltage (V)');
plot(i,V_out,'.')
grid on
hold on
%plot(i,E_nernst,'.')
disp(V_out)
hold on
%plot(i,fig1,'.')
hold on
%plot(i,fig2,'.')
% Calculation of single cell power
P_sigle_cell=i*V_out;
figure(2)
title('PEMFC output power')
xlabel('Current Density (A/cm^2)');
ylabel('Power(W)');
grid on
hold on
%plot(i,V_out,'.')
hold on
plot(i,P_sigle_cell,'.')
% Calculation of power stack
P_out = N_cells.*V_out.*i.*A_cell;
figure(3)
title('PEMFC stack output power')
xlabel('Current Density (A/cm^2)');
ylabel('Power stack(W)');
grid on
```

```
hold on
plot(i,P_out,'.')
disp(P_out);
end
```

Program 2:

```
% Inputs
R = 8.314; % Ideal gas constant (J/mol.K)
F = 96487; % Faraday's constant
Alpha = 0.5; % Transfer coefficient
io = 10^-6.912; % Exchange current density
%%%%%%%%%%%%%%%%%%%%%%%%%%%%%%%%%%%
% Part a: Constant Current Density of 0.7 A with a temperature
range from
i = 0.7; % Current
T = 273:373; % Temperature
% Activation Losses
B = R.*T./(2.*Alpha.*F);
V_act = b.*log10(i./io);
figure1 = figure('Color',[1 1 1]);
hdlp = plot(T,V_act);
title('Losses Activation as a function of temperature','FontSize',12,'FontWeight','Bold')
xlabel('Temperature (K)','FontSize',12,'FontWeight','Bold');
ylabel('Losses Activation (Volts)','FontSize',12,'FontWeight','Bold');
set(hdlp,'LineWidth',1.5);
grid on;
% Part b: Constant temperature of 300 K with a current density
range from
% 0-1 A
i2 = 1:1:50; % range of current
T_2 = 313; % Temperature
% Activation Losses
b2 = R.*T_2./(2.*Alpha.*F);
V_act2 = b2.*log10(i2./io); % Tafel equation
figure2 = figure('Color',[1 1 1]);
hdlp = plot(i2,V_act2);
title('Losses Activation according to Current Density','FontSize',12,'FontWeight','Bold')
xlabel('Current density (A/cm^2)','FontSize',12,'FontWeight','Bold');
ylabel('Losses Activation (Volts)','FontSize',12,'FontWeight','Bold');
set(hdlp,'LineWidth',1.5);
grid on;
```

Program 3:

```
clc;
clear;
close all;
%MAIN PROGRAM
```

```
ObjectiveFunction=@optimize_PID(K); % Objective Function
nVar=3; % Number of Decision Variables
VarSize=[3 nVar]; % Size of Decision Variables Matrix
VarMin=[0.01 0.1 0]; % Lower Bound of Variables
VarMax=[10 10 10]; % Upper Bound of Variables


%% PSO Parameters

MaxIt=100; % Maximum Number of Iterations
nPop=50; % Population Size (Swarm Size)

% PSO Parameters
wmax=0.8; %  Max inertia weight
wmin=0.4; %  Min inertia weight
c1=c2=1.494; %  Coefficient

% Velocity Limits
VelMax=0.1*(VarMax-VarMin);
VelMin=-VelMax;

%% Initialization

empty_particle.Position=[];
empty_particle.Cost=[];
empty_particle.Velocity=[];
empty_particle.Best.Position=[];
empty_particle.Best.Cost=[];

particle=repmat(empty_particle,nPop,1);
GlobalBest.Cost=inf;

for i=1:nPop

% Initialize Position
particle(i).Position=unifrnd(VarMin,VarMax,VarSize);

% Initialize Velocity
particle(i).Velocity=zeros(VarSize);

% Evaluation
particle(i).Cost=CostFunction(particle(i).Position);

% Update Personal Best
particle(i).Best.Position=particle(i).Position;
particle(i).Best.Cost=particle(i).Cost;
```

```
% Update Global Best
if particle(i).Best.Cost<GlobalBest.Cost
GlobalBest=particle(i).Best;

end
end

BestCost=zeros(MaxIt,1);

%% PSO Main Loop

for it=1:MaxIt
for i=1:nPop

% Update Velocity
particle(i).Velocity = w*particle(i).Velocity ...
+c1*rand(VarSize).*(particle(i).Best.Position-particle(i).Position) ...
 +c2*rand(VarSize).*(GlobalBest.Position-particle(i).Position);

% Apply Velocity Limits
particle(i).Velocity = max(particle(i).Velocity,VelMin);
particle(i).Velocity = min(particle(i).Velocity,VelMax);

% Update Position
particle(i).Position = particle(i).Position + particle(i).Velocity;

% Velocity Mirror Effect
IsOutside=(particle(i).Position<VarMin | particle(i).Position>VarMax);
particle(i).Velocity(IsOutside)=-particle(i).Velocity(IsOutside);

% Apply Position Limits
particle(i).Position = max(particle(i).Position,VarMin);
particle(i).Position = min(particle(i).Position,VarMax);

% Evaluation
particle(i).Cost = CostFunction(particle(i).Position);

% Update Personal Best
if particle(i).Cost<particle(i).Best.Cost

particle(i).Best.Position=particle(i).Position;
particle(i).Best.Cost=particle(i).Cost;

% Update Global Best
if particle(i).Best.Cost<GlobalBest.Cost

GlobalBest=particle(i).Best;
```

```
end
end
end

BestCost(it)=GlobalBest.Cost;

disp(['Iteration ' num2str(it) ': Best Cost = ' num2str(BestCost(it))]);

w=wmax*((wmax-wmin)/MaxIt)*it;

end

BestSol = GlobalBest;

%%%%%%%%%%%%%%%%%%%%%%%%%%%%%%%%%%
function cost=optimize_PID(K)
assignin('base','K',K);
sim('slido.slx'); %Simulink
cost=EE(length(EE));
end
```

Bibliography

[Abbaker AM et al., 2020] Abbaker AM, O., Wang, H., and Tian, Y. (2020). Adaptive integral type-terminal sliding mode control for pemfc air supply system using time delay estimation algorithm. *Asian Journal of Control*.

[Akpakpavi, 2017] Akpakpavi, M. (2017). Modeling and control of a car suspension system using p, pi, pid, ga-pid and auto-tuned pid controller in matlab/simulink. *Journal of Multidiciplimry Engineering Science Studies (JMESS) ISSN*.

[Ali et al., 2020] Ali, N., Liu, Z., Hou, Y., Armghan, H., Wei, X., and Armghan, A. (2020). Lcc-s based discrete fast terminal sliding mode controller for efficient charging through wireless power transfer. *Energies*, 13(6), pp 1370.

[Armghan et al., 2020] Armghan, H., Yang, M., Armghan, A., Ali, N., Wang, M., and Ahmad, I. (2020). Design of integral terminal sliding mode controller for the hybrid ac/dc microgrids involving renewables and energy storage systems. *International Journal of Electrical Power & Energy Systems*, 119, pp 105857.

[Asad et al., 2017] Asad, M., Ashraf, M., Iqbal, S., and Bhatti, A. I. (2017). Chattering and stability analysis of the sliding mode control using inverse hyperbolic function. *International Journal of Control, Automation and Systems*, 15(6), pp 2608–2618.

[Astrom, 1988] Astrom, K. J. (1988). Automatic tuning of pid controllers. *Insturment Society of America*.

[Azar and Serrano, 2020] Azar, A. T. and Serrano, F. E. (2020). Stabilization of port hamiltonian chaotic systems with hidden attractors by adaptive terminal sliding mode control. *Entropy*, 22(1), pp 122.

[Bai, 2010] Bai, Q. (2010). Analysis of particle swarm optimization algorithm. *Computer and information science*, 3(1), pp 180.

[Bartolini et al., 2000] Bartolini, G., Ferrara, A., Usai, E., and Utkin, V. I. (2000). On multi-input chattering-free second-order sliding mode control. *IEEE transactions on automatic control*, 45(9), pp 1711–1717.

[Baschuk and Li, 2005] Baschuk, J. and Li, X. (2005). A general formulation for a mathematical pem fuel cell model. *Journal of power sources*, 142(1-2), pp 134–153.

[Behling, 2012] Behling, N. H. (2012). *Fuel cells: current technology challenges and future research needs*. Newnes.

[Bühler, 1986] Bühler, H. (1986). *Réglage par mode de glissement*. PPUR presses polytechniques.

[Candusso, 2013] Candusso, D. (2013). *Contribution à l'expérimentation de générateurs à piles à combustible de type PEM pour les systèmes de transport*. PhD thesis, École normale supérieure de Cachan-ENS Cachan.

[Cao et al., 2018] Cao, Q., Cao, C., Wang, F., Liu, D., and Sun, H. (2018). Robust adaptive full-order tsm control based on neural network. *Symmetry*, 10(12), pp 726.

[Ceraolo et al., 2003] Ceraolo, M., Miulli, C., and Pozio, A. (2003). Modelling static and dynamic behaviour of proton exchange membrane fuel cells on the basis of electro-chemical description. *Journal of power sources*, 113(1), pp 131–144.

[Che et al., 2020] Che, X., Tian, D., Jia, P., Gao, Y., and Ren, Y. (2020). Terminal sliding mode control with a novel reaching law and sliding mode disturbance observer for inertial stabilization imaging sensor. *Sensors*, 20(11), pp 3107.

[Choe et al., 2007] Choe, S.-Y., Lee, J.-G., Ahn, J.-W., and Baek, S.-H. (2007). Integrated modeling and control of a pem fuel cell power system with a pwm dc/dc converter. *Journal of Power Sources*, 164(2), pp 614–623.

[Choudhury and Kraft, 2004] Choudhury, D. and Kraft, D. W. (2004). Big bang nucleosynthesis and the missing hydrogen mass in the universe. In *AIP Conference Proceedings*, volume 698, pages 345–348. American Institute of Physics.

[Corrêa et al., 2004] Corrêa, J. M., Farret, F. A., Canha, L. N., and Simoes, M. G. (2004). An electrochemical-based fuel-cell model suitable for electrical engineering automation approach. *IEEE Transactions on industrial electronics*, 51(5), pp 1103–1112.

[Delgado et al., 2020] Delgado, S., Lagarteira, T., and Mendes, A. (2020). Air bleeding strategies to increase the efficiency of proton exchange membrane fuel cell stationary applications fuelled with co ppm-levels. *Int. J. Electrochem. Sci*, 15, pp 613–627.

[Derbeli et al., 2020] Derbeli, M., Barambones, O., Farhat, M., Ramos-Hernanz, J. A., and Sbita, L. (2020). Robust high order sliding mode control for performance improvement of pem fuel cell power systems. *International Journal of Hydrogen Energy*, 45(53), pp 29222–29234.

[Derbeli et al., 2019a] Derbeli, M., Barambones, O., Farhat, M., and Sbita, L. (2019a). Efficiency boosting for proton exchange membrane fuel cell power system using new mppt method. In *2019 10th International Renewable Energy Congress (IREC)*, pages 1–4. IEEE.

[Derbeli et al., 2019b] Derbeli, M., Barambones, O., Ramos-Hernanz, J. A., and Sbita, L. (2019b). Real-time implementation of a super twisting algorithm for pem fuel cell power system. *Energies*, 12(9), pp 1594.

[Derbeli et al., 2017a] Derbeli, M., Farhat, M., Barambones, O., and Sbita, L. (2017a). Control of pem fuel cell power system using sliding mode and super-twisting algorithms. *International journal of hydrogen energy*, 42(13), pp 8833–8844.

[Derbeli et al., 2017b] Derbeli, M., Sbita, L., Farhat, M., and Barambones, O. (2017b). Proton exchange membrane fuel cell—a smart drive algorithm. In *2017 International Conference on Green Energy Conversion Systems (GECS)*, pages 1–5. IEEE.

[Doan et al., 2020] Doan, Q. V., Vo, A. T., Le, T. D., Kang, H.-J., and Nguyen, N. H. A. (2020). A novel fast terminal sliding mode tracking control methodology for robot manipulators. *Applied Sciences*, 10(9), pp 3010.

[Eberhart and Shi, 2000] Eberhart, R. C. and Shi, Y. (2000). Comparing inertia weights and constriction factors in particle swarm optimization. In *Proceedings of the 2000 congress on evolutionary computation. CEC00 (Cat. No. 00TH8512)*, volume 1, pages 84–88. IEEE.

[Escobar et al., 2011] Escobar, G., Pettersson, S., Ho, C., Karppanen, M., and Pulli, T. (2011). Pv current sensorless mppt for a single-phase pv inverter. In *IECON 2011-37th Annual Conference of the IEEE Industrial Electronics Society*, pages 3906–3911. IEEE.

[Fang et al., 2019] Fang, J.-S., Tsai, J. S.-H., Yan, J.-J., and Guo, S.-M. (2019). Adaptive chattering-free sliding mode control of chaotic systems with unknown input nonlinearity via smooth hyperbolic tangent function. *Mathematical Problems in Engineering*, 2019.

[Feng et al., 2002] Feng, Y., Yu, X., and Man, Z. (2002). Non-singular terminal sliding mode control of rigid manipulators. *Automatica*, 38(12), pp 2159–2167.

[Fridman and Levant, 2002] Fridman, L. and Levant, A. (2002). High-order sliding modes sliding modes control in engineering. *Ed. W. Perruquetti, JP Barbot, M. Dekker, Inc. New York*.

[Gao and Hung, 1993] Gao, W. and Hung, J. C. (1993). Variable structure control of nonlinear systems: A new approach. *IEEE transactions on Industrial Electronics*, 40(1), pp 45–55.

[García-Olivares et al., 2020] García-Olivares, A., Solé, J., Samsó, R., and Ballabrera-Poy, J. (2020). Sustainable european transport system in a 100% renewable economy. *Sustainability*, 12(12), pp 5091.

[Gertler, 1998] Gertler, J. (1998). *Fault detection and diagnosis in engineering systems*. CRC press.

[Grooves, 1839] Grooves, W. (1839). On volatic series and the combination of gases by platinum. *philos. Mag*, 14, pp 127–130.

[Grubb and Niedrach, 1960] Grubb, W. and Niedrach, L. (1960). Batteries with solid ion-exchange membrane electrolytes: Ii. low-temperature hydrogen-oxygen fuel cells. *Journal of the Electrochemical Society*, 107(2), pp 131.

[Gudey and Gupta, 2016] Gudey, S. K. and Gupta, R. (2016). Recursive fast terminal sliding mode control in voltage source inverter for a low-voltage microgrid system. *IET Generation, Transmission & Distribution*, 10(7), pp 1536–1543.

[Guesmi et al., 2018] Guesmi, S., Jamoussi, K., Ghariani, M., and Chrifi-Alaoui, L. (2018). Experimental validation of the robustness of super-twisting control for induction motor of electric vehicle.

[Hijazi, 2010] Hijazi, A. (2010). *Modélisation électrothermique, commande et dimensionnement d'un système de stockage d'énergie par supercondensateurs avec prise en compte de son vieillissement: application à la récupération de l'énergie de freinage d'un trolleybus*. PhD thesis.

[Ho et al., 1996] Ho, W. K., Gan, O., Tay, E. B., and Ang, E. (1996). Performance and gain and phase margins of well-known pid tuning formulas. *IEEE Transactions on Control Systems Technology*, 4(4), pp 473–477.

[Hoogers, 2002] Hoogers, G. (2002). *Fuel cell technology handbook*. CRC press.

[Hua et al., 2014] Hua, T., Ahluwalia, R., Eudy, L., Singer, G., Jermer, B., Asselin-Miller, N., Wessel, S., Patterson, T., and Marcinkoski, J. (2014). Status of hydrogen fuel cell electric buses worldwide. *Journal of Power Sources*, 269, pp 975–993.

[Huang, 2009] Huang, B. (2009). *Convertisseur continu-continu à rapport de transformation élevé pour applications pile à combustible*. PhD thesis, Institut National Polytechnique de Lorraine.

[Iqbal, 2003] Iqbal, M. (2003). Modeling and control of a wind fuel cell hybrid energy system. *Renewable energy*, 28(2), pp 223–237.

[Isidori et al., 1995] Isidori, A., van Schuppen, J., Sontag, E., Thoma, M., and Krstic, M. (1995). Communications and control engineering. *Nonlinear control systems*.

[Johnson and Moradi, 2005] Johnson, M. A. and Moradi, M. H. (2005). *PID control*. Springer.

[Kåberger, 2018] Kåberger, T. (2018). Progress of renewable electricity replacing fossil fuels. *Global Energy Interconnection*, 1(1), pp 48–52.

[Kennedy and Eberhart, 1995] Kennedy, J. and Eberhart, R. (1995). Particle swarm optimization. In *Proceedings of ICNN'95-international conference on neural networks*, volume 4, pages 1942–1948. IEEE.

[Kester et al.,] Kester, W., Erisman, B., and Thandi, G. Section 4 switched capacitor voltage converters. *Switched Capacitor Voltage Converters,(21 pages total)*.

[Kim et al., 2008] Kim, T.-H., Maruta, I., and Sugie, T. (2008). Robust pid controller tuning based on the constrained particle swarm optimization. *Automatica*, 44(4), pp 1104–1110.

[Komurcugil, 2012] Komurcugil, H. (2012). Adaptive terminal sliding-mode control strategy for dc–dc buck converters. *ISA transactions*, 51(6), pp 673–681.

[Larminie et al., 2003] Larminie, J., Dicks, A., and McDonald, M. S. (2003). *Fuel cell systems explained*, volume 2. J. Wiley Chichester, UK.

[Lee and Lin, 2020] Lee, D. and Lin, K.-C. (2020). How to transform sustainable energy technology into a unicorn start-up: Technology review and case study. *Sustainability*, 12(7), pp 3018.

[Lee et al., 1998] Lee, J., Lalk, T., and Appleby, A. (1998). Modeling electrochemical performance in large scale proton exchange membrane fuel cell stacks. *Journal of power sources*, 70(2), pp 258–268.

[Levant, 1993] Levant, A. (1993). Sliding order and sliding accuracy in sliding mode control. *International journal of control*, 58(6), pp 1247–1263.

[Levant, 2001] Levant, A. (2001). Universal single-input-single-output (siso) sliding-mode controllers with finite-time convergence. *IEEE transactions on Automatic Control*, 46(9), pp 1447–1451.

[Levant, 2003] Levant, A. (2003). Quasi-continuous high-order sliding-mode controllers. In *42nd IEEE International Conference on Decision and Control (IEEE Cat. No. 03CH37475)*, volume 5, pages 4605–4610. IEEE.

[Levant, 2005] Levant, A. (2005). Homogeneity approach to high-order sliding mode design. *Automatica*, 41(5), pp 823–830.

[Liutanakul, 2007] Liutanakul, P. (2007). *Stabilité des réseaux embarqués: interactions Puissance-Structure-Commande*. PhD thesis, Institut National Polytechnique de Lorraine.

[Luta and Raji, 2019] Luta, D. N. and Raji, A. K. (2019). Fuzzy rule-based and particle swarm optimisation mppt techniques for a fuel cell stack. *Energies*, 12(5), pp 936.

[Magoon, 2018] Magoon, Jr; Clare, R. (2018). *Creation and the Big Bang: How God Created Matter from Nothing*. WestBow Press.

[Mamizadeh et al., 2018] Mamizadeh, A., Genc, N., and Rajabioun, R. (2018). Optimal tuning of pi controller for boost dc-dc converters based on cuckoo optimization algorithm. In *2018 7th international conference on renewable energy research and applications (ICRERA)*, pages 677–680. IEEE.

[Mardle et al., 2020] Mardle, P., Ji, X., Wu, J., Guan, S., Dong, H., and Du, S. (2020). Thin film electrodes from pt nanorods supported on aligned n-cnts for proton exchange membrane fuel cells. *Applied Catalysis B: Environmental*, 260, pp 118031.

[Méndez-Barrios et al., 2008] Méndez-Barrios, C., Niculescu, S.-I., Morarescu, C.-I., and Gu, K. (2008). On the fragility of pi controllers for time-delay siso systems. In *2008 16th mediterranean conference on control and automation*, pages 529–534. IEEE.

[Mosdale, 2003] Mosdale, R. (2003). Transport électrique routier: Véhicules électriques à pile à combustible. *Techniques de l'ingénieur. Génie électrique*, 12(D5570), pp D5570–1.

[Nekoui et al., 2010] Nekoui, M. A., Khameneh, M. A., and Kazemi, M. H. (2010). Optimal design of pid controller for a cstr system using particle swarm optimization. In *Proceedings of 14th International Power Electronics and Motion Control Conference EPE-PEMC 2010*, pages T7–63. IEEE.

[Nouaouria et al., 2014] Nouaouria, N., Boukadoum, M., and Proulx, R. (2014). Position update mechanisms for enhanced particle swarm classification. In *2014 IEEE 13th International Conference on Cognitive Informatics and Cognitive Computing*, pages 48–52. IEEE.

[O'dwyer, 2009] O'dwyer, A. (2009). *Handbook of PI and PID controller tuning rules*. World Scientific.

[O'hayre et al., 2016] O'hayre, R., Cha, S.-W., Colella, W., and Prinz, F. B. (2016). *Fuel cell fundamentals*. John Wiley & Sons.

[Qi et al., 2009] Qi, R., Hu, B., and Cournede, P.-H. (2009). Psots: a particle swarm optimization toolbox in scilab. In *2009 IEEE international workshop on open-source software for scientific computation (OSSC)*, pages 107–114. IEEE.

[Qi et al., 2020] Qi, Z., Tang, J., Pei, J., and Shan, L. (2020). Fractional controller design of a dc-dc converter for pemfc. *IEEE Access*, 8, pp 120134–120144.

[Rastayesh et al., 2020] Rastayesh, S., Bahrebar, S., Blaabjerg, F., Zhou, D., Wang, H., and Dalsgaard Sørensen, J. (2020). A system engineering approach using fmea and bayesian network for risk analysis—a case study. *Sustainability*, 12(1), pp 77.

[Reddy and Samuel, 2020] Reddy, B. M. and Samuel, P. (2020). Modeling and simulation of proton exchange membrane fuel cell hybrid electric vehicle. In *Intelligent Computing Techniques for Smart Energy Systems*, pages 281–291. Springer.

[Reddy and Sudhakar, 2018] Reddy, K. J. and Sudhakar, N. (2018). A new rbfn based mppt controller for grid-connected pemfc system with high step-up three-phase ibc. *International Journal of Hydrogen Energy*, 43(37), pp 17835–17848.

[Reddy and Sudhakar, 2019] Reddy, K. J. and Sudhakar, N. (2019). Anfis-mppt control algorithm for a pemfc system used in electric vehicle applications. *International Journal of Hydrogen Energy*, 44(29), pp 15355–15369.

[Rizi and Eliasi, 2020] Rizi, M. T. and Eliasi, H. (2020). Nonsingular terminal sliding mode controller for voltage and current control of an islanded microgrid. *Electric Power Systems Research*, 185, pp 106354.

[Saltzman, 1984] Saltzman, B. A. S. A. R. H. (1984). *Earth-orbital eccentricity variations and climatic change*. Springer.

[Shotorbani et al., 2017] Shotorbani, A. M., Ghassem-Zadeh, S., Mohammadi-Ivatloo, B., and Hosseini, S. H. (2017). A distributed secondary scheme with terminal sliding mode controller for energy storages in an islanded microgrid. *International Journal of Electrical Power & Energy Systems*, 93, pp 352–364.

[Silva et al., 2007] Silva, G. J., Datta, A., and Bhattacharyya, S. P. (2007). *PID controllers for time-delay systems*. Springer Science & Business Media.

[Slotine, 1984] Slotine, J.-J. E. (1984). Sliding controller design for non-linear systems. *International Journal of control*, 40(2), pp 421–434.

[Slotine et al., 1991] Slotine, J.-J. E., Li, W., et al. (1991). *Applied nonlinear control*, volume 199. Prentice hall Englewood Cliffs, NJ.

[Solihin et al., 2011] Solihin, M. I., Tack, L. F., and Kean, M. L. (2011). Tuning of pid controller using particle swarm optimization (pso). In *Proceeding of the International Conference on Advanced Science, Engineering and Information Technology*, volume 1, pages 458–461.

[Srinivasan, 2006] Srinivasan, S. (2006). *Fuel cells: from fundamentals to applications*. Springer Science & Business media.

[Stevens et al., 2000] Stevens, P., Novel-Cattin, F., Hammou, A., Lamy, C., and Cassir, M. (2000). Piles à combustible. *Techniques de l'ingénieur. Génie électrique*, 5(D3340), pp D3340–1.

[Trigeassou et al., 2003] Trigeassou, J., Poinot, T., and Bachir, S. (2003). Méthodes de commande des machines électriques, chapter 7: Estimation paramétrique pour la connaissance et le diagnostic des machines électriques. *Traité EGEN-Série Génie Elctrique, sous la direction de R. Husson, Hermes, Paris*, pages 215–249.

[Utkin, 1977] Utkin, V. (1977). Variable structure systems with sliding modes. *IEEE Transactions on Automatic control*, 22(2), pp 212–222.

[Utkin et al., 1999] Utkin, V., Guldner, J., and Shijun, M. (1999). *Sliding mode control in electro-mechanical systems*, volume 34. CRC press.

[Utkin, 2013] Utkin, V. I. (2013). *Sliding modes in control and optimization*. Springer Science & Business Media.

[Vangari et al., 2015] Vangari, A., Haribabu, D., and Sakamuri, J. N. (2015). Modeling and control of dc/dc boost converter using k-factor control for mppt of solar pv system. In *2015 International Conference on Energy Economics and Environment (ICEEE)*, pages 1–6. IEEE.

[Venkataraman and Gulati, 1993] Venkataraman, S. and Gulati, S. (1993). Control of nonlinear systems using terminal sliding modes.

[Wang et al., 2013] Wang, G., Wang, F., Magai, G., Lei, Y., Huang, A., and Das, M. (2013). Performance comparison of 1200v 100a sic mosfet and 1200v 100a silicon igbt. In *2013 IEEE Energy Conversion Congress and Exposition*, pages 3230–3234. IEEE.

[Wang et al., 2020] Wang, Y., Yang, Y., Kuang, H., Yuan, D., Yu, C., Chen, J., Hua, N., and Hou, H. (2020). High performance both in low-speed tracking and large-angle swing scanning based on adaptive nonsingular fast terminal sliding mode control for a three-axis universal inertially stabilized platform. *Sensors*, 20(20), pp 5785.

[Wang et al., 2019] Wang, Y., Yu, H., Che, Z., Wang, Y., and Liu, Y. (2019). The direct speed control of pmsm based on terminal sliding mode and finite time observer. *Processes*, 7(9), pp 624.

[Williams, 1994] Williams, K. (1994). Francis thomas bacon, 21 december 1904-24 may 1992.

[Yu and Zhihong, 2002] Yu, X. and Zhihong, M. (2002). Fast terminal sliding-mode control design for nonlinear dynamical systems. *IEEE Transactions on Circuits and Systems I: Fundamental Theory and Applications*, 49(2), pp 261–264.

[Zafran et al., 2020] Zafran, M., Khan, L., Khan, Q., Ullah, S., Sami, I., and Ro, J.-S. (2020). Finite-time fast dynamic terminal sliding mode maximum power point tracking control paradigm for permanent magnet synchronous generator-based wind energy conversion system. *Applied Sciences*, 10(18), pp 6361.

[Zhang, 2010] Zhang, Z. (2010). *Modélisation mécanique des interfaces multi-contacts dans une pile à combustible.* PhD thesis, Evry-Val d'Essonne.

[Zhao et al., 2020] Zhao, H., Zhang, L., Liu, J., Zhang, C., Cai, J., and Shen, L. (2020). Design of a low-order fir filter for a high-frequency square-wave voltage injection method of the pmlsm used in maglev train. *Electronics*, 9(5), pp 729.